Towards High Fidelity Quantum Computation and Simulation with Rydberg Atoms

Thesis by
Anant Kale

In Partial Fulfillment of the Requirements for the
Degree of
Bachelor of Science in Physics

CALIFORNIA INSTITUTE OF TECHNOLOGY
Pasadena, California

2020
Defended June 5, 2020

Anant Kale
ORCID: 0000-0002-7049-5630

ACKNOWLEDGEMENTS

First and foremost, I would like to thank Professor Manuel Endres, my thesis advisor, for giving me the opportunity to work in his group, starting as a SURF last year which then naturally led to this thesis project. Being a part of Endres group has helped me develop a passion for AMO physics and has shaped my future research path. I would like to thank Prof. Endres for his guidance on this project, his support and advice regarding graduate school admissions, and for the various other factors which have helped me become a better researcher.

I would also like to thank everyone else in the Endres group for their help over the last year. A very special thanks to Joonhee for being extremely supportive and encouraging, and for always being available to answer my questions. Thanks to Jake for his guidance throughout the project and especially during my SURF project, for teaching me the basics of AMO experiments, and for his advice on graduate schools and future career paths. Thanks to Ivaylo for his help and guidance in building the ladder array setup, for helping me grow as an experimentalist and for answering my questions in general. Thanks to Adam for his help in solving the numerous technical difficulties I faced during this project. Thanks to Hannes and Tai Hyun for their mentorship and many helpful discussions. And thanks to Vlad and Alex for their guidance and support.

Lastly, I would like to thank my parents for all their support and encouragement.

ABSTRACT

Individually trapped neutral atoms are a promising candidate for use in quantum computing and simulation applications. They are highly scalable, have long coherence times and can be entangled via strong dipole-dipole interactions by driving to highly excited Rydberg states. However, the fidelity of single atom operations as well as two-atom entangling operations is limited by intrinsic sources of decoherence such as atomic motion, as well as technical sources of noise such as laser intensity fluctuations and phase/frequency fluctuations. We study the effect of these factors on single atom Rabi oscillations and two-atom Rydberg blockaded Rabi oscillations, using perturbation theory and numerical simulation. We develop a window function approach which helps us qualitatively understand the significance of the different spectral components of the noise as well as quantitatively understand the dependence of the Rabi oscillation fidelity on Rabi frequency. This allows us to predict the maximum experimentally achievable fidelities using independent measurements of experimental parameters such as noise spectra and atomic temperature. Turning to the question of near-term scalability of the experimental system, we prototype and test a method of generating a 'ladder' configuration of optical tweezers utilizing two independent lasers. Our setup allows us to fully tune the geometry of the ladder, namely the separation between the two rows, the angle between them, and their relative position along the axis of the ladder. This pseudo-2D configuration enables us to reach larger system sizes in the near future and allows us to access beyond 1D physics.

TABLE OF CONTENTS

Chapter 1

INTRODUCTION

Over the past few decades, one of the major goals of the physics community has been the development of feasible quantum computers and quantum simulators. From the time since the idea of using a quantum mechanical device to simulate nature was first proposed [1], there has been remarkable experimental [2] and theoretical [3] progress towards making this idea a reality. Large scale quantum computers/simulators have significant applications in a large variety of fields. For example, they would allows us to gain a deeper understanding of many-body quantum phenomena in condensed matter [4], and the fundamental behavior of particles in high-energy physics [5]. They would enable us to make accurate models of large molecules, improving our understanding of quantum chemistry as well as potentially enabling more efficient chemical synthesis [6]. They have already been shown to provide speed-ups over classical computers in several important problems, and it is believed that they would provide speed-ups in many more highly practical computational problems [3].

Various experimental platforms have been developed over the years to try to build quantum computers and simulators. These devices usually work with collections of (effectively) two-level systems known a qubits or quantum bits, analogous to classical binary bits of information on classical computers. The various experimental platforms can be categorized based on which quantum mechanical system they use to define their qubits. A few prominent platforms include superconducting circuits [7], trapped ions [8], quantum dots[9] and neutral atoms [10]. Regardless of how a qubit is defined, universal quantum computation and digital quantum simulation can be performed using single- and two-qubit quantum gates [11], analogous to classical logical gates. Thus it is convenient of think of quantum devices as devices that implement quantum circuits comprised of quantum gates. To solve meaningful problems we would like to perform quantum operations with many qubits and with large circuit depths. To reach large system sizes, we would like our quantum devices to be scalable. And to reach large circuit depths, we would like our quantum gates to be precise and reliable, or 'high fidelity'. Thus scalability and gate fidelity are the primary means of comparing various experimental platforms.

Neutral atom arrays have recently emerged as a promising platform for quantum computation [12, 13, 14, 15, 16, 17, 18] and simulation [19, 20, 21, 22, 23]. They are highly scalable, have long coherence times and competitive gate fidelities. In particular, neutral atoms can be arranged in a large one-, two- or three-dimensional arrays, and be addressed individually by laser beams for qubit operations with little crosstalk to quantum states of nearby atoms [24, 25]. Gate protocols utilizing highly excited (Rydberg) states [26] currently provide the best means for entangling two neutral atom qubits. Yet, the gate fidelities achieved with neutral atoms are comparatively lower than those with platforms such as trapped ions [27] or superconducting qubits [28]. Various decoherence channels have limited the practically achievable fidelities in neutral atom systems. However, this is a relatively more recent field and we are still primarily limited by technical imperfections, rather than any fundamental limitations of this platform [29, 30, 31]. Thus understanding and mitigating the sources of decoherence in this system is very important.

1.1 Outline and summary of results

In the Endres group, we conduct experiments with individually trapped arrays of neutral Strontium-88 (^{88}Sr) atoms. In the latter portion of this chapter, we provide an overview of this experimental setup. In neutral atom qubits, single qubit rotations can be performed using single atom Rabi oscillations. Two-qubit entanglement can be generated by driving Rabi oscillations in the Rydberg blockade regime, in which strong interactions between Rydberg states prevents the excitation of two nearby atoms to the Rydberg state. Thus we focus our attention on single atom and blockaded Rabi oscillations.

In chapter 2, we review how atoms interact with a classical electromagnetic field to undergo Rabi oscillations. We derive the rotating wave Hamiltonian in the absence of noise as well as in the presence of classical noise. We provide a general solution to the two-level dynamics resulting from light-matter interaction. We also review how two atoms in the Rydberg state interact via the van der Waal potential to produce entanglement.

The sources of decoherence in neutral atom experiments include laser noise, atomic motion at finite temperature, spontaneous emission, black body radiation, off-resonant scattering of light, imperfect pulse control, and state detection and preparation errors. Of these, the dominant ones are laser intensity

noise, laser frequency noise, atomic motion and spontaneous emission. In chapter 3, we describe how we measured the laser intensity and frequency noise power spectral density (PSD) for our Rydberg laser.

Previous works [32, 14, 26] have numerically studied the effect of various noise sources on single atom Rabi oscillations. In chapter 4, we extend upon the previous works by providing a simple analytical understanding of the effect of the dominant noise sources using perturbation theory. We analytically study the effect laser intensity noise, laser frequency noise and atomic motion on single atom and two-atom blockaded Rabi oscillations. Further we provide analytic upper bounds on experimentally achievable single atom and blockaded π-pulse fidelities. For the case of laser intensity and frequency noise, we derive analytic 'window' functions which select only specific components of the intensity and frequency noise spectra. These window functions help us qualitatively understand the significance of various spectral components of the noise as well as quantitatively understand the dependence of the Rabi oscillation fidelity on Rabi frequency. We find that for the case of only laser intensity noise, the π-pulse fidelity decreases with increasing Rabi frequency, whereas for the case of only laser frequency noise, the π-pulse fidelity increases with increasing Rabi frequency. The decoherence caused by atomic motion at finite temperature also decreases with increasing Rabi frequency. We see similar behavior for the blockaded π-pulse fidelity. We compare our perturbation theory results to numerical simulation and find good agreement. Further, we compare our result to our recent experimental work [17] in which we report the highest neutral atom entanglement fidelity and find good agreement as well.

In chapter 5, we study single atom and blockaded Rabi oscillations of trapped atoms. Most Rydberg atom experiments are conducted with the optical traps momentarily turned off during laser interrogation. This is because generically Rydberg states are repelled from red-detuned optical traps. However, blinking the traps off during interrogation leads to heating and loss of atoms, presenting challenges for sequential gates for large circuit depths. Thus we investigate the fidelity of Rabi oscillations when the optical traps are left on. Instead of working in the usual fock basis of the harmonic trapping potential, we define a more convenient modified basis of a displaced harmonic oscillator. Working in this basis allows us to treat the 'non-magic' trapping condition perturbatively. We find that we can still achieve high fidelities for single atom and blockaded

π-pulses when the Rabi frequency is much larger than the trap frequency spacing. We also experimentally demonstrated this in [17].

In chapter 6, we turn to the question of near term scalability of Strontium atom arrays. To achieve magic trapping condition, we require a trapping laser wavelength of 813nm. However, the optical polarizability of Strontium at this wavelength is comparatively small and the commercially available laser power is also limited. We explore one method to scale up the system size by using two separate lasers to double the optical power. We generate two rows of optical tweezers, one from each laser, and combine them into a ladder configuration where the two rows are parallel to each other. We prototype a setup which allows us to fully tune the geometry of the ladder, we can adjust the separation between the two rows and the position along the axis of the ladder. This pseudo-2D configuration allows us to access beyond 1D physics models in addition to reaching larger system sizes. Finally we test the mechanical stability of the setup to check if the alignment or position of the tweezers drifts with time. We find that the mechanical stability is satisfactory.

In chapter 7 we provide concluding remarks and outlook for future work.

1.2 Overview of Sr experiment

In the Endres lab, we conduct experiments with individually trapped atoms of neutral Strontium-88 (^{88}Sr). Compared to the more conventional alkali atoms such as Rubidium or Cesium, alkaline-earth (-like) atoms (AEAs) such as Strontium and Ytterbium have a more complex electronic structure which provides several benefits as detailed below. AEAs have narrow optical transitions which allow us to reach lower atomic temperatures through narrow-line cooling. They also have ultra-narrow optical transitions, also known as 'clock' transitions, which allow us to build extremely precise and accurate optical atomic clocks. AEAs allow for single photon excitation to Rydberg states from metastable clock states, leading to high fidelity Rydberg control. Further the two valence electron structure of AEAs allows for high fidelity loss-based detection of Rydberg states using auto-ionization.

The full experiment is described in detail in [34, 33, 35, 17]. We summarize the main steps below (see Figure 1.1). Strontium-88 atoms start off in an atomic beam oven at a high temperature. These are first slowed using a Zeeman slower and 2D magneto-optical trap (MOT). Then the atoms are cooled and trapped

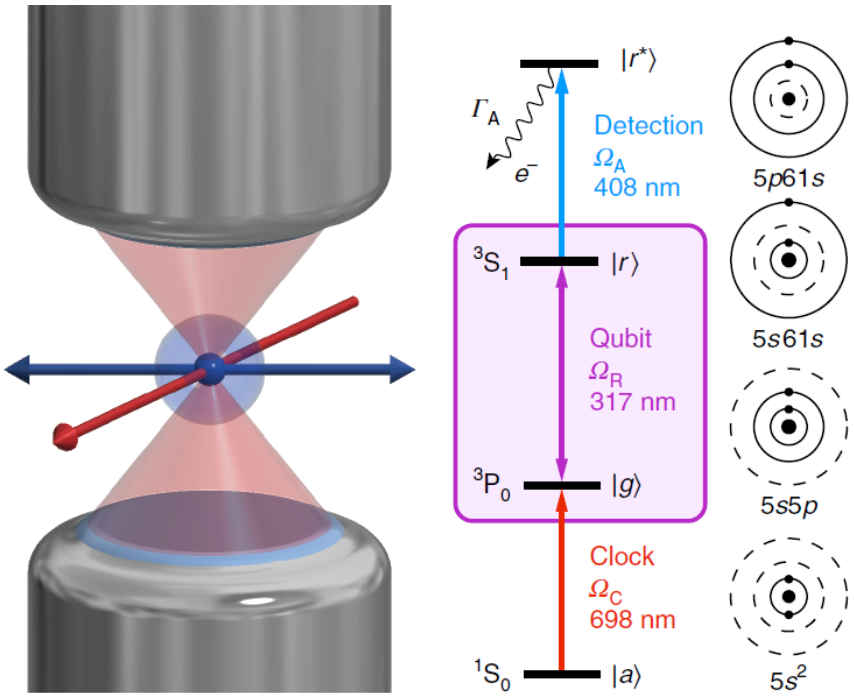

(a) Optical Tweezer

(b) Simplified level structure and electronic configuration for ^{8}8Sr.

Figure 1.1: Overview of the experiment. (a) Tweezer trapping of Strontium atoms. Individual ^{88}Sr atoms are trapped in 813nm magic wavelength optical tweezers generated through microscope objectives (grey) with NA = 0.5. The atoms are cooled with 689nm light (red) and imaged with 461nm light (dark blue). Figure from [33]. (b) Relevant level structure (left) and electronic configuration (right) for Rydberg control with ^{88}Sr. The Rydberg ground-state qubit is defined by a metastable 'clock' state $|g\rangle$ and the 5s61s $^3S_1$ $m_J = 0$ Rydberg state $|r\rangle$ (highlighted with a purple box), which we detect by driving to an auto-ionizing 5p61s state $|r^*\rangle$. Subscripts: A, auto-ionizing; R, Rydberg; C, clock. The clock state $|g\rangle$ is initialized from the absolute ground state $|a\rangle$. Figure from [17]

in a 3D 'blue' MOT operating on the broad $^1S_0 \leftrightarrow {}^1P_1$ dipole allowed blue transition (460.9 nm), followed by a 3D 'red' MOT operating on the narrow $^1S_0 \leftrightarrow {}^3P_1$ red transition (689.5 nm). The atoms in the absolute ground state $^1S_0$ ($|a\rangle$) are then loaded into a 1D array of optical tweezers which are generated using an acousto-optic deflector (AOD) and microscope objectives with NA = 0.5. The wavelength of the tweezer trapping light is chosen to be 813.4 nm which is the magic wavelength for the doubly-forbidden ultra-narrow $^1S_0 \leftrightarrow {}^3P_0$ optical clock transition ($\approx$ 698nm). The number of atoms loaded in each tweezer is restricted to be only zero or one via light-assisted

collisions, resulting in $\sim 50\%$ stochastic loading of each tweezer. The atoms in $|a\rangle$ are imaged via fluorescence imaging on the blue 461nm transition. The tweezers which are loaded with one atom are then rearranged to the desired configuration (non-interacting or strongly interacting) using the AOD.

The meta-stable clock state $|g\rangle$ is prepared from $|a\rangle$ by first driving a coherent π-pulse on the clock transition followed by incoherent optical pumping of the remaining atom population in $|a\rangle$. Then Rydberg Rabi oscillations are performed via single photon, resonant excitation of the 5s5p $^3P_0\,|g\rangle \leftrightarrow$ 5s61s $^3S_1\,|r\rangle$ UV Rydberg transition (317nm). At the end of the Rydberg laser pulse, we implement a high fidelity auto-ionization based detection scheme. To detect atoms in $|r\rangle$ we excite the core electron from a $5s$ to a $5p$ level with 408nm light, which then rapidly auto-ionizes the Rydberg electron, and makes the ionized atom dark to subsequent imaging of $|g\rangle$. Atoms in $|g\rangle$ are detected by transferring the population back to $|a\rangle$ and using blue fluorescence imaging of $|a\rangle$.

In the non-interacting regime, resonant excitation acts as a local X-rotation about the Bloch sphere for the Rydberg qubit defined by $|g\rangle$ and $|r\rangle$. In the strongly-interacting regime, the Rydberg-blockade effect prevents the excitation of both atoms to the Rydberg state resulting in entanglement between the two atoms. In this case a blockaded π-pulse results in the generation of a symmetric bell state of the two atoms. Further, several schemes have been proposed [36, 16, 29] (and realized with alkali atoms [16, 24]) to utilize the Rydberg blockade effect for entangling gates among qubits utilizing long-lived atomic states. These schemes can be readily adapted to AEA experiments using for example $|a\rangle$ and $|g\rangle$ as the qubit states and using $|r\rangle$ only for entangling operations.

Chapter 2

LIGHT-MATTER AND ATOM-ATOM INTERACTIONS

In this chapter, we shall summarize how atoms interact with a classical electromagnetic field and how two atoms at a distance interact with each other. There is extensive literature covering these topics and hence we shall only present a brief overview here. For the case of light-matter interaction, we shall first present the standard derivation of the rotating wave Hamiltonian for an atom interacting with a monochromatic classical electromagnetic field. We shall then generalize this derivation to the case of a laser with classical intensity and phase/frequency noise. For the atom-atom interaction, we shall focus on the case of van der Waals (dipole-dipole) interactions between Rydberg states which are relevant for our experimental setting.

2.1 Rotating Wave Hamiltonian

This section is based on [37]. We begin by describing how an atom interacts with a classical electromagnetic field. We treat the atom as a two-level system (2LS) with ground state $|g\rangle$ and excited state $|e\rangle$ and an energy splitting $\hbar\omega_A$. We shall occasionally use $|r\rangle$ for the excited state to indicate a Rydberg state. We can write the atomic Hamiltonian H_A in the basis of the ground and excited state as:

$$H_A = -\frac{\hbar\omega_A}{2}\sigma^z \tag{2.1}$$

where σ^μ represent the spin-1/2 Pauli matrices for $\mu = \{x, y, z\}$. Let the λ be the wavelength of the incident light, ω_L be the angular frequency and $k = 2\pi/\lambda$ be the wavenumber. Further let the direction of propagation of the EM wave be along the x-axis. Then the propagating electric field is varies with position and time as given by a travelling wave $\propto \cos(kx - \omega_L t - \phi)$ where ϕ is some arbitrary phase offset. Define Ω be the bare Rabi frequency, which characterizes the strength of the atom-field coupling. Then we can write the atom-field interaction Hamiltonian as:

$$H_{AF}(t) = \hbar\Omega\cos(kx - \omega_L t - \phi)\sigma^x \tag{2.2}$$

The angular frequencies involved in these Hamiltonians are very large with extremely short associated time-scales. We would like to make a frame trans-

formation that eliminates this fast oscillation and reveals the slow dynamics relevant on experimental time-scales. This is the essence of the Rotating Wave Approximation (RWA). This frame transformation is identical to the interaction picture formalism with an added approximation to drop fast-oscillating terms. In terms of the interaction picture, define a "bare" Hamiltonian H_R, and the associated time-evolution operator $U_R(t)$ as:

$$H_R = -\frac{\hbar\omega_L}{2}\sigma^z \tag{2.3}$$

$$\begin{aligned} U_R(t) &= \exp\left(\frac{-iH_R t}{\hbar}\right) \\ &= \exp\left(\frac{i\omega_L t}{2}\sigma^z\right) \end{aligned} \tag{2.4}$$

Then the interaction picture Hamiltonian $H_I(t)$ is given by:

$$H_I(t) = U_R(t)^\dagger (H_A + H_{AF}(t)) U_R(t) - H_R \tag{2.5}$$

Further let us decompose the cosine term in $H_{AF}(t)$ as a sum of exponentials. We shall make use of the fact that $e^{-i\alpha\sigma^z}\sigma^x e^{i\alpha\sigma^z} = (e^{2i\alpha}\sigma^+ + e^{-2i\alpha}\sigma^-)$ where $\sigma^+ = |e\rangle\langle g|$ and $\sigma^- = |g\rangle\langle e|$. We define $\Delta = \omega_L - \omega_A$ to be the detuning of the laser (in angular frequency) with respect to the atomic transition (angular) frequency. This gives us:

$$\begin{aligned} H_I(t) &= \frac{\hbar\Delta}{2}\sigma^z + \frac{\hbar\Omega}{2}\left(e^{i(kx-\omega_L t-\phi)} + e^{-i(kx-\omega_L t-\phi)}\right)\left(e^{i\omega_L t}\sigma^+ + e^{-i\omega_L t}\sigma^-\right) \\ &= \frac{\hbar\Delta}{2}\sigma^z + \frac{\hbar\Omega}{2}\left(e^{i(kx-\phi)}\sigma^+ + e^{-i(kx-\phi)}\sigma^-\right) \\ &\qquad + \frac{\hbar\Omega}{2}\left(e^{i(kx-2\omega_L t-\phi)\sigma^-} + e^{-i(kx-2\omega_L t-\phi)}\sigma^+\right) \\ H_I &\approx \frac{\hbar\Delta}{2}\sigma^z + \frac{\hbar\Omega}{2}\left(e^{i(kx-\phi)}\sigma^+ + e^{-i(kx-\phi)}\sigma^-\right) \end{aligned} \tag{2.6}$$

In the last line we make the rotating wave approximation and drop the fast oscillating terms. This gives us a time-independent rotating wave Hamiltonian which governs the slow dynamics of the system in the laser frame of reference (as opposed to the lab frame of reference). Restricting to just the electronic degrees of freedom, we can treat the e^{ikx} factor as just a phase factor. This is a good approximation for many experiments where the translational degrees of freedom are not as important, for example at low temperatures and when the experiment is conducted in free flight.

2.2 2LS General Solution

Here we show the general solution for the driven two-level system (2LS). In matrix form the Hamiltonian is given by:

$$H = \frac{\hbar}{2}\begin{bmatrix} \Delta & \Omega e^{-i\phi} \\ \Omega e^{i\phi} & -\Delta \end{bmatrix} \tag{2.7}$$

We can define $\bar{\Omega}$ to be generalized Rabi frequency given by $\bar{\Omega} = \sqrt{\Omega^2 + \Delta^2}$. Let us define an angle θ using the relations:

$$\cos\theta = \frac{\Delta}{\bar{\Omega}} = \frac{\Delta}{\sqrt{\Omega^2+\Delta^2}}, \qquad \sin\theta = \frac{\Omega}{\bar{\Omega}} = \frac{\Omega}{\sqrt{\Omega^2+\Delta^2}} \tag{2.8}$$

Then we can diagonalize the Hamiltonian H with the unitary U as $H = UDU^\dagger$ where D is a diagonal matrix. The unitary U and the diagonal matrix (of eigen-energies) are given by:

$$U = \begin{bmatrix} \cos\frac{\theta}{2} & \sin\frac{\theta}{2}e^{-i\phi} \\ \sin\frac{\theta}{2}e^{i\phi} & -\cos\frac{\theta}{2} \end{bmatrix}, \qquad D = \begin{bmatrix} \frac{\sqrt{\Omega^2+\Delta^2}}{2} & \\ & -\frac{\sqrt{\Omega^2+\Delta^2}}{2} \end{bmatrix} \tag{2.9}$$

Thus the eigenstates of the Hamiltonian are:

$$|E_+\rangle = \begin{pmatrix} \cos\frac{\theta}{2} \\ \sin\frac{\theta}{2}e^{i\phi} \end{pmatrix}, \qquad |E_-\rangle = \begin{pmatrix} \sin\frac{\theta}{2}e^{i\phi} \\ -\cos\frac{\theta}{2} \end{pmatrix} \tag{2.10}$$

2.3 RWA Hamiltonian for noisy case

Now we generalize the derivation of the rotating wave Hamiltonian for the case when the driving laser has intensity and phase fluctuations. Instead of eq. 2.2, we have the following noisy atom-field coupling Hamiltonian.

$$H_{AF}(t) = \hbar\Omega(t)\cos\left(kx - \omega_L t - \phi(t)\right)\sigma^x \tag{2.11}$$

Here $\Omega(t)$ represents the fluctuating Rabi frequency as a result of fluctuating laser intensity and $\phi(t)$ represents the fluctuating laser phase. We shall make a frame transformation as before to follow the laser frame of reference. We make the assumption that the laser's phase $\phi(t)$ is a differentiable function of time. For any physical process we can expect $\phi(t)$ to at least be a continuous function. However, its derivative need not be continuous. Yet we can still treat $\phi(t)$ to be approximately differentiable in some coarse-grained sense. This is because at the level of the rotating wave approximation, we are only concerned with terms in the Hamiltonian that do not get averaged out are relevant on

experimentally observable timescales. If we average $\phi(t)$ over some small time-window $\Delta t \sim 1/\omega_A$ then the discontinuities in the derivative of $\phi(t)$ vanish (as long as $\phi(t)$ is continuous, which is a physically reasonable assumption).

To transform to the laser frame, as opposed to eq. (2.3), we define the bare Hamiltonian $H_R(t)$ and associated time-evolution operator as:

$$H_R(t) = -\frac{\hbar(\omega_L + \dot{\phi}(t)}{2}\sigma^z \tag{2.12}$$

$$\begin{aligned} U_R(t) &= \exp\left(\frac{-i}{\hbar}\int_0^t H_R(t')dt'\right) \\ &= \exp\left(\frac{i(\omega_L t + \phi(t))}{2}\sigma^z\right) \end{aligned} \tag{2.13}$$

This gives us the interaction picture Hamiltonian

$$H_I \approx \frac{\hbar(\Delta + \dot{\phi}(t))}{2}\sigma^z + \frac{\hbar\Omega(t)}{2}\left(e^{ikx}\sigma^+ + e^{-ikx}\sigma^-\right) \tag{2.14}$$

Define $\nu(t) = \dot{\phi}(t)$ be the instantaneous frequency noise of the laser. Then by construction $\nu(t)$ is a stationary random variable, meaning that its first moment vanishes, $\overline{\nu(t)} = 0$. If $|\nu(t)| \ll \Omega$ then we can treat the laser frequency fluctuations perturbatively. Let us also separate $\Omega(t)$ into its static component Ω and its fluctuating component $\Omega\epsilon(t)$, i.e. $\Omega(t) = \Omega(1 + \epsilon(t))$. Then $\epsilon(t)$ is also a stationary variable $\overline{\epsilon(t)} = 0$. If $|\epsilon(t)| \ll 1$, then we can also treat the laser intensity fluctuations perturbatively. We write the Hamiltonian as the sum of a noise free Hamiltonian H_0 and a stationary perturbation Hamiltonian $H_1(t)$. Ignoring the translational degrees of freedom, we can work in a two-level system.

$$H_0 = \frac{\hbar\Delta}{2}\sigma^z + \frac{\hbar\Omega}{2}\sigma^x \tag{2.15}$$

$$H_1(t) = \frac{\hbar\nu(t)}{2}\sigma^z + \frac{\hbar\Omega\epsilon(t)}{2}\sigma^x \tag{2.16}$$

We shall find the perturbative effect of noise on Rabi oscillations in Chapter 4.

2.4 Rydberg Interactions

Now we consider how two atoms interact with each other in our experimental setup. This section is based off the review of Rydberg atom experiments [12]. Rydberg states are highly excited electronic states of an atom where a valence

electron has a large principal quantum number $n \gg 1$. Two nearby atoms in Rydberg states can interact very strongly with each other via the dipole–dipole interaction. This interaction is given by the van der Waals potential.

$$H_{int} = \frac{C_6}{R^6} |rr\rangle\langle rr| \tag{2.17}$$

where R is the distance between the atoms and C_6 is the van der Waals interaction coefficient that depends on the atomic species as well as the principal quantum number. Then the interaction strength is given by $U_{vdW} = C_6/R^6$. Consider the ground state $|g\rangle$ coupled to a Rydberg state $|r\rangle$ with a resonant laser with Rabi frequency Ω. In the case of two atoms, the two-atom ground state is still resonantly coupled to the states $|gr\rangle$ and $|rg\rangle$ containing a single Rydberg excitation. However, the doubly excitated state $|rr\rangle$ is shifted out of resonance by the strong van der Waals interaction U_{vdW}. In the limit $U_{vdW} \gg \hbar\Omega$, the double excitation is energetically forbidden. This effect is known as the Rydberg blockade. See figure 2.1.

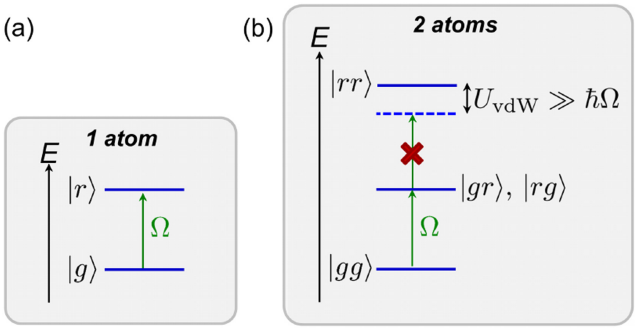

Figure 2.1: Rydberg interactions and the blockade effect. (a) A resonant laser couples the ground state $|g\rangle$ to the Rydberg state $|r\rangle$ with coupling strength Ω. (b) For two nearby atoms, the van der Waals interaction U_{vdW} shifts the doubly excited state $|rr\rangle$, preventing the double excitation of the atomic pair when $U_{vdW} \gg \hbar\Omega$. Figure from [12]

Specifically, the laser couples the ground state $|G\rangle = |gg\rangle$ only to the symmetric collective state $|W\rangle = \frac{1}{\sqrt{2}}(|rg\rangle + |gr\rangle)$. The anti-symmetric collective state $|D\rangle = \frac{1}{\sqrt{2}}(|rg\rangle - |gr\rangle)$ is dark to the laser excitation. And the doubly excited state $|R\rangle = |rr\rangle$ is energetically forbidden. Thus the dynamics of the system prepared in the ground state follow that of a two-level system comprised of just $|G\rangle$ and $|W\rangle$ with collectively enhanced Rabi frequency $\sqrt{2}\Omega$. The state $|W\rangle$ is maximally entangled. Thus we can entangle two atoms by simply performing a resonant pi-pulse in the blockaded regime. We shall consider the fidelity of

such an entangling operation in the presence of noise and other decoherence in Chapters 4 and 5. Ultimately, to generate entanglement that is useful from a quantum computing perspective, we would like to entangle two atoms in long-lived states such as hyperfine or metastable clock states. This blockade effect was proposed in [36] precisely as a means of implementing fast quantum gates between long-lived states in neutral atoms.

Chapter 3

TECHNICAL NOISE

There are two main sources of technical noise in our experiment, namely intensity noise and frequency noise on the UV Rydberg laser. For an ideal laser, the laser's phase would be perfectly coherent and it's intensity perfectly stable over time. However, in any real laser, this is not the case. The laser's intensity fluctuates with time resulting in fluctuations in the Rabi frequency for the atoms. And the laser's phase drifts manifesting as frequency noise for the atoms. We briefly describe how these noise sources are measured in the lab and report our measured noise power spectral densities (PSDs).

3.1 Laser intensity noise

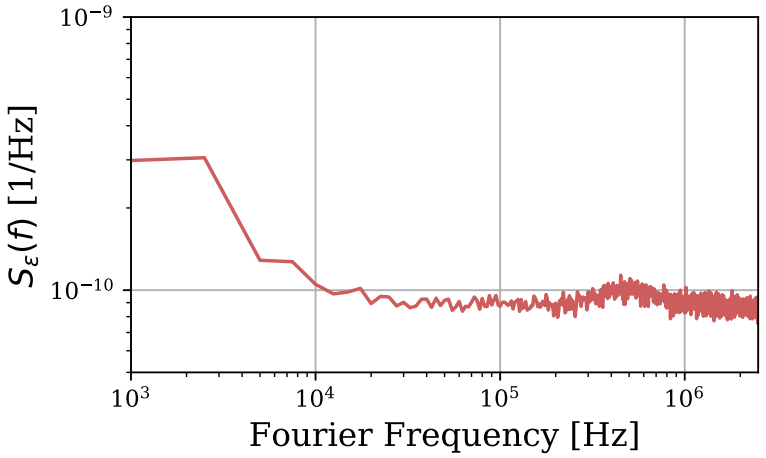

Figure 3.1: Laser intensity noise power spectral density (PSD)

The intensity noise of a laser can be measured using a fast photo-diode. Let $I(t)$ be the actual intensity of the laser as a function of time with mean value $I_0 = \overline{I(t)}$. Let $\Delta I(t) = I(t) - I_0$ be the intensity fluctuation of the laser. The voltage measured from the photo-diode is proportional to the laser intensity. Thus we can shine the laser directly onto a fast photo-diode and record time traces of the output voltage, call it $V_I(t) = \kappa I(t)$ with mean value $V_0 = \overline{V(t)}$. Let $\Delta V(t) = V(t) - V_0$ be the voltage fluctuation of the photo-diode output voltage. Then we can see that since $V \propto I$, the relative voltage fluctuation is equal to the relative intensity fluctuation, i.e. $\Delta V(t)/V_0 = \Delta I(t)/I_0$.

Now the (time dependent) Rabi frequency $\Omega(t)$ is proportional to the square root of the laser intensity, i.e. $\Omega(t) \propto \sqrt{I(t)}$. Assuming the noise to be Gaussian distributed, we can approximate the relative fluctuations in Rabi frequency to be half the relative fluctuations in laser intensity. This assumption is valid when the relative fluctuations are small compared to the mean. Just as before we define $\Omega(t) = \Omega(1 + \epsilon(t))$. Thus our approximation is that

$$\epsilon(t) \approx \frac{1}{2}\frac{\Delta I(t)}{I_0} = \frac{1}{2}\frac{\Delta V(t)}{V_0} \tag{3.1}$$

Thus using the voltage time trace $V(t)$, we can calculate the auto-correlation function for relative Rabi frequency noise K_ϵ given by:

$$K_\epsilon(\tau) = \overline{\epsilon(t)\epsilon(t+\tau)} \tag{3.2}$$

Since the noise variable $\epsilon(t)$ is real, the auto-correlation function is an even function, $K_\epsilon(\tau) = K_\epsilon(-\tau)$. Using $K_\epsilon(\tau)$ we can calculate the power spectral density $S_\epsilon(\omega)$ via a Fourier transform.

$$S_\epsilon(\tau) = \int d\tau e^{i\omega\tau} K_\epsilon(\tau) = \int d\tau \cos\omega\tau K_\epsilon(\tau) \tag{3.3}$$

The laser intensity noise PSD measured for our Rydberg laser is shown in Figure 3.1. There are three main features in the spectrum. First, we see that there is a peak in the PSD for low Fourier frequencies. This means that there is a strong contribution from very slow fluctuations in the intensity. We call this low frequency contribution the 'shot-to-shot' noise, i.e. noise which varies from one shot of the experiment to the next, but is essentially static over the course of a single shot. Second, we see that for the majority of the spectrum, the noise PSD is constant. This nearly frequency independent contribution is the 'white' noise contribution. Finally, there is a small peak in the noise at about 500 kHz. This peak comes from the conversion of frequency noise to intensity noise in an optical cavity. We shall discuss this in the next section.

3.2 Laser Frequency noise

Our Rydberg laser system is described in detail in [17]. We generate UV light at $\lambda_{\mathrm{UV}} = 316.6$ nm from an infrared extended cavity laser diode (ECDL) at $\lambda_{\mathrm{IR}} = 1266.6$ nm using two frequency doubling cavities. The fundamental laser (IR) is stabilized to an ultralow expansion (ULE) optical cavity using the Pound-Drever-Hall (PDH) method [38]. We use the in-loop PDH error

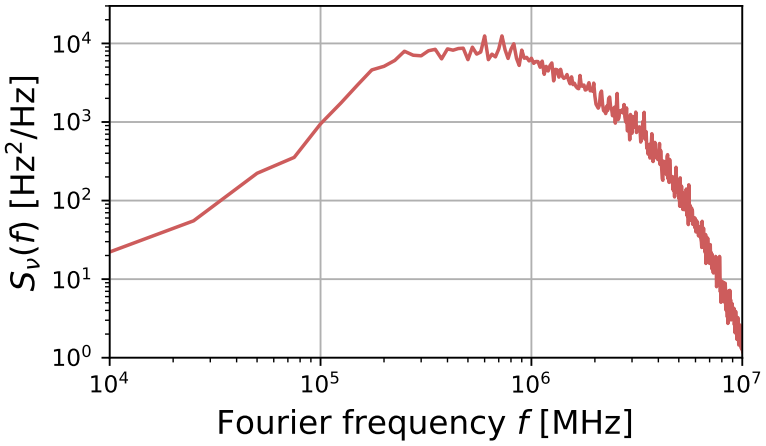

Figure 3.2: Laser frequency noise power spectral density

signal derived from the cavity reflection to extract a frequency noise spectrum as detailed in [39, 40]. We summarize this procedure below for completeness.

We measure the reflected light from the ULE cavity using a photo-diode and a spectrum analyzer. This gives us the electrical power spectral density for the photo-diode output voltage. From the calibration of the PDH locking signal, we can convert the photo-diode voltage to laser frequency noise f measured relative to the cavity resonance frequency f_0, i.e. $f = f_{laser} - f_0$. Thus we obtain a frequency noise power spectral density for the laser light reflected off the cavity. However, we wish to obtain the frequency noise PSD of the light incident on the cavity rather than the light reflected off the cavity. Thus we need to correct for the cavity roll-off factor (CRF) associated with the Fabry-Perot cavity, given by [39, 41]:

$$\mathrm{CRF}_{\mathcal{F},\nu_c}(f) = \frac{1}{\mathcal{F}} + \frac{1 - 1/\mathcal{F}}{1 + \left(\frac{2f}{\nu_c}\right)^2} \tag{3.4}$$

where $\mathcal{F}$ is the finesse of the cavity, ν_c is the cavity linewidth (FWHM) and f is the frequency noise measured relative to the cavity resonance. We measure our cavity finesse to be $\approx$ 14000 using ringdown spectroscopy [42] and our cavity linewidth to be $\approx$ 110 kHz. Dividing by this cavity roll-off factor, we obtain the frequency noise PSD for the IR light incident on the cavity.

In our laser system, the IR light is frequency doubled twice in two bowtie cavities. This doubling has two effects on the frequency noise PSD. First, since the frequency is quadrupled, the frequency noise PSD increases by a factor of

16 (since the PSD is the second moment of the noise). However, in addition, when the light passes through the two bowtie cavities, the cavities filter the frequency noise [14] imparting a cavity roll-off factor to the transmitted light. The bowtie cavities have a finesse of ≈ 150 and a cavity linewidth of ≈ 7 MHz. Multiplying by the factor of 16 and the two cavity roll-off factors for the two cavities, we obtain the frequency noise PSD for the UV light.

The laser frequency noise PSD measured for our Rydberg laser is shown in Figure 3.2. We see that the PDH locking suppresses frequency noise below the cavity linewidth of ≈ 110 kHz. Additionally, we see that there is a broad peak in the frequency noise at about 500 kHz. This is the 'servo bump' of the PDH lock. Since the typical Rabi frequency is larger than the cavity linewidth, the servo bump has a significant contribution to the Rabi infidelity. At higher Fourier frequencies, the frequency noise PSD tapers off very quickly (partly because of the cavity filteration). The cavity filteration also results in some of the laser frequency noise being converted to laser intensity noise. We see some evidence of this in the measured intensity noise PSD. The broad servo bump at ~ 500 kHz shows up as a small peak in the intensity noise at ~ 500 kHz as seen in Figure 3.1.

3.3 Numerics

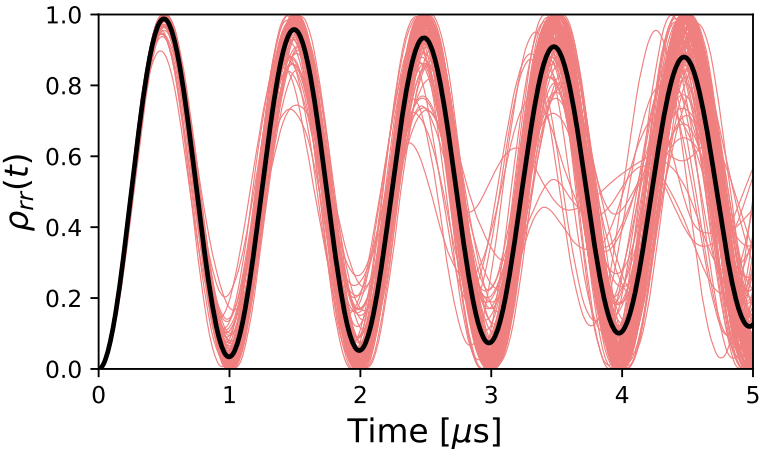

Figure 3.3: Numerically simulated noisy single atom Rabi oscillations. Here we consider the effects of intensity noise and frequency noise for Rabi frequency $\Omega = 2\pi \times 1$ MHz. The red curves are the individual traces of the population $\rho_{rr}(t)$ for randomly generated instances of $\epsilon(t)$ and $\nu(t)$. The black curve is the average of the red curves, i.e., $\overline{\rho_{rr}(t)}$.

In this section we discuss how to perform the numerical simulation of laser intensity and frequency noise. We start with measured power spectral density of the noise source, generate time-traces of the noise term in our Hamiltonian, numerically simulate the time-dependent Schrodinger equation, and average over many (typically ~ 100) independently generated noise time-traces.

To generate the time-traces we follow the procedure from [39] summarized below. Let $S_X(f)$ be the power spectral density of a stationary, random, real process $X(t)$. Let the Fourier component of $X(t)$ with frequency f be written as $A_f \cos(2\pi f t + \phi_f)$. When we measure the power spectrum $S_X(f)$ in a real system, we can only measure it at discrete frequencies with frequency spacing Δf. In this case, the amplitude of the Fourier component of $X(t)$ with frequency f is given by $A_f = 2\sqrt{S_X(f)\Delta f}$ where the factor of 2 comes from the positive and negative frequency components (for a real signal $S_X(f) = S_X(-f)$). Since the different Fourier components in a random process are uncorrelated, to generate a noise time-trace, we add them with random phase offsets ϕ_f sampled uniformly, $\phi_f \in [0, 2\pi)$.

$$X(t) = \sum_f 2\sqrt{S_X(f)\Delta f}\cos(2\pi f t + \phi_f) \tag{3.5}$$

We use this equation to generate $\epsilon(t)$ and $\nu(t)$. Using these time traces, we numerically simulate the time-dependent Hamiltonians using the Runge-Kutta method. In Figure 3.3, we show a sample numerical simulation of the effect of frequency and intensity noise using the measured PSDs at a Rabi frequency of $\Omega = 2\pi \times 1$ MHz.

Chapter 4

ANALYSIS OF NOISY RABI OSCILLATIONS

The fidelity of single qubit operations as well as two-qubit entangling gates is limited by several decoherence channels of which the dominant ones are laser intensity noise and frequency noise and atomic motion. Here we present analytical expressions for the effect of these noise sources on the Rabi oscillations of a single atom and a pair of atoms in the Rydberg blockaded regime. We derive this result in terms of the power spectral density of the noise sources and use it to predict the maximum achievable single and two-qubit gate fidelities.

4.1 Introduction

The important noise sources in experiments involving laser-driven, optically trapped neutral atoms include laser noise, atomic motion at finite temperature, black body radiation, off-resonant scattering from the trap potential, imperfect pulse control, and state detection and preparation errors. Previous works have numerically and experimentally studied these noise sources for Rabi oscillations in single atoms [32]. There has also been theoretical analysis of the effect of white noise (Markovian approximation) on atomic spectroscopy [43, 44] and on the time dynamics in the context of stochastic differential equations [45, 46]. However, the noise sources in a real experiment are often far from Markovian and this non-Markovian behavior can have an important role on the decoherence. The effect of non-Markovian, time-dependent noise sources has been studied previously in solid-state isolated systems using a cluster expansion method [47] and also in many-body interacting systems using a resonance counting method [48]. However, here we present a simple description of the effect of non-Markovian noise sources on Rabi oscillations of isolated and interacting Rydberg atoms using time-dependent perturbation theory. We solve for the early-time dynamics focusing on the effect of laser intensity noise, laser frequency noise and atomic motion at finite temperature. Our result provides upper bounds on achievable single and two-qubit gate fidelities for given noise spectra, and also provides guidance to make improvements to these fidelities by appropriately modifying servo-controls of the laser systems.

In Section 4.2, we analyze Rabi oscillations in a single Rydberg atom. Our

main result is a perturbative solution of the effect of non-Markovian frequency noise based on a simple window-function picture applied to experimentally measurable noise spectra. These analytic time-dependent 'window functions' allow us to quantitatively understand how different spectral components of the noise play a role in the decoherence dynamics. In particular, they explain the particular sensitivity of Rabi oscillations to frequency noise near the Rabi frequency and intensity noise near zero frequency.

In Section 4.3, we analyze Rabi oscillations in a pair of strongly interacting Rydberg atoms. By appropriately changing basis, the same analysis of intensity and frequency noise from Sec. 4.2 can be applied here as well. For the atomic motional effects we find that while the center-of-mass motion of the atoms leads to similar decoherence as the single atom case, the relative motion of the atoms couples to an undesired dark state.

4.2 Single Atom Rabi Oscillations

We consider a single atom (two-level system) driven on resonance as our bare Hamiltonian. In the absence of a trapping potential, as is typical for Rydberg atom experiments, the Hamiltonian is given by:

$$H_0 = \frac{\hbar\Omega}{2}\sigma^x \tag{4.1}$$

where Ω is the Rabi frequency and σ^μ is the spin-1/2 Pauli operator ($\mu = x, y, z$). Working in the density matrix formalism, $\rho(t) = |\Psi(t)\rangle\langle\Psi(t)|$ and starting in the ground state, $\rho(0) = |g\rangle\langle g|$, the bare density matrix evolves as:

$$\rho_0(t) = \begin{bmatrix} \frac{1}{2}(1+\cos\Omega t) & \frac{i}{2}\sin\Omega t \\ -\frac{i}{2}\sin\Omega t & \frac{1}{2}(1-\cos\Omega t) \end{bmatrix} \tag{4.2}$$

We consider a perturbation Hamiltonian given by:

$$H_1(t) = \frac{\hbar\Omega\epsilon(t)}{2}\sigma^x + \frac{\hbar\nu(t)}{2}\sigma^z \tag{4.3}$$

The $\epsilon(t)$ term accounts for fractional fluctuations in the drive strength experienced by the atoms arising from laser intensity noise, beam pointing instability or pulse timing errors. This term commutes with the bare Hamiltonian and is thus its effect is exactly soluble. The $\nu(t)$ term accounts for fluctuations in the frequency of the laser experienced by the atoms, including laser frequency noise as well as the Doppler shift of the transition caused by thermal motion

of the atom (discussed further in Sec. 4.2). This term does not commute with the bare Hamiltonian and its effect is thus not exactly soluble in general.

We assume that the noise sources are real, stationary (time-translation invariant), Gaussian distributed and statistically independent. Thus,

$$\overline{\nu(t)} = \overline{\epsilon(t)} = 0 \quad \text{(stationary)} \tag{4.4}$$

$$\overline{\nu(t)\epsilon(t')} = 0 \quad \text{(independent)} \tag{4.5}$$

where $\overline{X}$ denotes the ensemble average of X. The noise sources are characterized by their covariance, i.e., two-point correlation function denoted by $K(\tau)$:

$$K_\epsilon(\tau) = \overline{\epsilon(t)\epsilon(t+\tau)} \tag{4.6}$$

$$K_\nu(\tau) = \overline{\nu(t)\nu(t+\tau)} \tag{4.7}$$

Since the noise sources are real, $K(\tau) = K(-\tau)$. The power spectral density (PSD) of the noise is given by the Fourier transform of the two-point correlation function and is denoted by $S(\omega)$:

$$S(\omega) = \int d\tau \cos\omega\tau K(\tau) \tag{4.8}$$

In the following, we individually calculate the effect of each noise source and sum up their contributions to get the net effect. To quantify the decoherence of the Rabi oscillations we examine the ensemble-averaged excited state population, $\overline{\rho_{rr}(t)} = \overline{\langle r|\,\rho(t)\,|r\rangle}$. The π-pulse fidelity $\mathcal{F}_\pi$, which is the fidelity of a single qubit bit-flip gate, is given by

$$\mathcal{F}_\pi = \overline{\rho_{rr}(\pi/\Omega)} \tag{4.9}$$

Intensity Noise (Integrable)

We first analyze the effect of just intensity fluctuations. The corresponding perturbing Hamiltonian is give by:

$$H_1(t) = \frac{\hbar\Omega\epsilon(t)}{2}\sigma^x \tag{4.10}$$

Note that this perturbation commutes with the bare Hamiltonian. Thus we calculate the ensemble-averaged excited state population, $\overline{\rho_{rr}(t)}$, using a similar approach as provided in [49].

$$\overline{\rho_{rr}(t)} = \frac{1}{2} - \frac{\cos\Omega t}{2}\; e^{-\frac{\Omega^2}{2}\int_0^t dt_1 \int_0^t dt_2 K_\epsilon(t_2-t_1)} \tag{4.11}$$

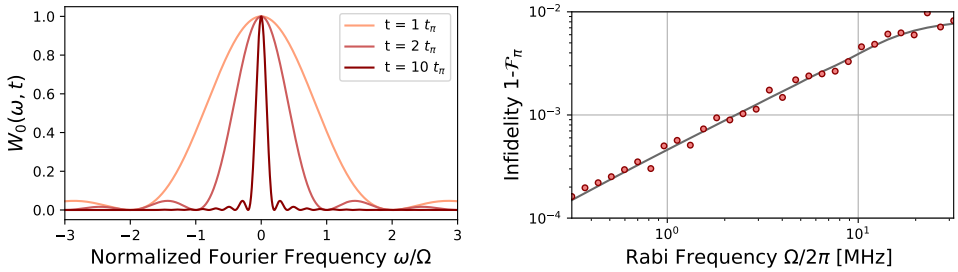

(a) (b)

Figure 4.1: Intensity noise effects on single atom Rabi oscillations (a) Window functions, $W_0(\omega, t)$, at three different Rabi interrogation times. The effect of the noise on the excited population is proportional to the area under $W_0(\omega, t) \times S_\epsilon(\omega)$. The window function selects the near-DC components of the intensity noise PSD. (c) Infidelity of a π-pulse (1 - $\mathcal{F}_\pi$). The red dots are generated using numerical simulation using the measured PSD (see chapter **??** for details) and the gray curve is from Eq. (4.16). Note that the fidelity reduces for higher Rabi frequency since the width of the window function is proportional to the Rabi frequency.

Using this general expression (Eq. 4.11) we can analyze three different noise profiles of interest:

- Shot-to-shot noise:

$$\overline{\rho_{rr}(t)} = \frac{1}{2} - \frac{\cos\Omega t}{2} \exp\left(\frac{-t^2}{\tau_1^2}\right) \tag{4.12}$$

  where we use $K_\epsilon(t) = \sigma_\epsilon^2$ in which σ_ϵ is the standard deviation of the fractional laser intensity noise and $\tau_1 = \frac{\sqrt{2}}{\Omega\sigma_\epsilon}$ is the $1/e$ Rabi decoherence time. This gives us a *Gaussian* decay profile and gives a π-pulse fidelity of $\mathcal{F}_\pi = \exp\left(\frac{-\pi\sigma_\epsilon}{\sqrt{2}}\right)$.

- White noise:

$$\overline{\rho_{rr}(t)} = \frac{1}{2} - \frac{\cos\Omega t}{2} \exp\left(\frac{-t}{\tau_2}\right) \tag{4.13}$$

  where we use $K_\epsilon(t) = \alpha_\epsilon\delta(t)$ and $\tau_2 = \frac{2}{\alpha_\epsilon\Omega^2}$ is the $1/e$ Rabi decoherence time. This gives an *exponential* decay profile and gives a π-pulse fidelity of $\mathcal{F}_\pi = \exp\left(\frac{-\pi\alpha_\epsilon\Omega}{2}\right)$.

- Non-Markovian noise:

  When the noise is neither shot-to-shot nor white, we can still write a

convolution-less solution by writing the two-point correlation function in terms of the PSD, (see Eq. (4.8)). This gives us:

$$\overline{\rho_{rr}(t)} = \frac{1}{2} - \frac{\cos\Omega t}{2}\ e^{-\frac{\Omega^2 t^2}{2}\int \frac{d\omega}{2\pi} S_\epsilon(\omega) W_0(\omega,t)} \tag{4.14}$$

where W_0 is a time-dependent 'window' function on the noise PSD defined as:

$$W_0(\omega,t) = \left(\frac{\sin(\omega t/2)}{(\omega t/2)}\right)^2 \tag{4.15}$$

Figure 4.1(a) shows a plot of the window function as a function of normalized Fourier frequency ω/Ω, for different values of time t. This window function is centered around zero frequency, and has a width of $\sim 2\pi/t$. At short times, the atom is sensitive to almost all the spectral components of the noise, while at long times, the atom picks out only the low frequency components of the PSD. The resultant decay profile is generically neither Gaussian nor exponential and gives a π-pulse fidelity of

$$\mathcal{F}_\pi = \exp\left(\frac{-\pi^2}{2}\int \frac{d\omega}{2\pi} S_\epsilon(\omega) W_0(\omega,t)\right) \tag{4.16}$$

Using the experimentally measured intensity noise PSD (figure **??**) and equation (4.16), we can calculate the effect of just intensity nosie on the π-pulse fidelity as a function of Rabi frequency. See figure 4.1(b).

Frequency Noise

Here we consider the case of non-Markovian frequency noise, neglecting any intensity noise:

$$H_1(t) = \frac{\hbar\nu(t)}{2}\sigma^z \tag{4.17}$$

This perturbing Hamiltonian does not commute with the bare Hamiltonian. While the case of case of shot-to-shot noise (see Sec. 4.2) and white noise [45, 46] (also see Appendix A.4) can be solved exactly, in practice, laser frequency noise is neither shot-to-shot nor white, as we can see from figure **??**. Thus, we resort to a perturbative analysis to analytically derive resultant time dynamics for arbitrary frequency noise. In the interaction picture, the perturbing Hamiltonian is given by $\bar{H}_1(t) = U_0(t)^\dagger H_1(t) U_0(t)$ where $U_0(t) = e^{-iH_0 t/\hbar}$ is the 'free' time evolution operator.

$$\bar{H}_1(t) = \frac{\hbar\nu(t)}{2}(\cos\Omega t\ \sigma^z + \sin\Omega t\ \sigma^y) \tag{4.18}$$

The full (perturbed) time-evolution operator $U(t)$ gets modified from the bare one as:

$$U(t) = U_0(t)\Big[e^{-\frac{i}{\hbar}\int_0^t dt' \bar{H}_1(t')}\Big]_T \tag{4.19}$$

where $[...]_T$ denotes time-ordering. Starting from an initial state of $\rho(0) = |g\rangle\langle g|$, we can use this formal solution expanded order by order to compute the excited state population as $\rho_{rr}(t) = \langle r| U(t)\rho(0)U(t)^\dagger |r\rangle = |\langle r| U(t) |g\rangle|^2$.

Explicitly writing out the matrix element $\langle r| U(t) |g\rangle$ to 2nd order in perturbation, we have:

$$\langle r| U(t) |g\rangle = -i \sin\frac{\Omega t}{2} - \frac{1}{2}\int_0^t dt_1 \nu(t_1)\left(\sin\frac{\Omega t}{2}\cos\Omega t_1 - \cos\frac{\Omega t}{2}\sin\Omega t_1\right)$$
$$+ \frac{i}{4}\int_0^t dt_1 \int_0^{t_1} dt_2 \nu(t_1)\nu(t_2)\left(\sin\frac{\Omega t}{2}\cos\Omega(t_1-t_2) - \cos\frac{\Omega t}{2}\sin\Omega(t_1-t_2)\right) \tag{4.20}$$

We can then compute $|\langle r| U(t) |g\rangle|^2$ to second order and average over the noise realizations making use of Eq. (4.7). See Appendix **??** for details of the calculation. The excited state population is then given by:

$$\overline{\rho_{rr}(t)} = \frac{1}{2} - \cos\Omega t\Big(\frac{1}{2} - \frac{t^2}{8}\int \frac{d\omega}{2\pi} S_\nu(\omega) W_1(\omega,\Omega,t)\Big)$$
$$+ \sin\Omega t\Big(\frac{t^2}{8}\int \frac{d\omega}{2\pi} S_\nu(\omega) W_2(\omega,\Omega,t)\Big) \tag{4.21}$$

where $S_\nu(\omega)$ is the Fourier transform of the two-point correlation function of the frequency noise (see Eq. (4.8)). Here we have defined two new window functions W_1 and W_2 to be:

$$W_1(\omega,\Omega,t) = \Big(3\Omega^2 + \omega^2 + (\Omega^2-\omega^2)\cos 2\Omega t$$
$$- 4\Omega^2 \cos\Omega t\cos\omega t - 4\Omega\omega\sin\Omega t\sin\omega t\Big)/\Big((\Omega^2-\omega^2)^2 t^2\Big) \tag{4.22}$$

$$W_2(\omega,\Omega,t) = \Big(4\Omega\omega\cos\Omega t\sin\omega t - 4\Omega^2\sin\Omega t\cos\omega t$$
$$+ (\Omega^2-\omega^2)(2\Omega t + \sin 2\Omega t)\Big)/\Big((\Omega^2-\omega^2)^2 t^2\Big) \tag{4.23}$$

See Appendix A.2 for the derivation of these window functions. In figure 4.2(a,b) we plot W_1 and W_2 as a function of normalized Fourier frequency for various Rabi pulse times t. We see that the window functions pick out

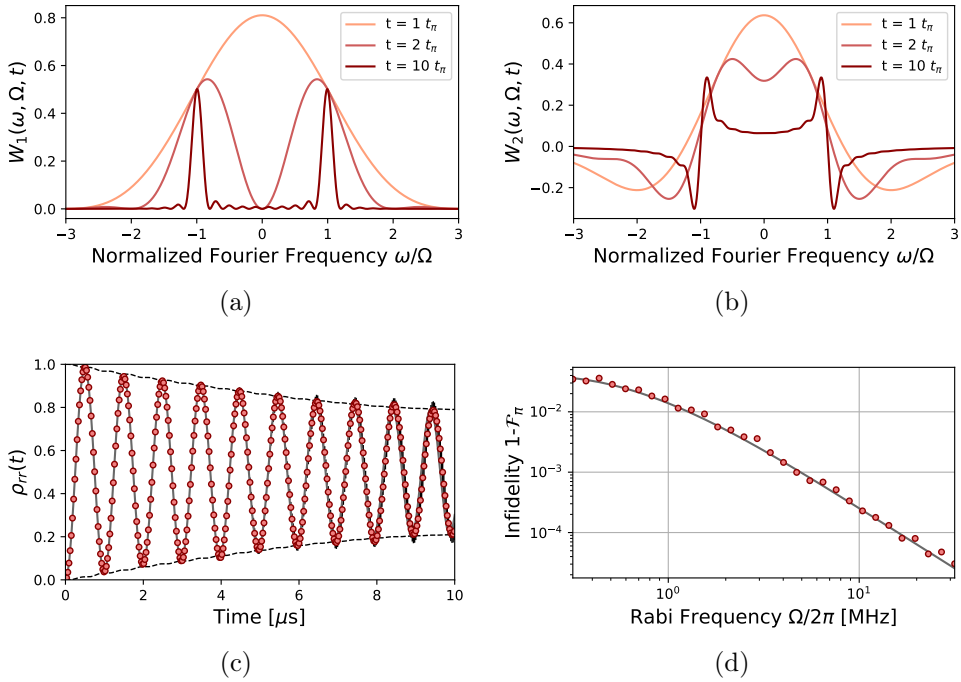

Figure 4.2: Frequency noise effects on single atom Rabi oscillations. (a,b) Window functions W_1 and W_2, probed at three different Rabi interrogation times. The effect of the noise is proportional to the area under $W_1(\omega, \Omega, t) \times S_\nu(\omega)$ and $W_2(\omega, \Omega, t) \times S_\nu(\omega)$. The window functions W_1 and W_2 at very early times are Fourier broadened from their long time limit and thus exhibit a single peak structure at early times and two sharp features at long times. (c) Rabi oscillations with frequency noise effects for $\Omega = 2\pi \times 1$ MHz. The red dots are generated using numerical simulation using the measured PSD (see Chapter **??** for details) while the gray curve is the perturbation theory result Eq. (4.21). We see good agreement between the theory and numerics at early times. (d) Infidelity of a π-pulse (1 - F_π). The red dots are generated using numerical simulation and the gray curve is from Eq. (4.24). We see that the π-pulse fidelity increases with increasing Rabi frequency.

spectral components of the noise near low frequency at early times and near Rabi frequency at late times. Thus at different times, the atoms are sensitive to different parts of the noise PSD. To minimize the decoherence at a given time, we can try to modify the PSD in a way that minimizes the overlap with the window functions at that time.

Using Eq. (4.21), we can compute the π-pulse fidelity to be:

$$\mathcal{F}_\pi = 1 - \frac{\pi^2}{4\Omega^2} \int \frac{d\omega}{2\pi} S_\nu(\omega) W_1(\omega, \Omega, \frac{\pi}{\Omega}) \tag{4.24}$$

We also compare the perturbative result of Eq. (4.21) with exact numerical

simulation of the frequency noise following the approach of [39, 50] (see Fig. 4.2(c)). We find good agreement between our perturbative calculation and exact numerics.

Motional Effects

Here we analyze the effect of a finite momentum distribution on the Rabi oscillations of Rydberg atom qubits. In this section we include the motional degrees of freedom which were previously ignored, but we work in 1D since the incoming laser beam can only change the atomic momentum along one axis (we label this as X). The drive Hamiltonian (in the rotating wave approximation) is given by:

$$H = \frac{p^2}{2m} + \frac{\hbar\Omega}{2}(e^{-ik_L x}\sigma^+ + \text{h.c.}) \tag{4.25}$$

where k_L is the wavevector of the Rydberg laser and $\sigma^+ = |r\rangle\langle g|$. We shall work in the basis $|p, s\rangle$ where $s \in (g, r)$ labels the atomic state and p is the atom's momentum. The Rabi drive couples the states $|p, g\rangle$ and $|p - \hbar k_L, r\rangle$. We can rewrite the Hamiltonian as:

$$H = \int dp\ \Gamma(p) \begin{bmatrix} \frac{p^2}{2m} & \frac{\hbar\Omega}{2} \\ \frac{\hbar\Omega}{2} & \frac{(p-\hbar k_L)^2}{2m} \end{bmatrix} \Gamma^\dagger(p) \tag{4.26}$$

where

$$\Gamma(p) = \begin{pmatrix} |p, g\rangle \\ |p - \hbar k_L, r\rangle \end{pmatrix} \tag{4.27}$$

We eliminate the term $p^2/2m$ from the diagonal which only acts as an energy offset and absorb the recoil shift term $\hbar^2 k_L^2/2m$ into the transition frequency since it is independent of momentum p. The remaining term is the effective Doppler detuning of $\delta = k_L p/m$. Starting in a pure state $\rho(0) = |p, g\rangle\langle p, g|$, the atom experiences detuned Rabi oscillations with effective Rabi frequency:

$$\Omega_{\text{eff}} = \sqrt{\Omega^2 + \delta^2} \approx \Omega(1 + \frac{\delta^2}{2\Omega^2}) \quad (\text{for } \delta \ll \Omega) \tag{4.28}$$

By tracing over the final momnetum of the atom, we can write the excited state population as $\rho_{rr}(t; p)$ where p stands for the initial momentum:

$$\rho_{rr}(t; p) = \frac{\Omega^2}{\Omega_{\text{eff}}^2} \frac{(1 - \cos\Omega_{\text{eff}} t)}{2} \tag{4.29}$$

$$\approx \frac{1 - \xi^2}{2} - \frac{1 - \xi^2}{2} \cos\left(\Omega t(1 + \frac{\xi^2}{2})\right) \tag{4.30}$$

where we have defined the normalized Doppler detuning $\xi = \delta/\Omega = \frac{k_L p}{m\Omega}$ and assume $\xi \ll 1$. Now suppose the initial state is not a pure momentum eigenstate, but is given by the density matrix:

$$\rho(0) = \int dp_1 \int dp_2 f(p_1, p_2) \, |p_1, g\rangle\langle p_2, g| \tag{4.31}$$

where $f(p_1, p_2)$ represents the coherent as well as thermal momentum distribution. Notice that the Hamiltonian does not couple different momentum eigenstates within the same electronic state. Thus, when we trace over the motional degrees of freedom, we are only left with the diagonal terms $f(p, p)$:

$$\begin{aligned}\rho_{rr}(t) &= \int dp \, \langle p, r| \, e^{-iHt/\hbar} \rho(0) e^{iHt/\hbar} \, |p, r\rangle \\ &= \int dp f(p, p) \rho_{rr}(t; p)\end{aligned}$$

Now $f(p, p)$ depends on the atomic temperature T and the details of the trapping potential from which the atom is released. For low temperatures, we can assume that the trapping potential is simply a harmonic potential $U_{trap}(x) = \frac{1}{2} m\omega^2 x^2$ where ω is the trapping frequency. Starting in a thermal state of this potential with temperature T, we can calculate $\overline{p} = 0$ and

$$\overline{p^2} = \frac{\hbar m\omega}{2 \tanh\left(\frac{\hbar\omega}{2k_B T}\right)}. \tag{4.32}$$

For very low temperatures, $k_B T \ll \hbar\omega$, the momentum variance approaches the Heisenberg limit $\overline{p^2} \to \hbar m\omega/2$. Whereas for higher temperatures, $k_B T \gg \hbar\omega$, the momentum variance approaches the classical limit $\overline{p^2} \to m k_B T$. We can approximate $f(p, p) = \mathcal{N}(0, \overline{p^2})$, i.e. a Gaussian distribution with zero mean and variance $\overline{p^2}$. This defines the variance of ξ which we denote by $\xi_0^2 = \frac{k_L^2 \overline{p^2}}{m^2\Omega^2}$. The probability distribution of ξ is $P(\xi) = \mathcal{N}(0, \xi_0^2)$.

Finally, tracing over final momentum distribution we get the following (see Appendix A.1 for details of calculation):

$$\overline{\rho_{rr}(t)} = \int d\xi P(\xi) \rho_{rr}(t; p) \tag{4.33}$$

$$\approx \frac{1 - \xi_0^2}{2} - \frac{|\sigma(t)(1 - \sigma(t)^2)|}{\xi_0} \frac{\cos\left(\Omega t + \phi(t)\right)}{2} \tag{4.34}$$

where $\sigma^2(t) = \frac{\xi_0^2}{1 - i\Omega t \xi_0^2}$ is the complex time-dependent variance that enters the averaging integral, and $\phi(t) = \arg(\sigma(t)(1 - \sigma(t)^2)$ is the Doppler-induced time-dependent phase shift. From Eq. (4.34), we identify that the Rabi signal has

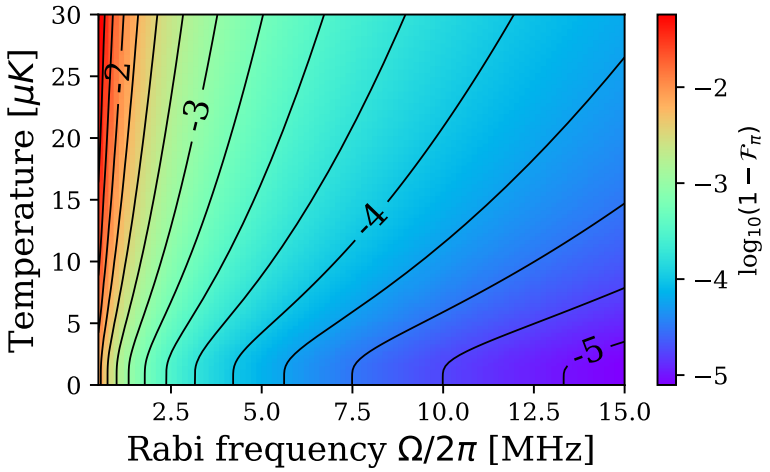

Figure 4.3: Infidelity of a π-pulse $(1-\mathcal{F}_\pi)$ plotted as a function of temperature and Rabi frequency. Here we used ^{88}Sr atoms with a trapping frequency $\omega = 2\pi \times 80$ kHz and $k_L = 2\pi/(317\text{nm})$. Considering only motional effects, the fidelity increases with Rabi frequency and decreases with temperature.

a decay timescale of $\tau = \frac{1}{\Omega\xi_0^2} = \frac{\Omega m^2}{k_L^2 \overline{p^2}}$. The π-pulse fidelity is given by:

$$\mathcal{F}_\pi = 1 - \xi_0^2 + O(\xi_0^4) = 1 - \frac{k_L^2 \overline{p^2}}{m^2\Omega^2} \tag{4.35}$$

Thus for a given temperature, going to higher Rabi frequency Ω increases the fidelity (see Fig. 4.3)

Note that tracing over the momentum distribution to find $\rho_{rr}(t)$ is identical to the case of averaging over an ensemble of experiments, each with a shot-to-shot frequency detuning δ. Hence atomic motion can be considered to be a shot-to-shot frequency noise source. If there is an additional independent source of shot-to-shot frequency noise, we can simply use an appropriately modified variance, $\xi_0^2 = \xi_{0,1}^2 + \xi_{0,2}^2$.

Combined effect

Finally, we can consider what happens when we have all three noise sources: intensity noise, frequency noise, and atomic motion. As per our assumption, these sources of noise are statistically independent and we can simply add their contributions together. From Eqs. (4.16,4.24, and 4.35), the combined

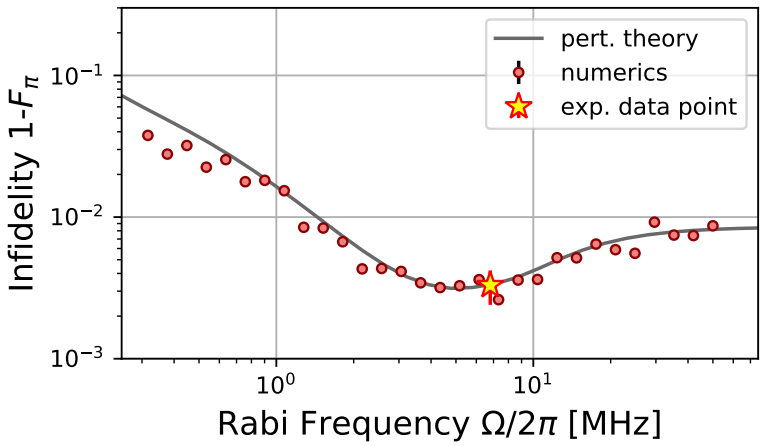

Figure 4.4: Infidelity of a π-pulse (1 - F_π) considering the effects of intensity noise, frequency noise and temperature. The red dots are generated using numerical simulation and the gray curve is from Eq. (4.36). In addition, the star marker represents the (SPAM corrected) experimentally achieved π-pulse fidelity for this system reported in [17]. We see very good agreement between numerics, our perturbative result and the experimental data point. This implies that the noise sources we have considered are indeed the only dominant ones in our experiment. At low Rabi frequency, the limiting factor is frequency noise whereas at high Rabi frequency, the limiting factor is intensity noise.

π-pulse fidelity is:

$$\mathcal{F}_\pi = 1 - \frac{\overline{\delta^2}}{\Omega^2} - \frac{\pi^2}{2}\int \frac{d\omega}{2\pi} S_\epsilon(\omega) W_0(\omega, \frac{\pi}{\Omega}) - \frac{\pi^2}{8\Omega^2}\int \frac{d\omega}{2\pi} S_\nu(\omega) W_1(\omega, \Omega, \frac{\pi}{\Omega}) \quad (4.36)$$

We also compare this result to the recent experimental work from our group [17] (see Fig. 4.4). We find very good agreement between our model and the experimentally achieved fidelity. This implies that the noise sources we have considered here are the only dominant ones in our experiment. One known decoherence source which we have ignored here is spontaneous emission. We estimate our Rydberg state lifetime to be $\approx 80\mu s$. The contribution to the π-pulse infidelity at the Rabi frequency of $\approx 2\pi \times 7$MHz is $\approx 2 \times 10^{-3}$ estimated using the integrated Rydberg state population [26]. This shifts our grey curve in figure 4.4 up, but is still within error bars of the experimental data point.

4.3 Blockaded Rabi Oscillations

When atoms are laser driven in the Rydberg-blockaded regime [26, 14], the very strong dipole-dipole interaction of the Rydberg states greatly suppresses the probability of a double excitation within the blockade radius. The atoms within the blockade radius become entangled as a result of this interaction. For the Rydberg-blockaded Rabi oscillation, the two-atom Hamiltonian is given by:

$$H = \frac{\hbar\Omega}{2}\left(e^{-ik_L x_1}\sigma_1^+ + e^{-ik_L x_2}\sigma_2^+ + \text{h.c.}\right) + V(x_1, x_2)\,|r_1 r_2\rangle\langle r_1 r_2| \tag{4.37}$$

where x_1 and x_2 are the positions of the two atoms and $V(x_1, x_2)$ is the van der Waals interaction term between the Rydberg states. In the ideal blockade, the interaction strength is infinite $V(x_1, x_2) \to \infty$. In this case, we can treat the interacting two-atom system as a three-level system with the basis states: ground state $|g\rangle$, bright state $|w\rangle$, and dark state $|d\rangle$ as defined below. In the case of finite but large Rydberg interaction strength, the blockade condition is not exact. We consider this case of in section **??**.

$$|g\rangle = |g_1 g_2\rangle \tag{4.38}$$

$$|w\rangle = \frac{e^{-ik_L x_1}\,|r_1 g_2\rangle + e^{-ik_L x_2}\,|g_1 r_2\rangle}{\sqrt{2}} \tag{4.39}$$

$$|d\rangle = \frac{e^{-ik_L x_1}\,|r_1 g_2\rangle - e^{-ik_L x_2}\,|g_1 r_2\rangle}{\sqrt{2}} \tag{4.40}$$

The bare Hamiltonian in this basis is given by (see Appendix A.3 for derivation):

$$H_0 = \frac{\hbar\Omega_2}{2} X_{gw} \tag{4.41}$$

where $\Omega_2 \equiv \sqrt{2}\ \Omega$ is the enhanced Rabi frequency and $X_{gw} \equiv |w\rangle\langle g| + |g\rangle\langle w|$. See figure 4.5.

The intensity and frequency perturbations to this Hamiltonian are given by:

$$H_1(t) = \frac{\hbar\Omega_2\epsilon(t)}{2} X_{gw} + \frac{\hbar\nu(t)}{2}(Z_{gw} - |d\rangle\langle d|) \tag{4.42}$$

where $Z_{gw} \equiv |g\rangle\langle g| - |w\rangle\langle w|$. Just as before, $\epsilon(t)$ characterizes the laser intensity fluctuations and $\nu(t)$ characterizes the laser frequency noise. We shall treat motional effects separately in section 4.3. The effect of atomic motion appears as a local independent Doppler shift for each atom as well as a coupling to the dark $|d\rangle$ state.

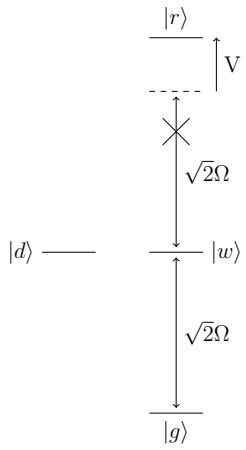

Figure 4.5: Rydberg blockade effect. The blockaded Hamiltonian has an enhanced Rabi frequency $\Omega_2 = \sqrt{2}\Omega$ and the interaction strength V prevents excitation of the $|r\rangle$ state.

Note that the states $|w\rangle$ and $|d\rangle$ are maximally entangled states. Starting from the $|g\rangle$ state, by driving a resonant π-pulse in the blockade regime (pulse duration of π/Ω_2), we can prepare the symmetric maximally entangled state $|w\rangle$. This blockaded π-pulse is thus an entangling gate. Note that while $|d\rangle$ is also maximally entangled, an incoherent mixture (or even any generic coherent mixture) of $|w\rangle$ and $|d\rangle$ is not maximally entangled. Thus we define the two-qubit entanglement fidelity as:

$$\mathcal{F}_2 = \overline{\rho_{ww}(\pi/\Omega_2)} \tag{4.43}$$

If $\mathcal{F}_2 = 1$ then the applied gate resulted in maximal entanglement. If $\mathcal{F}_2 < 1$, then the gate was imperfect and the atoms are not maximally entangled.

Intensity noise (integrable)

For the case of just intensity noise perturbation, the system is integrable just as before and in fact, there is no contribution of the dark state:

$$H_1(t) = \frac{\hbar\Omega_2\epsilon(t)}{2}X_{gw} \tag{4.44}$$

The subspace spanned by $|g\rangle$ and $|w\rangle$ does not mix with the $|d\rangle$ state. This case is identical to the one for a single atom with $\Omega \to \Omega_2$ and $\mathcal{F}_\pi \to \mathcal{F}_2$. Thus we simply refer the reader to Section 4.2.

Frequency noise

For the case of frequency noise perturbation, the system is no longer integrable:

$$H_1(t) = \frac{\hbar\nu(t)}{2}(Z_{gw} - |d\rangle\langle d|) \tag{4.45}$$

While the Hamiltonian explicitly has a term with $|d\rangle\langle d|$, there is no term that couples the $|g\rangle$ state or the $|w\rangle$ state to the $|d\rangle$ state. Thus once again, the subspace spanned by $|g\rangle$ and $|w\rangle$ does not mix with the $|d\rangle$ state. Hence this case is identical to the one for a single atom with $\Omega \to \Omega_2$ and $\mathcal{F}_\pi \to \mathcal{F}_2$. We refer the reader to Section 4.2.

Finite blockade interaction strength

So far we assumed an infinite Rydberg interaction strength and completely eliminated the $|r\rangle = |r_1 r_2\rangle$ state. In the case of a finite but large interaction strength, $V(x_1, x_2) = V \gg \hbar\Omega$, the blockade condition is not perfectly satisfied. However, we can still adiabatically eliminate the $|r\rangle$ state in the dressed state picture. In this section, we ignore any laser noise and consider only the effect of imperfect blockade on the entanglement fidelity. In particular, let us see how the state $|w\rangle$ gets dressed with a slight admixture of $|r\rangle$ in the case of imperfect blockade, resulting in loss of fidelity.

Consider the Hamiltonian H_{wr} for just the states $|w\rangle$ and $|r\rangle$

$$H_{wr} = V\,|r\rangle\langle r| + \frac{\Omega_2}{2}(|w\rangle\langle r| + |r\rangle\langle w|) \tag{4.46}$$

Let $|\boldsymbol{r}\rangle$ and $|\boldsymbol{w}\rangle$ be the eigenstates of H_{wr}. We shall treat the Rabi drive as a perturbation on top of the Rydberg interaction Hamiltonian. Thus $H_0 = V\,|r\rangle\langle r|$ and $H_{pert} = \frac{\Omega_2}{2}(|w\rangle\langle r| + |r\rangle\langle w|)$. We can see that $|w\rangle$ and $|r\rangle$ are eigenstates of H_0 with energies $E_w = 0$ and $E_r = V$. Using standard time-independent pertubation theory to second order, we can calculate the corrections to eigenenergies to be $E_w^{(2)} = -\frac{\hbar^2\Omega^2}{2V}$ and $E_r^{(2)} = \frac{\hbar^2\Omega^2}{2V}$.

Going back to the full Hamiltonian, the Rabi drive between $|g\rangle$ and $|\boldsymbol{w}\rangle$ is no longer resonant because the state $|\boldsymbol{w}\rangle$ has shifted down in energy as a result of the admixture of $|r\rangle$. We can make the drive between $|g\rangle$ and $|\boldsymbol{w}\rangle$ resonant by introducing an appropriate laser detuning. Now starting in the state $|g\rangle\langle g|$, performing a π-pulse with the Rabi drive, we can prepare the state $|\boldsymbol{w}\rangle\langle\boldsymbol{w}|$. However, the entanglement fidelity is not unity since $\langle w|\boldsymbol{w}\rangle \neq 1$. In fact,

$$\langle w|\boldsymbol{w}\rangle \approx 1 - \frac{\hbar^2\Omega^2}{2V^2} \tag{4.47}$$

Thus the entanglement fidelity in the case of imperfect blockade (and no other noies) is given by:

$$\mathcal{F}_2 = |\langle w|\boldsymbol{w}\rangle|^2 \approx 1 - \frac{\hbar^2\Omega^2}{4V^2} \tag{4.48}$$

Motional effects

Here we analyze the effect of a finite momentum distribution on the blockaded Rabi oscillations. The drive Hamiltonian (in the rotating wave approximation) is given by:

$$H = \frac{p_1^2}{2m} + \frac{p_2^2}{2m} + \frac{\hbar\Omega}{2}(e^{-ik_L x_1}\sigma_1^+ + e^{-ik_L x_2}\sigma_2^+ + \text{h.c.}) \tag{4.49}$$

We shall work in the basis $|p_1, p_2, s\rangle$ where $s \in (g, w, d)$ labels the electronic state and p_1 and p_2 represent the atomic momenta.

$$\begin{aligned}
|p_1, p_2, g\rangle &= |(p_1, g_1), (p_2, g_2)\rangle \\
|p_1, p_2, w\rangle &= \frac{1}{\sqrt{2}}(|(p_1 - \hbar k_L, r_1), (p_2, g_2)\rangle \\
&\qquad + |(p_1, g_1), (p_2 - \hbar k_L, g_2)\rangle) \\
|p_1, p_2, d\rangle &= \frac{1}{\sqrt{2}}(|(p_1 - \hbar k_L, r_1), (p_2, g_2)\rangle \\
&\qquad - |(p_1, g_1), (p_2 - \hbar k_L, g_2)\rangle)
\end{aligned}$$

In this basis, the Hamiltonian can be rewritten as follows (up to a constant kinetic energy term):

$$\begin{aligned}
H = \int dp_1 \int dp_2 \; &\Gamma(p_1, p_2) \\
&\times \begin{bmatrix} \frac{\hbar k_L(p_1+p_2)}{2m} & \frac{\hbar\Omega_2}{2} & 0 \\ \frac{\hbar\Omega_2}{2} & 0 & \frac{\hbar k_L(p_2-p_1)}{2m} \\ 0 & \frac{\hbar k_L(p_2-p_1)}{2m} & 0 \end{bmatrix} \Gamma^\dagger(p_1, p_2)
\end{aligned} \tag{4.50}$$

where

$$\Gamma(p_1, p_2) = \begin{pmatrix} |p_1, p_2, g\rangle \\ |p_1, p_2, w\rangle \\ |p_1, p_2, d\rangle \end{pmatrix} \tag{4.51}$$

See Appendix A.3 for derivation.

We see that the Hamiltonian has a Doppler detuning term between $|g\rangle$ and $|w\rangle$ which is sensitive to the global motion of the two atoms, and a Doppler

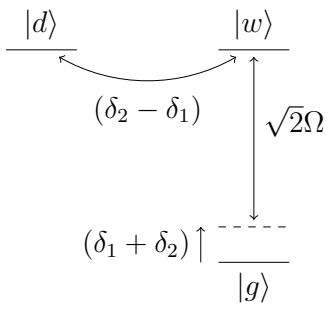

Figure 4.6: Motional effects in the blockade

coupling between $|w\rangle$ and $|d\rangle$ which is sensitive to only the relative motion of the two atoms. We solve this case perturbatively assuming the Doppler shifts are much smaller than the Rabi frequency. Suppressing the momentum degrees of freedom once again, we write the bare Hamiltonian same as before:

$$H_0 = \frac{\hbar\Omega_2}{2} X_{gw} \tag{4.52}$$

and the perturbation Hamiltonian is given by:

$$H_1 = \frac{\hbar\delta_1}{2}(|g\rangle\langle g| - X_{wd}) + \frac{\hbar\delta_2}{2}(|g\rangle\langle g| + X_{wd}) \tag{4.53}$$

where $\delta_j = k_L p_j/m$ and $X_{wd} \equiv |w\rangle\langle d| + |d\rangle\langle w|$. Using the time-evolution operator $U(t)$ (Eq. (4.19)), the ensemble-averaged bright state population $\overline{\rho_{ww}(t)} = \overline{|\langle w|\, U(t)\, |g\rangle\,|^2}$, can be calculated to second order as:

$$\overline{\rho_{ww}(t)} = \left(\frac{1}{2} - \frac{5\overline{\delta^2}}{4\Omega_2^2}\right)(1 - \cos\Omega_2 t) + \frac{\overline{\delta^2} t}{8\Omega_2}\sin\Omega_2 t + O(\delta^4 t^4) \tag{4.54}$$

We can estimate the fidelity of an entangling π-pulse by plugging in $t = \pi/\Omega_2$:

$$\mathcal{F}_2 = 1 - \frac{5\overline{\delta^2}}{4\Omega^2} = 1 - \frac{5k_L^2\overline{p^2}}{4m^2\Omega^2} \tag{4.55}$$

Similarly for the dark state, we find:

$$\overline{\rho_{dd}(t)} = \frac{\overline{\delta^2}}{\Omega_2^2}\left(3 - \cos\Omega_2 t - 4\cos\frac{\Omega_2 t}{2}\right) + O(\delta^4 t^4) \tag{4.56}$$

In Fig. 4.7, we compare our perturbative calculation with exact numerical simulation of the motional effects in the three-level system using Eqs. (4.52, 4.53) and find good agreement between the two at early times. At longer times, we need to go to higher orders in perturbation strength.

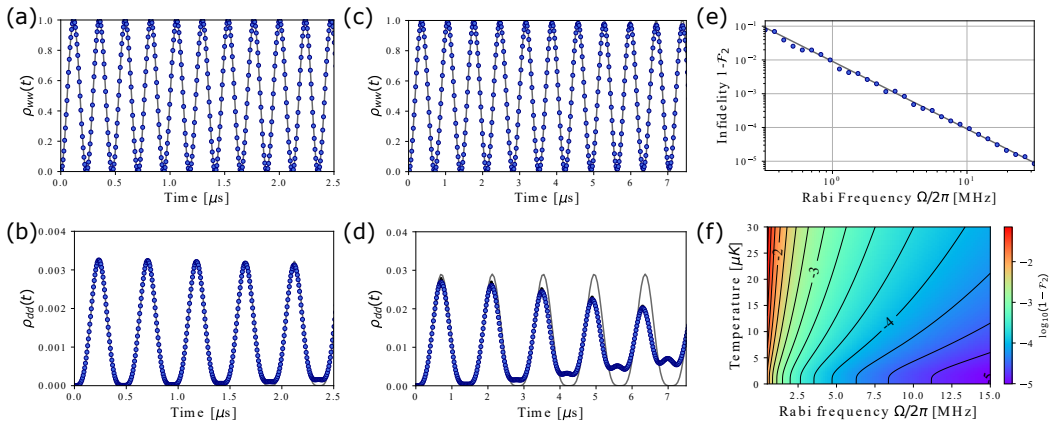

Figure 4.7: Blockaded Rabi oscillations. (a) and (b) Population of $|w\rangle$ and $|d\rangle$ respectively including only motional effects at Rabi frequency $\Omega = 2\pi \times 3$ MHz, trap frequency $\omega = 2\pi \times 80$ kHz and temperature $T = 15\ \mu K$ (to exaggerate the decoherence). The blue dots are generated using numerical simulation, the gray curve is the perturbation theory result Eq. (4.54, 4.56). We see good agreement between the theory and numerics at early times. (c) and (d) Same as (a) and (b) respectively except with $\Omega = 2\pi \times 1$ MHz. The decoherence is faster at this lower Rabi frequency. (e) Infidelity of an entangling π-pulse (1 - $\mathcal{F}_2$) at same trapping frequency and temperature. The blue dots are generated using numerical simulation and the gray curve is from Eq. (4.55). (f) 2D color plot of the entangling π-pulse infidelity (1 - $\mathcal{F}_2$). Considering only motional effects, the fidelity increases with Rabi frequency and decreases with temperature.

Combined effect

Considering the effect of all the different noise sources, namely, intensity noise, frequency noise, finite blockade strength and atomic motion, we get a combined two-atom entanglement fidelity of

$$\mathcal{F}_2 = 1 - \frac{5}{4}\frac{\overline{\delta^2}}{\Omega^2} - \frac{\hbar^2\Omega^2}{4V^2} - \frac{\pi^2}{2}\int \frac{d\omega}{2\pi} S_\epsilon(\omega) W_0(\omega, \frac{\pi}{\sqrt{2}\Omega}) - \frac{\pi^2}{16\Omega^2}\int \frac{d\omega}{2\pi} S_\nu(\omega) W_1(\omega, \sqrt{2}\Omega, \frac{\pi}{\sqrt{2}\Omega}) \quad (4.57)$$

See Fig. 4.8 for a comparison to numerics. In addition, we also compare this result to the recent experimental work from our group [17]. We find that our entanglement fidelity predicted using independent measurements of noise parameters is consistent with our experimental data point at the 1σ level. We estimate the contribution to the infidelity from spontaneous emission using the integrated Rydberg state population and find it is $\approx 10^{-3}$. Thus our predicted fidelity is still consistent with the experimental data point. Thus

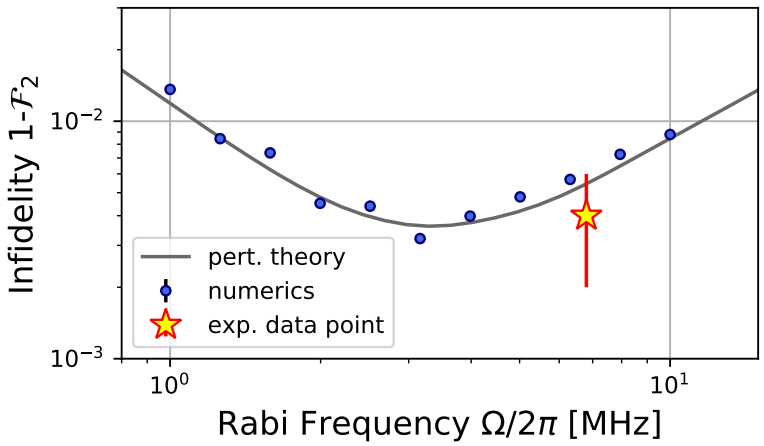

Figure 4.8: Infidelity of a two-qubit entangling π-pulse (1 - $\mathcal{F}_2$) considering the effects of intensity noise, frequency noise, finite blockade strength and temperature. We use an interaction strength of $V = h \times 130$ MHz as in our experimental setup [17]. The blue dots are generated using numerical simulation and the gray curve is from Eq. (4.57). In addition, the star marker represents the (SPAM corrected) experimentally achieved two-atom entanglement fidelity reported in [17]. We see good agreement between numerics and our perturbative result. Our predicted fidelity is consistent with our experimental data point at the 1σ level. This implies that the noise sources we have considered are the dominant ones in our experiment. At low Rabi frequency, the limiting factor is frequency noise whereas at high Rabi frequency, the limiting factor is intensity noise.

our noise modelling is accurate enough to predict experimentally achievable entanglement fidelities.

4.4 Conclusion

We have analyzed some of the dominant noise sources present in Rabi oscillations of Rydberg atoms. For both the non-interacting case and the Rydberg blockaded case, we provided analytical expressions for the effect of atomic motion, intensity noise and frequency noise with an arbitrary PSD. We also considered the case of imperfect blockade. We presented our results in terms of window functions acting on the noise PSDs which give us qualitative as well as quantitative understanding of the effect of the various frequency components of the noise. We compared our analytical results with exact numerical simulations and saw good agreement. Additionally, we compared our predicted π-pulse fidelity and entanglement fidelity to the actual experimentally observed fidelities and found that our prediction is consistent with what we

observe. Thus our modelling helps us predict the experimentally achievable fidelities and helps us understand how the various noise sources contribute to the decoherence of Rabi oscillations.

Chapter 5

RABI OSCILLATIONS OF ATOMS IN A TRAP

5.1 Motivation

So far when studying the Rabi oscillations of atoms we have only considered the electronic degrees of freedom of the atoms and ignored their translational degrees of freedom. In this chapter, we shall study how the (quantized) motion of the atoms affects Rabi oscillations. There are two ways in which the motion of the atom comes into play. Firstly, when the atoms absorb a photon, they also experience a momentum kick from the momentum of the photon. Secondly, while typical experiments with Rydberg atoms are conducted with the optical tweezers turned off, we can also conduct these experiments with the confining potentially left on. This means that the momentum and position the atom can affect how they behave when driven by a laser.

At the start of a quench experiment, the atoms are held in optical tweezers using the optical polarizability of the atoms. The tightly focused gaussian trapping beams of light give rise to an approximately harmonic trapping potential at the focus. See Appendix C for details of the full trapping potential. Here, we shall work in 1D and treat the potential to be harmonic. If we fine-tune the wavelength of the trapping light, we can ensure that the optical polarizability of the ground state $|g\rangle$ and excited state $|e\rangle$ is identical. This is known as a 'magic' trapping condition [51]. However, in general the polarizabilities of the two states are unequal. In fact, when the excited state is a Rydberg state, it is generically not even trapped by the optical tweezer (magic trapping of Rydberg states with optical tweezers was only recently demonstrated in Yb atoms [52]). We (Endres group) recently experimentally demonstrated high fidelity Rydberg Rabi oscillations in the presence of the non-magic potential of optical tweezers [17]. For the large Rabi frequency that we were able to achieve, the presence of the optical potential did not seem to have any appreciable effect on the Rabi oscillation fidelity. Futher, we were able to demonstrate high-fidelity Rydberg blockaded oscillations in the presence of the traps as well. Thus we are interested in understanding Rabi oscillations in the generic non-magic trapping condition.

5.2 Hamiltonian

The case of Rabi oscillations with a harmonic trapping potential in the case where the trap frequency is much larger than the Rabi frequency has been well studied in literature [53]. Here, the Hamiltonian is analyzed using basis states which are electronic states tensored with the fock basis of the harmonic oscillator. However, for high-fidelity Rydberg atom Rabi oscillations, we are interested in the case where the Rabi frequency is much larger than the trap frequency. In this case, the usual basis is not convenient to work in, as we shall see. Instead, we define a new basis of a displaced harmonic oscillator in which all the operators in the Hamiltonian are nearly diagonal.

The full single particle Hamiltonian is given by:

$$\begin{aligned} H = &\frac{p^2}{2m} \otimes \mathbb{1} \\ &+ \frac{1}{2} m x^2 \left(\omega_g^2 \left| g \right\rangle\!\left\langle g \right| + \omega_e^2 \left| e \right\rangle\!\left\langle e \right| \right) \\ &+ \frac{\hbar \Omega}{2} \left(e^{ikx} \left| e \right\rangle\!\left\langle g \right| + e^{-ikx} \left| g \right\rangle\!\left\langle e \right| \right) - \hbar \Delta \left| e \right\rangle\!\left\langle e \right| \end{aligned} \tag{5.1}$$

We shall rewrite this Hamiltonian in a more convenient form as follows. We introduce a fictitious trapping frequency ω. Using this frequency as a reference, we define the relative polarizability of the ground electronic state to be $\alpha_g = \omega_g^2/\omega^2$. We define the relative polarizability of the excited state α_e similarly. Note that for the magic condition $\alpha_e = \alpha_g$, for the general non-magic condition $\alpha_e \neq \alpha_g$, and for the case when the trapping potential is turned off altogether, $\alpha_e = \alpha_g = 0$. Using these variables, we get the following Hamiltonian:

$$\begin{aligned} H = &\left(\frac{p^2}{2m} + \frac{1}{2} m \omega^2 x^2 \right) \otimes \mathbb{1} \\ &+ \frac{\hbar \Omega}{2} \left(e^{ikx} \left| e \right\rangle\!\left\langle g \right| + e^{-ikx} \left| g \right\rangle\!\left\langle e \right| \right) - \hbar \Delta \left| e \right\rangle\!\left\langle e \right| \\ &+ \frac{1}{2} m \omega^2 x^2 \left((\alpha_g - 1) \left| g \right\rangle\!\left\langle g \right| + (\alpha_e - 1) \left| e \right\rangle\!\left\langle e \right| \right) \end{aligned} \tag{5.2}$$

Now we can expand the continuous position variables using the ladder operators defined by the harmonic oscillator with trapping frequency ω. That is, we define x and p as:

$$\begin{aligned} x &= x_0 (a + a^\dagger) \\ p &= p_0 (i a^\dagger - i a) \end{aligned} \tag{5.3}$$

where $x_0 = \sqrt{\frac{\hbar}{2m\omega}}$ is the length scale of the harmonic oscillator and $p_0 = \sqrt{\frac{\hbar m\omega}{2}} = \frac{\hbar}{2x_0}$ is the momentum scale. Let η be the Lamb-Dicke parameter i.e. $\eta = kx_0 = \frac{2\pi x_0}{\lambda_L}$ where λ_L is the wavelength of the driving laser. This parameter indicates how delocalized the atomic wavefunction is compared to the laser wavelength. If $\eta \ll 1$, the atom is tightly confined. And if $\eta \approx 1$, the atomic spread is comparable to the wavelength. Given the commutation relation $[x, p] = i\hbar$, we have $[a, a^\dagger] = 1$. Also $a\,|n\rangle = \sqrt{n}\,|n-1\rangle$ and $a^\dagger\,|n\rangle = \sqrt{n+1}\,|n+1\rangle$. In this basis the Hamiltonian is given by:

$$\begin{aligned} H = {} & \hbar\omega\left(a^\dagger a + \frac{1}{2}\right)\otimes \mathbb{1} \\ & + \frac{\hbar\Omega}{2}\left(e^{i\eta(a+a^\dagger)}\,|e\rangle\langle g| + e^{-i\eta(a+a^\dagger)}\,|g\rangle\langle e|\right) - \hbar\Delta\,|e\rangle\langle e| \\ & + \frac{\hbar\omega}{4}(a+a^\dagger)^2\left((\alpha_g - 1)\,|g\rangle\langle g| + (\alpha_e - 1)\,|e\rangle\langle e|\right) \end{aligned} \tag{5.4}$$

Now we shall see why the usual fock basis is a good basis for the case where $\Omega \ll \omega$ and why it is not convenient when $\omega \ll \Omega$. Assume for now that the detuning Δ is zero (resonant) or negligible compared to other energy scales in the Hamiltonian. Note that the term $a^\dagger a$ is diagonal in the fock basis, i.e. it does not change the harmonic oscillator occupation number ($\langle n'|\,a^\dagger a\,|n\rangle \propto \delta_{n',n}$). The term $(a + a^\dagger)^2$ changes the occupation number by at most 2 levels. However, the term $e^{i\eta(a+a^\dagger)}$ could change the occupation number by an arbitrary number (see Figure 5.1). We can see this by Taylor expanding the operator using η as the expansion parameter. The explicit form of the operator $e^{i\eta(a+a^\dagger)}$ in the fock basis can be expressed in terms of a generalized Laguerre polynomial [53]. The coefficient of the $e^{i\eta(a+a^\dagger)}$ is the Rabi frequency $\sim \Omega$. In the case

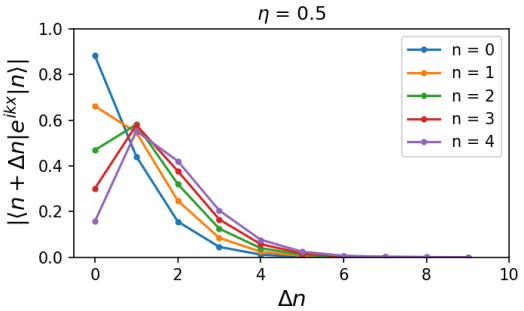

Figure 5.1: Magnitude of the matrix elements of the operator e^{ikx} in the fock basis. We work with Lamb-Dicke parameter $\eta = 0.5$. Notice that the matrix elements have a significant non-zero magnitude for a large number of fock states $|n + \Delta n\rangle$ starting from the state $|n\rangle$.

where $\Omega \ll \omega$, the transitions where the oscillator occupation number changes by more than one are strongly suppressed by a factor of $\sim \Omega/\omega$. Thus even though the operator $e^{i\eta(a+a^\dagger)}$ connects several different states, most of those transitions are energetically suppressed. However, when $\omega \ll \Omega$, the transitions in oscillator occupation number caused by the operator $e^{i\eta(a+a^\dagger)}$ are no longer energetically suppressed. Thus a single n in the ground electronic state can be driven to many different n' in the excited electronic state. Thus we need to define a new basis in which the operator $e^{i\eta(a+a^\dagger)}$ connects only a few different states (ideally only 2).

5.3 Strong resonant drive

Here we work in the limit $\omega_g/\Omega \ll 1$. We do not make assumptions about the magnitude of the Lamb-Dicke parameter η. We shall set $\omega = \omega_g$. Let $\xi = e^{i\eta(a+a^\dagger)}$ and $\xi^\dagger = e^{-i\eta(a+a^\dagger)}$. Let $H = H_0 + H_1$ where

$$\begin{aligned} H_0 &= \frac{\hbar\Omega}{2}\left(\xi\left|e\right\rangle\!\left\langle g\right| + \xi^\dagger\left|g\right\rangle\!\left\langle e\right|\right) - \hbar\Delta\left|e\right\rangle\!\left\langle e\right| + \hbar\omega_g\left(a^\dagger a + \frac{1}{2}\right)\otimes\mathbb{1} \\ H_1 &= \frac{\hbar\omega_g}{4}(\alpha_e - 1)(a + a^\dagger)^2\left|e\right\rangle\!\left\langle e\right| \end{aligned} \tag{5.5}$$

We shall use $|g,n\rangle = |g\rangle \otimes |n\rangle$ and $|e,\xi(n)\rangle = |e\rangle \otimes e^{i\eta(a+a^\dagger)}|n\rangle$ as basis states. Note that $\langle e,\xi(n)| = \langle e| \otimes \langle n|\, e^{-i\eta(a+a^\dagger)}$. Inserting resolutions of the identity to the left and right of the Hamiltonian, we can write the Hamiltonian as:

$$H = \left(\sum_{n'} |g,n'\rangle\!\langle g,n'| + |e,\xi(n')\rangle\!\langle e,\xi(n')|\right) H \left(\sum_{n} |g,n\rangle\!\langle g,n| + |e,\xi(n)\rangle\!\langle e,\xi(n)|\right) \tag{5.6}$$

Now for convenience we define the the spinors Γ_n and $\Gamma_n^\dagger$ as:

$$\begin{aligned} \Gamma_n^\dagger &= \begin{pmatrix} |g,n\rangle & |e,\xi(n)\rangle \end{pmatrix} \\ \Gamma_n &= \begin{pmatrix} \langle g,n| \\ \langle e,\xi(n)| \end{pmatrix} \end{aligned} \tag{5.7}$$

Then we can rewrite H as:

$$H = \left(\sum_{n'} \Gamma_{n'}^\dagger \Gamma_{n'}\right) H \left(\sum_{n} \Gamma_n^\dagger \Gamma_n\right) = \sum_{n,n'} \Gamma_{n'}^\dagger \left(\Gamma_{n'} H \Gamma_n^\dagger\right) \Gamma_n \tag{5.8}$$

where $\left(\Gamma_{n'} H \Gamma_n^\dagger\right)$ is a 2×2 matrix given by:

$$h_{n',n} = \left(\Gamma_{n'} H \Gamma_n^\dagger\right) = \begin{bmatrix} \langle g,n'|\, H\, |g,n\rangle & \langle g,n'|\, H\, |e,\xi(n)\rangle \\ \langle e,\xi(n')|\, H\, |g,n\rangle & \langle e,\xi(n')|\, H\, |e,\xi(n)\rangle \end{bmatrix} \tag{5.9}$$

Note that since x commutes with ξ, we can compute many matrix elements just as in the standard fock basis. For the momentum operator, we use the Baker-Campbell-Hausdorff (BCH) formula to compute matrix elements. A particular version of the formula is given by:

$$e^X Y e^{-X} = Y + [X,Y] + \frac{1}{2}[X,[X,Y]] + \frac{1}{6}[X,[X,[X,Y]]] + ... \tag{5.10}$$

Applying BCH to $X = -i\eta(a + a^\dagger) = -ikx$ gives us:

Y	$[X,Y]$	$\frac{1}{2}[X,[X,Y]]$	$\frac{1}{6}[X,[X,[X,Y]]]$
$(a+a^\dagger)^n$	0	0	0
$a^\dagger a$	$i\eta(a^\dagger - a)$	η^2	0
a^2	$2i\eta a$	$-\eta^2$	0
$(a^\dagger)^2$	$-2i\eta a^\dagger$	$-\eta^2$	0

Now we can compute all the non-zero matrix elements:

$$\begin{aligned}
\langle g,n'|\, H_0\, |g,n\rangle &= \hbar\omega_g \left(n + \frac{1}{2}\right)\delta_{n',n} \\
\langle g,n'|\, H_0\, |e,\xi(n)\rangle &= \hbar\Omega/2\delta_{n',n} \\
\langle e,\xi(n')|\, H_0\, |g,n\rangle &= \hbar\Omega/2\delta_{n',n} \\
\langle e,\xi(n')|\, H_0\, |e,\xi(n)\rangle &= \hbar\omega_g \left(n + \frac{1}{2} + \eta^2\right)\delta_{n',n} - \hbar\Delta\delta_{n',n} \\
&\quad + i\eta\hbar\omega_g \left(\sqrt{n+1}\delta_{n',n+1} - \sqrt{n}\delta_{n',n-1}\right) \\
\langle e,\xi(n')|\, H_1\, |e,\xi(n)\rangle &= \frac{\hbar\omega_g(\alpha_e - 1)}{4}\Big[(1+2n)\delta_{n',n} \\
&\quad + \left(\delta_{n',n-2}\sqrt{n(n-1)} + \delta_{n',n+2}\sqrt{(n+1)(n+2)}\right)\Big]
\end{aligned} \tag{5.11}$$

Let $h_{n',n} = \left(\Gamma_{n'} H_0 \Gamma_n^\dagger\right)$ corresponding to the magic trapping part of the Hamiltonian and $h'_{n',n} = \left(\Gamma_{n'} H_1 \Gamma_n^\dagger\right)$ correspond to the non-magic terms. Then we

can write the Hamiltonian as:

$$
\begin{aligned}
h_{n,n} &= n\hbar\omega_g \mathbb{1} + \frac{\hbar\Omega}{2}\sigma^x + \hbar(\omega_g\eta^2 - \Delta)\left(\frac{\mathbb{1}-\sigma^z}{2}\right) \\
h_{n+1,n} &= +i\eta\hbar\omega_g\sqrt{n+1}\left(\frac{\mathbb{1}-\sigma^z}{2}\right) \\
h_{n,n+1} &= -i\eta\hbar\omega_g\sqrt{n+1}\left(\frac{\mathbb{1}-\sigma^z}{2}\right)
\end{aligned} \tag{5.12}
$$

$$
\begin{aligned}
h'_{n,n} &= \frac{\hbar\omega_g(\alpha_e-1)}{4}(2n+1)\left(\frac{\mathbb{1}-\sigma^z}{2}\right) \\
h'_{n+2,n} &= \frac{\hbar\omega_g(\alpha_e-1)}{4}\sqrt{(n+1)(n+2)}\left(\frac{\mathbb{1}-\sigma^z}{2}\right) \\
h'_{n,n+2} &= -\frac{\hbar\omega_g(\alpha_e-1)}{4}\sqrt{(n+1)(n+2)}\left(\frac{\mathbb{1}-\sigma^z}{2}\right)
\end{aligned} \tag{5.13}
$$

See Figure 5.2 for a visualization of the different terms in the Hamiltonian. For magic trapping, we can choose the laser detuning Δ such that it cancels the doppler shift term $\omega_g\eta^2 = \hbar k^2/2m$. For the non-magic trapping case, we cannot make all fock levels resonant. However, for low temperatures, we are mostly interested in the lowest fock level. Thus we choose the laser detuning that makes the $|g,0\rangle \leftrightarrow |e,\xi(0)\rangle$ transition resonant, i.e. $\Delta = \omega_g\eta^2 + \omega_g(\alpha_e - 1)/4$.

Strong resonant drive with magic trapping

In this case, all $h'_{n',n}$ terms are zero. The Hamiltonian has a chemical potential for each site, an on-site flip-flop term, and a nearest-neighbour spin-selective hopping term. In the strong drive regime, we can treat the hopping term perturbatively. Let us perform another change of basis. We shall work in the $|\pm n\rangle$ basis defined by:

$$
|\pm n\rangle = \frac{|g,n\rangle \pm |e,\xi(n)\rangle}{\sqrt{2}} \tag{5.14}
$$

For the 'resonant' case, there is no σ^z term in $h_{n,n}$. Thus $|\pm n\rangle$ are eigenstates of the bare Hamiltonian with bare energy $E^{(0)}_{\pm n} = n\hbar\omega_g \pm \hbar\Omega/2$.

Perturbative energy shifts and corrections to the eigenstates

The first order shift to the energy vanishes since the perturbing terms are off-diagonal. We get a second order contribution to energy. We are most interested in the low n eigenstates since these are the ones we deal with at

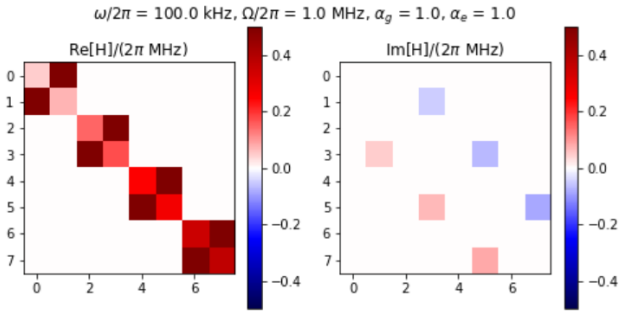

(a) Magic Trapping condition

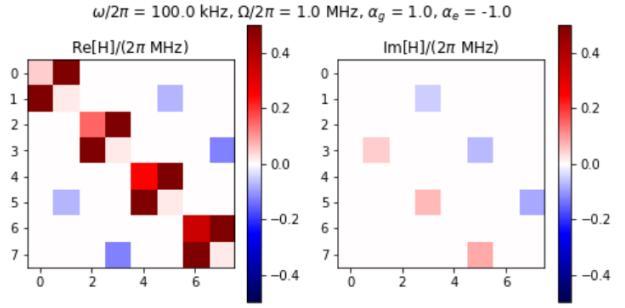

(b) Non-Magic Trapping condition

Figure 5.2: Visualizing the Hamiltonian in the modified basis in matrix form with a truncated Hilbert space of 4 harmonic oscillator energy levels. For the magic trapping case, we can see that the Hamiltonian is almost block diagonal with block size of 2. In the non-magic trapping case, the Hamiltonian has matrix elements that change the occupation number n by up to 2. Thus in both cases, this modified basis is quite convenient.

low temperature of the atoms. We calculate the perturbative corrections to the $n = 0$ eigenstates and eigenenergies in table 5.1. We define $y = \omega/\Omega$ and use the notation: $|\Psi\rangle$ is the unperturbed eigenstate, $\left|\psi^{(1)}\right\rangle$ is the first order correction to state, $E_\psi^{(2)}$ is the second order correction to the energy of the state and $|\boldsymbol{\psi}\rangle = |\psi\rangle + \left|\psi^{(1)}\right\rangle + ...$ is un-normalized perturbed eigenstate.

$$\begin{aligned} H_{pert}\,|\psi\rangle &= \sum_j c_j\,|\phi_j\rangle \\ \left|\psi^{(1)}\right\rangle &= \sum_j \frac{c_j}{E_\psi - E_{\phi_j}} \\ E_\psi^{(2)} &= \sum_j \frac{|c_j|^2}{E_\psi - E_{\phi_j}} \end{aligned} \tag{5.15}$$

Note that for moderate values of η, there is significant mixing of eigenstates by the perturbing Hamiltonian (regardless of how large Ω is). We can also

$\|\psi\rangle$	E_ψ	$\|\phi_j\rangle$	c_j	$E_\psi - E_{\phi_j}$	$\|\psi^{(1)}\rangle$	$E_\psi^{(2)}$	$\langle\boldsymbol{\psi}\|\boldsymbol{\psi}\rangle - 1$
$\|+0\rangle$	$\hbar\Omega/2$	$\|+1\rangle$	$\frac{i\eta}{2}\hbar\omega_g$	$-\hbar\omega_g$	$-\frac{i\eta}{2}\|+1\rangle$	$-\frac{\eta^2}{4}\hbar\omega_g$	$\frac{\eta^2}{4}$
		$\|-1\rangle$	$-\frac{i\eta}{2}\hbar\omega_g$	$\hbar\Omega - \hbar\omega_g$	$-\frac{i\eta}{2}\frac{y}{1-y}\|-1\rangle$	$\frac{\eta^2}{4}\frac{y}{1-y}\hbar\omega_g$	$\frac{\eta^2}{4}\frac{y^2}{(1-y)^2}$
$\|-0\rangle$	$-\hbar\Omega/2$	$\|+1\rangle$	$-\frac{i\eta}{2}\hbar\omega_g$	$-\hbar\Omega - \hbar\omega_g$	$\frac{i\eta}{2}\frac{y}{1+y}\|+1\rangle$	$-\frac{\eta^2}{4}\frac{y}{1+y}\hbar\omega_g$	$\frac{\eta^2}{4}\frac{y^2}{(1+y)^2}$
		$\|-1\rangle$	$\frac{i\eta}{2}\hbar\omega_g$	$-\hbar\omega_g$	$-\frac{i\eta}{2}\|-1\rangle$	$-\frac{\eta^2}{4}\hbar\omega_g$	$\frac{\eta^2}{4}$

Table 5.1: Perturbative correction to the $n = 0$ eigenstates and eigenenergies for magic trapping

compute these energy shifts and overlaps for all other $|\pm n\rangle$ for $n \geq 1$.

Numerics

We perform numerical simulation of time evolution for the case of magic trapping. We start in a thermal initial state in the ground electronic manifold. Specifically, we mean that the initial density matrix is given by $\rho_0 = \rho_\beta^{HO} \otimes |g\rangle\langle g|$ where ρ_β^{HO} is the reduced density matrix of the harmonic oscillator at inverse temperature $\beta = 1/T$. In other words, the reduced density matrix of the harmonic oscillator is diagonal and the population in the state labelled by n is given by its Boltzmann factor $e^{-\beta E_n}/Z$ where Z is the partition function. We use a truncated Hilbert space, restricting to $N = 100$ harmonic oscillator energy levels. The resultant two atom Hilbert space has dimension $2N = 200$. We do not see any finite size effects as a result of this truncation. We use parameters of $\omega/2\pi = 100$ kHz, $\omega/2\pi = 1$ MHz, $\eta = 0.5$ and $T = 2.5\mu K$ as a test case (see Figure 5.3). We find that the resultant Rabi oscillations have high contrast. In addition, the population remains well confined to the motional ground state of the harmonic oscillator even though $\Omega \gg \omega$. The average occupation number of the harmonic oscillator remains small (< 0.5) and the spread of the atomic wavefunction in position space is small.

Strong drive with non-magic trapping

This is case relevant to Rydberg Rabi oscillations with anti-trapped Rydberg states. Here we still have $\omega = \omega_g \ll \Omega$. However, $\alpha_e \neq \alpha_g$. In this case the $h'_{n,n}$, $h'_{n,n+2}$ and $h'_{n+2,n}$ terms are non-zero but still perturbative since $\omega \ll \Omega$ and $|\alpha_e| \sim 1$. We choose $\Delta = \omega_g\eta^2 + \omega_g(\alpha_e - 1)/4$ to make the lowest motional level resonant. Thus we can again change basis to the $|\pm n\rangle$ basis which are eigenstates of the bare Hamiltonian. We calculate perturbative corrections to

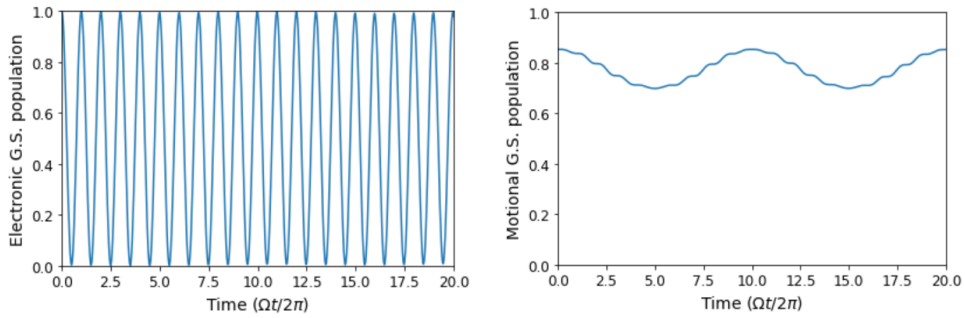

(a) Electronic ground state population P_g (b) Motional ground state population

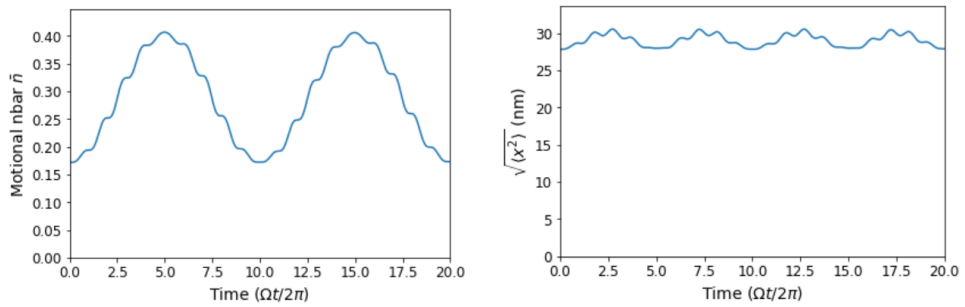

(c) Average motional occupation number $\bar{n}$ (d) Standard Deviation of atomic position $\sqrt{\langle x^2 \rangle}$

Figure 5.3: Numerical simulation of time evolution of a thermal initial state for the case of magic trapping. See text for details.

these states and their energies.

Perturbative energy shifts and corrections to the eigenstates

The first order shift to the energy no longer vanish for all n since the perturbing terms not all off-diagonal. However, for $n = 0$, the $h'_{n,n}$ term is zero and thus the first order shift is also zero. We calculate the second order correction to energy and the first-order correction to the $n = 0$ state in table 5.2. Again let $y = \omega/\Omega$ and define c_j, $|\phi_j\rangle$, $|\psi^{(1)}\rangle$, $E^{(2)}_{\psi}$ and $|\boldsymbol{\psi}\rangle$ same as in equation (5.15).

We see that the more non-magic the trapping is, i.e., the further α_e is from 1, the more the eigenstates get mixed together. Note that for moderate values of η, there is significant mixing of eigenstates by the perturbing Hamiltonian (regardless of how large Ω is). We can also compute these energy shifts and overlaps for all other $|\pm n\rangle$ for $n \geq 1$.

$\|\psi\rangle$	E_ψ	$\|\phi_j\rangle$	$\|\psi^{(1)}\rangle$	$E_\psi^{(2)}$	$\langle\boldsymbol{\psi}\|\boldsymbol{\psi}\rangle - 1$
$\|+0\rangle$	$\hbar\Omega/2$	$\|+1\rangle$	$-\frac{i\eta}{2}\|+1\rangle$	$-\frac{\eta^2}{4}\hbar\omega_g$	$\frac{\eta^2}{4}$
		$\|-1\rangle$	$-\frac{i\eta}{2}\frac{y}{1-y}\|-1\rangle$	$\frac{\eta^2}{4}\frac{y}{1-y}\hbar\omega_g$	$\frac{\eta^2}{4}\frac{y^2}{(1-y)^2}$
		$\|+2\rangle$	$-\frac{(\alpha_e-1)\sqrt{2}}{16}\|+2\rangle$	$-\frac{(\alpha_e-1)^2}{64}\hbar\omega_g$	$\frac{(\alpha_e-1)^2}{128}$
		$\|-2\rangle$	$-\frac{(\alpha_e-1)\sqrt{2}}{8}\frac{y}{1-2y}\|-2\rangle$	$\frac{(\alpha_e-1)^2}{32}\frac{y}{1-2y}\hbar\omega_g$	$\frac{(\alpha_e-1)^2}{32}\frac{y^2}{(1-2y)^2}$
$\|-0\rangle$	$-\hbar\Omega/2$	$\|+1\rangle$	$\frac{i\eta}{2}\frac{y}{1+y}\|+1\rangle$	$-\frac{\eta^2}{4}\frac{y}{1+y}\hbar\omega_g$	$\frac{\eta^2}{4}\frac{y^2}{(1+y)^2}$
		$\|-1\rangle$	$-\frac{i\eta}{2}\|-1\rangle$	$-\frac{\eta^2}{4}\hbar\omega_g$	$\frac{\eta^2}{4}$
		$\|+2\rangle$	$\frac{(\alpha_e-1)\sqrt{2}}{8}\frac{y}{1+2y}\|+2\rangle$	$-\frac{(\alpha_e-1)^2}{32}\frac{y}{1+2y}\hbar\omega_g$	$\frac{(\alpha_e-1)^2}{32}\frac{y^2}{(1+2y)^2}$
		$\|-2\rangle$	$-\frac{(\alpha_e-1)\sqrt{2}}{16}\|-2\rangle$	$-\frac{(\alpha_e-1)^2}{64}\hbar\omega_g$	$\frac{(\alpha_e-1)^2}{128}$

Table 5.2: Perturbative correction to the $n = 0$ eigenstates and eigenenergies for non-magic trapping

Numerics

Now we numerical simulate time evolution for the case of non-magic trapping. Again, we start in a thermal initial state in the ground electronic manifold. We use parameters of $\omega/2\pi = 100$ kHz, $\omega/2\pi = 1$ MHz, $\eta = 0.5$ and $T = 2.5\mu K$. In addition, we set $\alpha_e = -1$, i.e. the excited state is just as anti-trapped as the ground state is trapped. We use a truncated Hilbert space, restricting to $N = 100$ harmonic oscillator energy levels. The resultant two atom Hilbert space has dimension $2N = 200$. We do not see any finite size effects as a result of this truncation. See Figure 5.4.

We find that the resultant Rabi oscillations initially have a large contrast but rapidly start to lose contrast. After a few cycles, the oscillations show a revival which is typical of thermal decoherence of Rabi oscillations. This occurs when the different motional levels oscillate at slightly different Rabi frequencies and periodically constructively and destructively interfere. The population is no longer well confined to the motional ground state of the harmonic oscillator. However, the population in the motional ground state does not keep decreasing monotonically - the population asymptotes to about 0.5 after about 5 Rabi cycles. The average occupation number of the harmonic oscillator rapidly increases at short times but does not keep increasing unbounded. It seems to peak at about 5 cycles and then reduces again. The spread of the atomic wavefunction in position space mimics the behavior of the motional occupation

number.

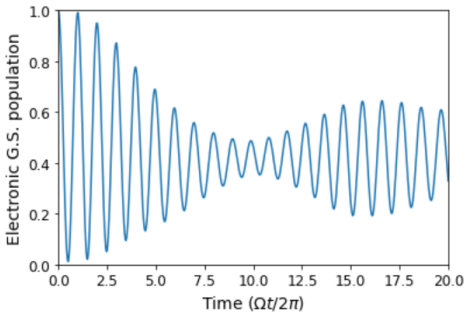

(a) Electronic ground state population P_g

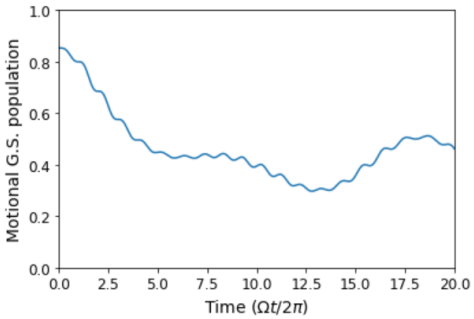

(b) Motional ground state population

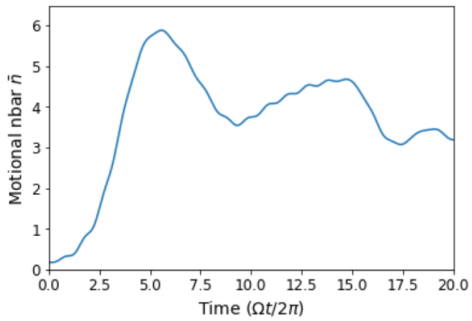

(c) Average motional occupation number $\bar{n}$

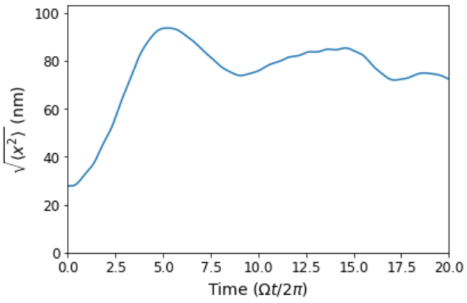

(d) Standard Deviation of atomic position $\sqrt{\langle x^2 \rangle}$

Figure 5.4: Numerical simulation of time evolution of a thermal initial state for the case of non-magic trapping. See text for details.

It appears that the fidelity of Rabi oscillations is severely impacted by the non-magic condition. However, in real experiments, we take measures to mitigate this effect. The trap depth of the optical tweezers is adiabatically reduced by several fold ($\sim$ 10 times reduction) before the start of the Rabi drive. This adiabatic ramp-down not only reduces the temperature of the atoms (thus reducing the momentum-spread) but also reduced the ratio of ω/Ω. Thus the non-magic effects and reduced by several fold when we ramp down the tweezer depth. We numerically simulate this ramp-down effect for many different values of Ω and ω keeping the initial temperature constant at $T = 2.5\mu K$. From the resultant Rabi oscillations, we extract the pi-pulse fidelity F_π and two-pi-pulse fidelity $F_{2\pi}$. These we define as $F_\pi = \langle e| \rho(t = \pi/\Omega) |e\rangle$ and $F_\pi = \langle g| \rho(t = 2\pi/\Omega) |g\rangle$. See Figure 5.5 for a parametric plot of the pi-pulse and two-pi-pulse infidelities $(1 - F)$. We see that increasing Rabi frequency Ω and decreasing the trap frequency ω lead to higher fidelities. Further, even

for the anti-trapping condition, the fidelities achievable are quite high (at the 0.9999 level ignoring all other decoherence).

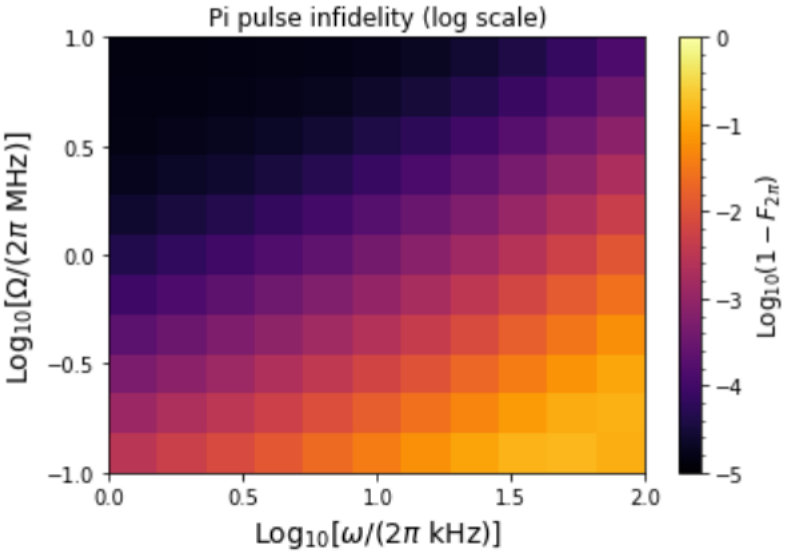

(a) Pi-pulse Infidelity $1 - F_{\pi}$

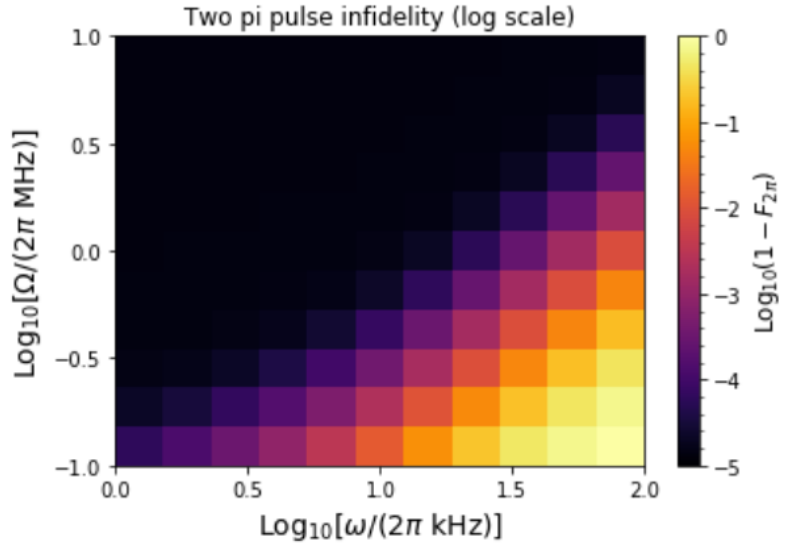

(b) Two-Pi-pulse Infidelity $1 - F_{2\pi}$

Figure 5.5: Rabi oscillation fidelities extracted from numerical simulation for a single atom in a non-magic condition. See text for details.

5.4 Rydberg interactions

The interaction between two atoms in the rydberg state is given by the van der Waals potential.

$$H_{int} = \frac{C_6}{|\vec{r}_1 - \vec{r}_2|^6} |ee\rangle\langle ee| \tag{5.16}$$

where C_6 is the van der Waals interaction coefficient that depends on the atomic species as well as the principal quantum number. Let a_0 be the mean separation between the two atoms. In the Rydberg blockade regime, $C_6/a_0^6 \gg \Omega$, the energy penalty of having two atoms in the Rydberg state is much larger than the Rabi drive frequency. Thus the strong dipole-dipole interactions prevent more than one Rydberg excitation for atoms within the blockade radius $R_c \approx (C_6/\Omega)^{1/6}$. By driving Rabi oscillations in the blockaded regime, the two atoms get entangled and form a symmetric Bell state [54]. The blockaded Hamiltonian couples the electronic state $|G\rangle = |gg\rangle$ to the maximally entangled state $|W\rangle = \frac{1}{\sqrt{2}}(|eg\rangle + |ge\rangle)$. We wish to study how entanglement with motional degrees of freedom impacts the two-atom entanglement fidelity.

The position operators in the denominator of the interaction term are troublesome to deal with as they appear. However, we can Taylor expand the denominator about the mean separation a_0 to bring the operators to the numerator.

$$\begin{aligned}\frac{C_6}{|\vec{r}_1 - \vec{r}_2|^6} &= C_6 \left(\frac{1}{a_0^6} - \frac{6(x_1 - x_2)}{a_0^7} + \frac{21(x_1 - x_2)^2}{a_0^8} - \frac{3(y_1 - y_2)^2}{a_0^8} - \frac{3(z_1 - z_2)^2}{a_0^8} + ... \right) \\ &\approx V - \frac{6V(x_1 - x_2)}{a_0} + O((\delta r)^2)\end{aligned} \tag{5.17}$$

where we have defined $V = C_6/a_0^6$. We see that to first order in position fluctuations, the interaction potential only depends on the separation along the x-direction. Even including second order effects, the x, y and z directions remain separable. Thus we can continue to work in 1D. Further, since $\xi = e^{ikx}$ commutes with x, the matrix elements of the interaction Hamitonian in the modified fock basis are identical to those in the usual fock basis.

Now we can perform numerics to see what effect a fully quantum mechanical treatment of atomic motion has on blockaded Rabi oscillations. In particular, we can simulate blockaded Rabi oscillations when the optical traps are turned off as well as when they are left on.

Numerics

We numerically simulate the time-evolution governed by the two atom Hamiltonian. In our experiment, we work with the $^3P_0$ Rydberg state of ^{8}8Sr with $n = 61$. For the C_6 interaction coefficient, we use the value from [55] which gives $C_6/2\pi = 275$ GHz μm^6. We work with mean atomic spacing of $a_0 = 3.6\mu m$. Thus the interaction strength is given by $V/2\pi \approx 130$ MHz.

Untrapped condition

First, we simulate the case where the traps are turned off as a base case. We know that the blockaded Rabi oscillations in this case can be high fidelity when we are well in the blockade regime. We start in a product state where the initial density matrix of the two atom system is a tensor product of the initial density matrices of the two individual atoms. We use parameters of $\Omega/2\pi = 1$ MHz, $\omega/2\pi = 100$ kHz ($\eta \approx 0.5$), $T = 2.5\mu K$ and $\alpha_g = \alpha_e = 0$. This means that the atoms start in a harmonic trap with trap frequency $\omega/2\pi = 100$ kHz, but just before the Rabi drive is turned on, we turn off the optical tweezers, conducting the experiment without any optical potential. We use a truncated Hilbert space for each atom, restricting to $N = 10$ harmonic oscillator energy levels per atom. The resultant two atom Hilbert space has dimension $4N^2 = 400$. We do see finite size effects as a result of truncating the Hilbert space beyond ~ 6 Rabi cycles. However, at short times, the truncation has no noticeable effects. See Figure 5.6.

The atomic population oscillates with high contrast between the ground state $|G\rangle$ and the maximally entangled state 'bright' state $|W\rangle$. The population in the the 'dark' state $|D\rangle = \frac{1}{\sqrt{2}}(|eg\rangle - |ge\rangle)$ as well as in the double excitation state $|R\rangle = |ee\rangle$ is negligible. Because the atoms are untrapped, we can see that the motional occupation number rapidly increases with time and keeps increasing unbounded. This is also seen in the spread of the atomic wavefunction with time. This means that in the absence of any trapping potential, the initially confined atomic wavepacket spreads out ballistically in time.

Non-magic trapping condition

We now repeat the simulation for the case of non-magic trapping. We use parameters of $\Omega/2\pi = 1$ MHz, $\omega/2\pi = 100$ kHz ($\eta \approx 0.5$), $T = 2.5\mu K$ and $\alpha_g = 1, \alpha_e = -1$ (anti-trapping). We use a truncated Hilbert space for each

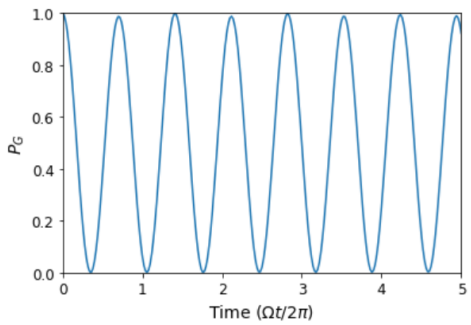

(a) Electronic ground state population P_G

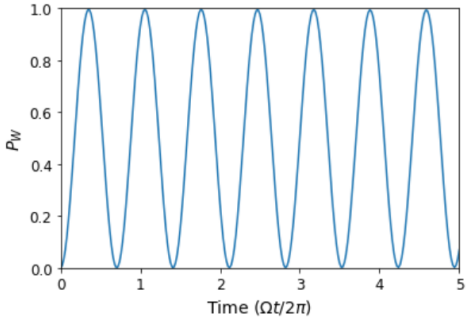

(b) Maximally entangled 'bright' state population P_W

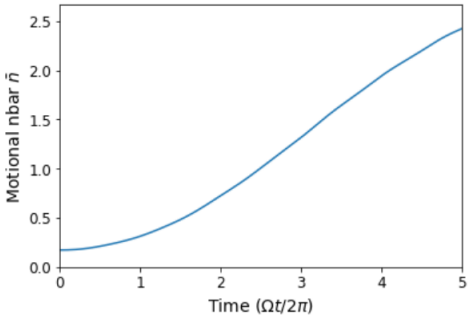

(c) Average motional occupation number $\bar{n}$

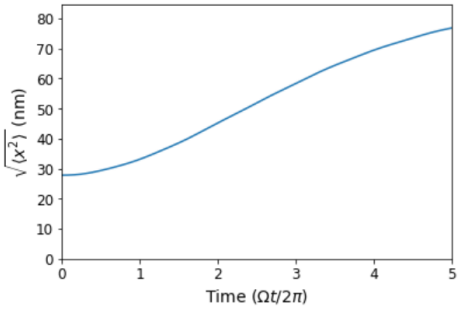

(d) Standard deviation of atomic position $\sqrt{\langle x_1^2 \rangle}$

Figure 5.6: Numerical simulation of blockaded Rabi oscillations in the untrapped case. See text for details.

atom, restricting to $N = 10$ harmonic oscillator energy levels per atom. The resultant two atom Hilbert space has dimension $4N^2 = 400$. We do not see any finite size effects as a result of truncating the Hilbert space. See Figure 5.7.

We see that the contrast of the Rabi oscillation between $|G\rangle$ and $|W\rangle$ is somewhat reduced compared to the untrapped case. However, as mentioned previously, in an experiment, we adiabatically ramp down the trap depth to mitigate this effect. The population in the doubly excited state $|R\rangle$ is negligible. However, the population in the dark state $|D\rangle$ is higher than in the untrapped case. Ramping down the trap depth can mitigate this effect as well. Looking at the average motional occupation number, we see that even for this anti-trapping configuration, the occupation number does not increase very rapidly. This can also be seen in the spread of the atomic wavefunction with time. This means that even the excited state is just as repelled by the optical potential as the

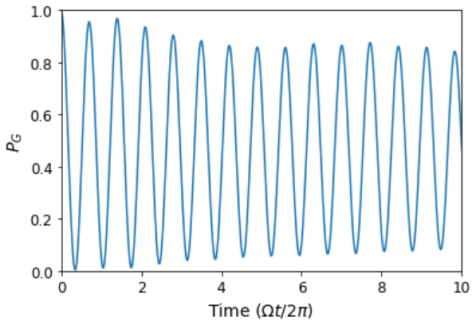

(a) Electronic ground state population P_G

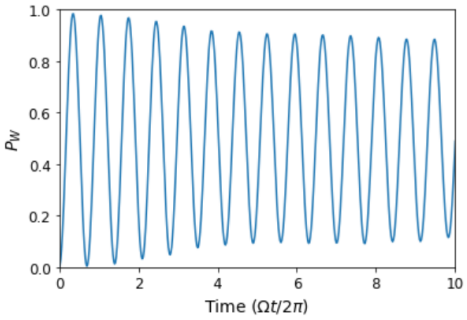

(b) Maximally entangled 'bright' state population P_W

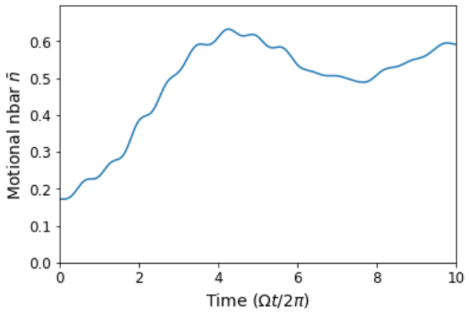

(c) Average motional occupation number $\bar{n}$

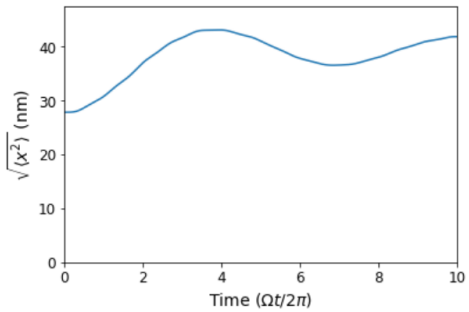

(d) Standard deviation of atomic position $\sqrt{\langle x_1^2 \rangle}$

Figure 5.7: Numerical simulation of blockaded Rabi oscillations in the non-magic trapping case. See text for details.

ground state is attracted to it, the net effect is that the atomic wavepacket does not expand nearly as quickly as in the untrapped case.

We numerically simulate the blockaded oscillations for different values of Ω and ω keeping the initial temperature constant at $T = 2.5\mu K$. We extract the pi-pulse fidelity F_π and two-pi-pulse fidelity $F_{2\pi}$. See Figure 5.8 for a parametric plot of the pi-pulse and two-pi-pulse infidelities $(1 - F)$. We see that decreasing trap frequency ω leads to higher fidelities while increasing Rabi frequency Ω only increases fidelity up to a certain point. Beyond this point, increasing Rabi frequency actually reduces the Pi-pulse fidelity because we start to weaken the Rydberg blockade constraint. We find that even for the anti-trapping condition, the fidelities achievable are quite high (at the 0.9999 level ignoring laser noise and spontaneous decay).

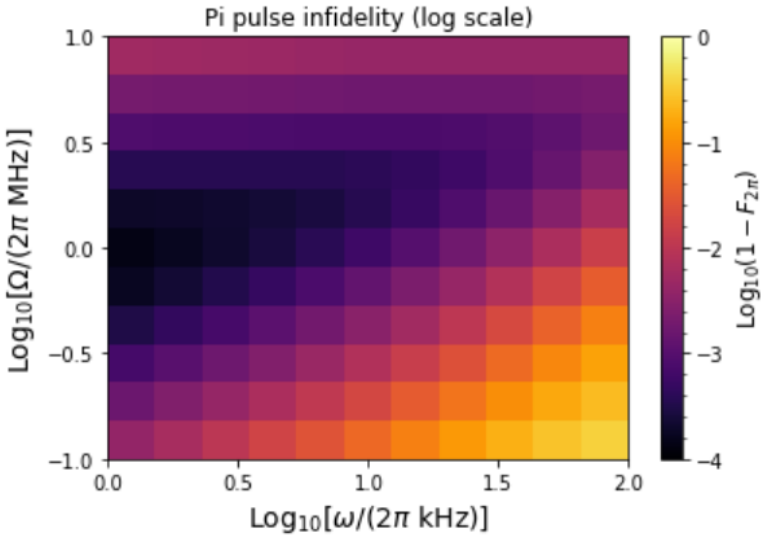

(a) Pi-pulse Infidelity $1 - F_{\pi}$

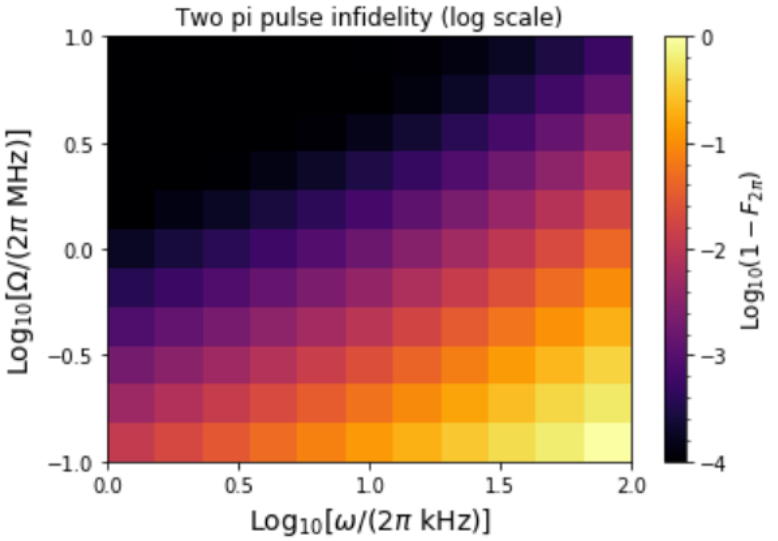

(b) Two-Pi-pulse Infidelity $1 - F_{2\pi}$

Figure 5.8: Blockaded Rabi oscillation fidelities extracted from numerical simulation for two atoms in a non-magic condition. See text for details.

Chapter 6

LADDER ARRAY

6.1 Introduction

An optical tweezer is simply a tightly focused laser beam. With an appropriate wavelength of light, these tweezers can trap or repel atoms and can be used to hold individual atoms. We can generate a single optical tweezer by simply focusing a laser beam using a convex lens. By sending multiple laser beams with slightly different angles into the same focusing lens, we can generate multiple optical tweezers. The position of the tweezers can be controlled by changing the angle of the laser beams. The more tightly focused a beam is, the more trapping force it can generate. Thus for AMO experiments, typically very tightly focusing lenses with short focal lengths are used.

In a standard tweezer array setup, an acousto-optic deflector (AOD) is used to generate an array of laser beams from a single input laser beam. Acousto-optic deflectors are devices that can deflect light by a variable angle controlled by the frequency of an electrical signal. By sending multiple electrical signals with different frequencies, we can generate multiple deflected laser beams from a single input beam. The optical power of the incoming laser beam gets distributed among the multiple deflected beams. The tweezers generated with the deflected beams thus have at most 1/N times the power of the incoming laser beam. Thus to scale to large system sizes, we need the laser power to scale with the number of tweezers we want to create. We are interested in reaching large system sizes for a variety of reasons. For quantum computing with atomic qubits, more number of atoms gives us more computational power. The Hilbert space that can be explored with N qubits grows as 2^N. Thus every additional qubit that we can get doubles our Hilbert space. For quantum metrology applications, for example, high precision optical clocks, the more atoms we have the faster we can reach a given precision by averaging the signal. Further, for studying thermodynamic properties of quantum systems, we want our system to be as large as possible to reduce boundary effects.

For the Strontium magic wavelength of 813nm, the commercially available laser power is limited to about 10W. The Ti:Saph laser used in the Endres lab

has an output power of just over 5W. However, to reach system sizes larger than 100 atoms, we need to more laser power. One possible solution is to use two separate lasers to double the total power. It is possible to coherently combine two lasers using appropriate monitoring and control of the frequency and relative phase of the two lasers. However, we can also use the two lasers to generate two parallel rows of tweezers. This configuration is known as a 'ladder array'.

Working in the ladder configuration not only allows us to reach larger N for the various applications mentioned earlier but also opens up many new physics directions. For example, by changing the separation between the two rows of tweezers, we could study the physics of two coupled quantum systems. By adjusting the position along the axis of the array, we can change the geometry to be either a square lattice or a triangular lattice. This changes the coordination number of each atom from 3 to 4 and also leads to more frustration in magnetic systems. There are additional possibilities of spin-1 physics[56], resonating valence bond[57, 58] physics and even lattice gauge theories[59] using spin ladder systems.

We built a prototype setup to test the feasibility of our method of combining optical tweezer arrays from two lasers into a tunable ladder configuration.

6.2 Laser Monitoring Setup and Calibration

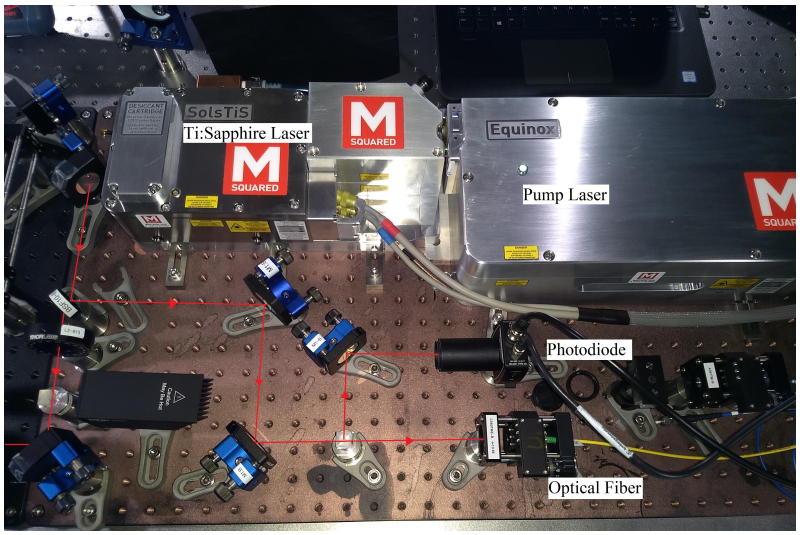

Figure 6.1: Laser pick-off stage

The laser we used for this prototype setup was a SolsTis Ti:Sapphire CW

laser with an Equinox pump laser both from Msquared. The SolsTis laser requires a pump beam at 532 nm and produces an output beam of upto that has a tunable wavelength from 725nm - 960nm. Thus we can use this laser to generate the 813.4nm light that we require for magic trapping of Strontium atoms. The Equinox pump laser is a high power 532nm laser that can provide up to 18W of pump power. Together this setup outputs up to 5.5W of 813nm light.

We first built a pick-off stage to monitor the laser power as well as wavelength. We sample a small fraction of the laser light using a pick-off plate and direct this light onto a photodiode to measure the intensity. We also couple this light into an optical fiber which can be connected to a wavemeter to measure the wavelength. We calibrate the photodiode voltage reading by changing the pump power from the Equinox, measuring the laser power with a thermal-head power meter and recording the corresponding photodiode voltage. Note that at the max pump power of 18W, we have an output power of 5W. We obtain a clean linear calibration curve.

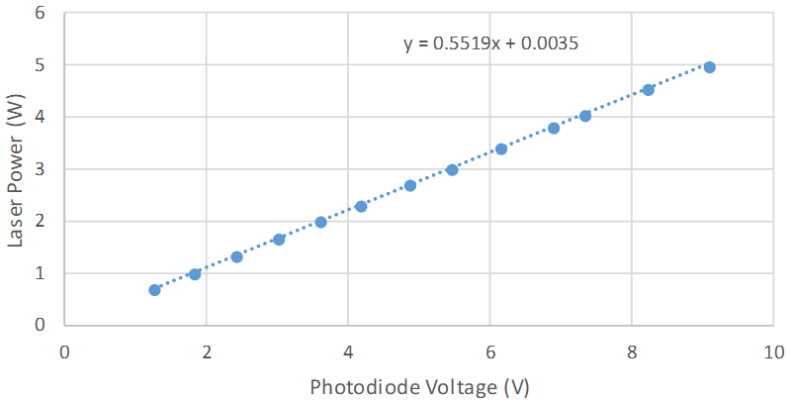

Figure 6.2: Laser power calibration

6.3 Acousto-Optic Deflectors (AOD) Setup

Acousto-optic deflectors take in sinusoidal radio-frequency (RF) electrical tones and generate deflected beams. The RF tones drive a piezoelectric transducer which generates sound waves in the AOD crystal. Incoming light undergoes Bragg diffraction off the periodic density modulation caused by the sound waves. The diffraction efficiency is given by the ratio of the power in the deflected beam to the power in the incoming beam. As we increase the RF power, the diffraction efficiency increases until a certain threshold beyond which the

AOD can get damaged. The AOD we used here was DTSX-400-810.920 from AA Opto Electronic. The damage threshold for this AOD was 2W (or 33 dBm).

We generate the RF signals using an AWG which is controlled by MATLAB from a computer. We used the existing design of RF amplification and filtering to boost the AWG output to the level required to drive the AOD. The output from the AWG was passed through a high pass filter (41-800 MHz) followed by a low pass filter (DC - 140 MHz) and then through an RF amplifier (Gain $\approx$ 35). We can digital scale the amplitude of the AWG to control the RF power supplied to the AOD. We calibrate the digital amplitude scaling factor to RF output power by measuring the RF power using a spectrum analyzer.

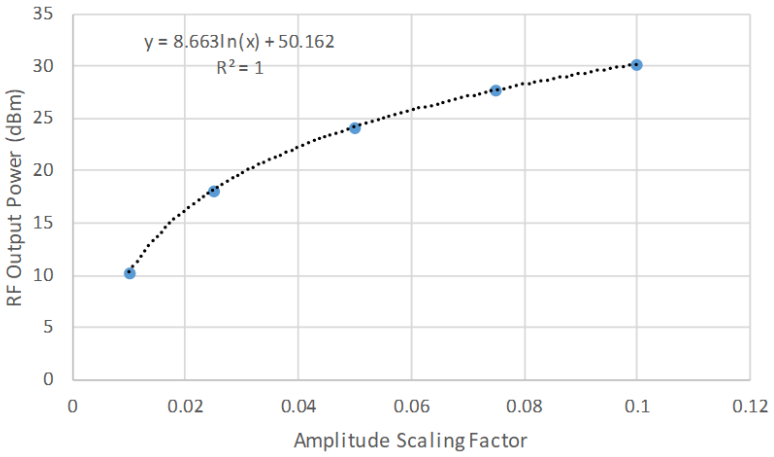

Figure 6.3: Calibrating RF power supplied to the AOD

6.4 Imaging Stage

In the real experimental setup, we use high power objective lenses with short focal lengths (f = 4mm) and large numerical appertures (NA $\approx$ 0.5). These lenses are custom made to have high transmission at the various wavelengths required for trapping, cooling and imaging Strontium atoms, and cost tens of thousands of dollars. For the purposes of the prototype setup, we used simple achromat doublet lenses with a relatively short focal lengths (f = 35 mm) as a substitute for the objectives. We used a Basler camera (acA3800-14um) with an imaging lens to image the tweezers produced in the focal plane of our mock objectives. Using these components we can generate and image a single row of tweezers as in a standard experimental setup. We image a few different array sizes as a test. After confirming that all the components are working as

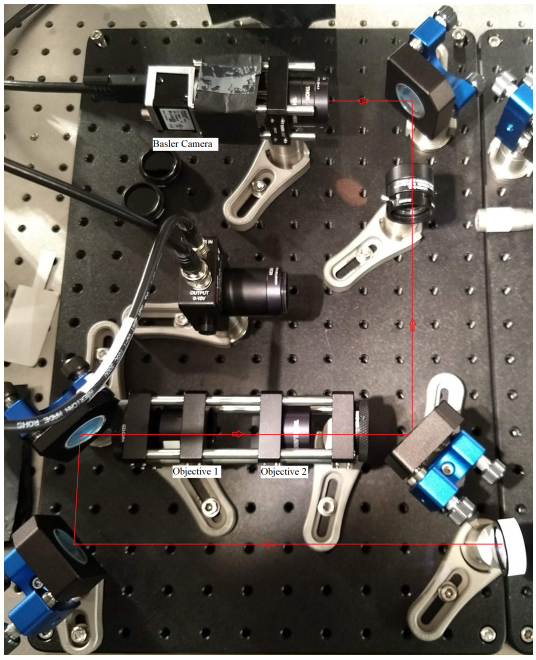

Figure 6.4: Objective lenses and imaging camera

expected, we can move to generating and combining two rows of tweezers.

6.5 Combining two rows of tweezers

In a real experimental situation, we would like to combine two rows of tweezers from two independent lasers to double the available laser power and reach larger system sizes. However, for the prototype setup, we use a single laser and one AOD to generate one array of tweezers and use a 50:50 splitter to duplicate this tweezer array. This allows us to perform a proof of principle test for the combining technique without having to use two AODs.

Now, to generate the ladder array, we want to combine two beams of light that can each generate an array of tweezers. When combining two beams of light with opposite polarization, we typically use a polarizing beam splitter (PBS). The PBS selectively reflects light of only one polarization and allows the opposite polarization light to pass through unaffected. However, for the ladder arrays we require both arrays to have the same polarization to allow for laser cooling with a global cooling beam. Thus we cannot use a PBS to combine the two beams of light.

Instead we use a D-shaped mirror (which is just a mirror with a sharp edge). We allow one beam of light to pass by the edge of the mirror (analogous to

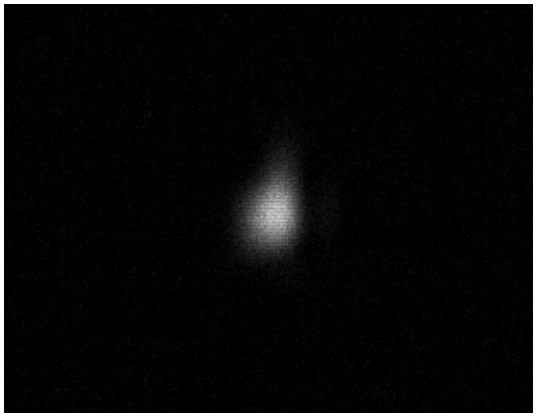

(a) Single tweezer

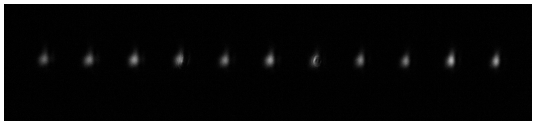

(b) 11 tweezers

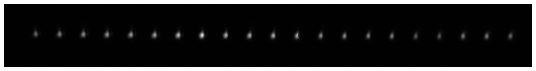

(c) 21 tweezers

Figure 6.5: Imaging a single row of tweezers. There is some spherical aberration in the tweezers because of the plano-convex lenses combined with slight misalgnment in the objectives.

the beam that goes through the PBS). And we reflect the other beam of light of the D-mirror very close to the edge of the mirror (analogous to the beam that is reflected by the PBS). Using this method, the two laser beams cannot be overlapped with each other but can be brought very close to each other, limited only by diffraction off the edge of the mirror.

We combine the two rows of tweezers in the focal plane of a lens with a large focal length (we use f = 150mm). Using a telescope, this focal plane maps directly to the focal plane of the objective lens. For the ladder configuration, we want to generate two arrays of tweezers that are parallel to each other with a given separation. To be concrete, let the direction of propagation of light be along the z-direction, and the axis of the first array be in the x-direction. Then, if all goes well then the second array is at the same z-position and is the parallel to the first array, separated only in the y-direction. However, in general, the second array could be focused at a different z-position compared to the first array and could be at some arbitrary angle (in the XY plane) with respect

to the first array. To correct this we need to adjust the relative z-position, relative angle between the axes of the array as well as the y-separation. We can perform these adjustments as follows:

- Adjusting the relative z-position: The focal plane in which we combine the two laser beams on the D-mirror gets mapped with a telescope to the focal plane of the objectives. Thus, by adjusting the path length of the laser beams before the D-mirror, we can ensure that the two beams focus at the same z-position. We do this by adding mirrors mounted on translation stages for both laser beams.

- Adjusting the relative angle: The relative angle between the arrays can be adjusted by rotating the wavefront of one of the beams. This can be done using a periscope - changing the angle of one of the mirrors in the periscope rotates the wavefront. In practice, the angle between the arrays is very small and can be corrected using a procedure similar to beam walking with the periscope mirrors.

- Adjusting the y-separation: Once the arrays are parallel to each other, we can adjust their y-displacement using the D-mirror on which the two beams are combined. By changing the separation between the two beams at the D-mirror, we can change the separation in the focal plane of the objectives (since the two focal planes are mapped to each other with a telescope).

- Adjusting the x-separation: If the teo arrays have zero x-offset, then they form a square-lattice ladder geometry. We can beam-walk to change the x-offset to generate a triangular lattice ladder geometry or anything in between.

6.6 Translation Stage Setup

We implement the translation stages for z-position control using sliding breadboards. We mount a periscope on each of the 2 translation stages to allow us to rotate the angle of both the rows of tweezers. We also mount the D-mirror on a 2D translation stage to allow for control of the y-separation between the two tweezers arrays. See figure for the layout on the optical table.

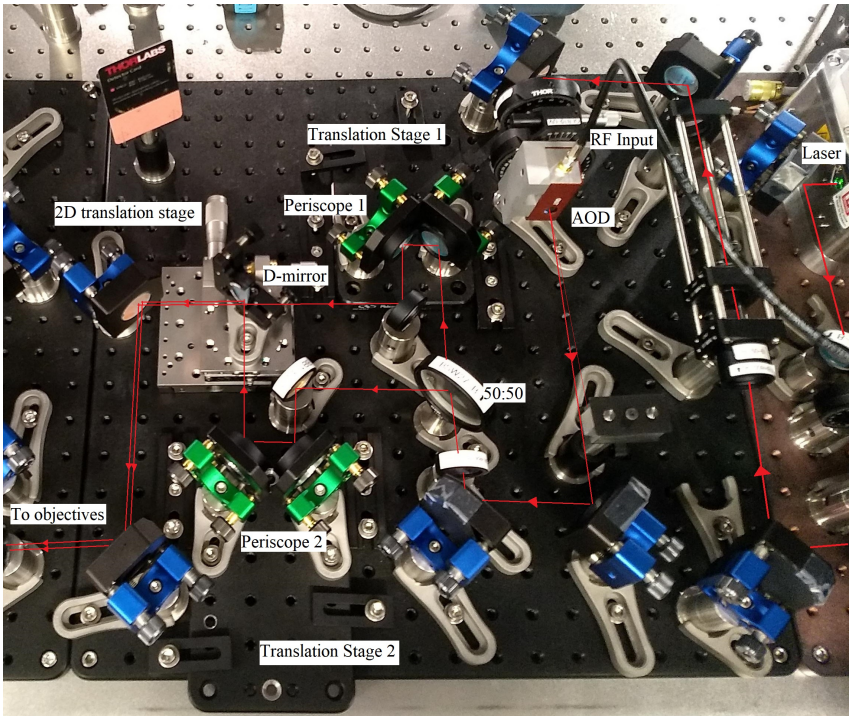

Figure 6.6: Layout of the translation stages and D-mirror for combination of the two tweezer arrays

6.7 Imaging and 'Live' Aligning the ladder array

Using this setup, we generated, combined and imaged two rows of tweezers. By monitoring the video stream from the imaging camera, we can make sure both arrays are focused in the same plane and roughly align the two rows. However, to help with fine alignment, we wrote a MATLAB script to image the tweezers, compute the angle between the rows and their y-separation. Using this tool, we can eliminate any angle between the rows and precisely adjust the inter-row separation.

6.8 Test of Stability

Finally, we perform a test of the mechanical stability of the setup. Once we align our optics, we would like our setup to remain well aligned for hours (if not days) while we take data. Drifts in alignment can ruin data quality and add a lot of overhead time in the daily experimental procedure. Thus, mechanical stability is an important consideration in AMO experiments. We logged the position and angle data using the same MATLAB live alignment tool. We found that the setup was sufficiently stable over the course of several hours despite the numerous translation stages and the D-mirror beam combining.

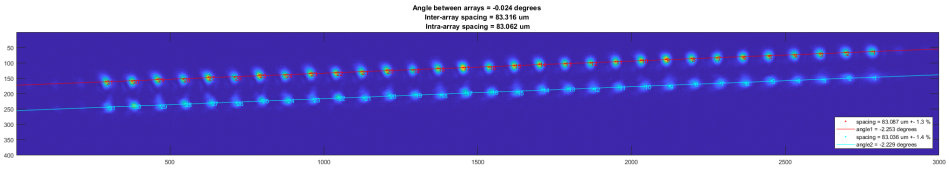

(a) Live alignment tool

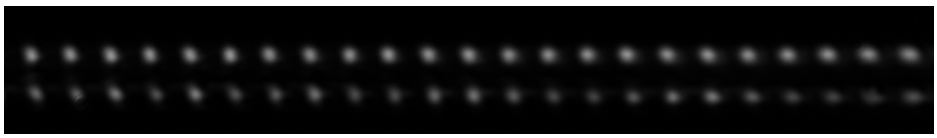

(b) Square lattice ladder geometry

Figure 6.7: Imaging and Live aligning the ladder array

The drift in the inter-row separation was about 0.5% over the course of 4 hours. The drift in the relative angle between the rows of tweezers was about 0.02 degrees over 4 hours.

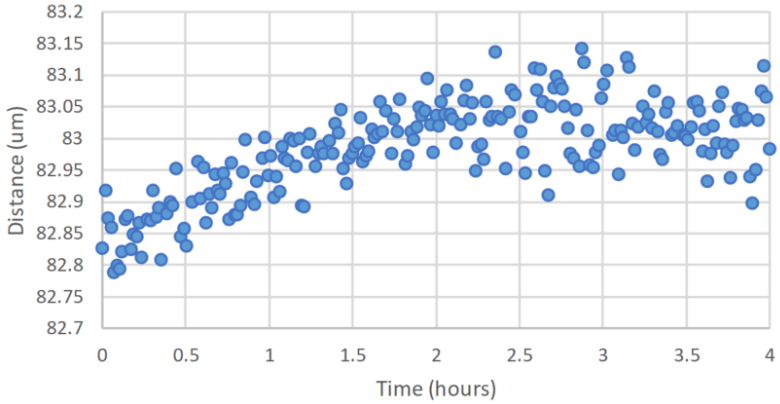

(a) Inter-row separation

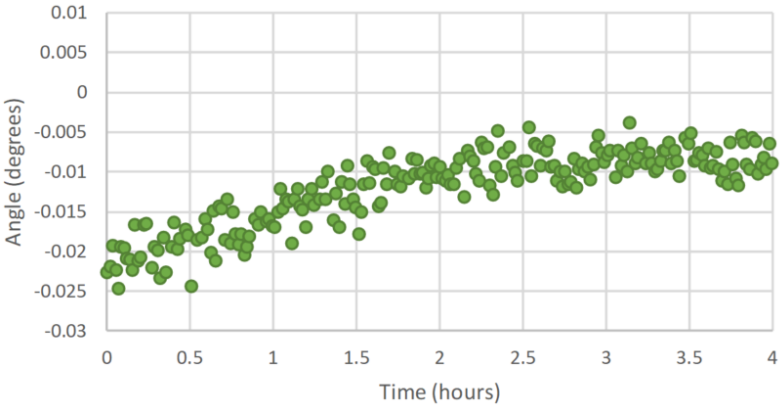

(b) Relative angle between rows

Figure 6.8: Mechanical stability of the setup

Chapter 7

CONCLUSION AND OUTLOOK

In this thesis, we have analyzed the effect of various sources of decoherence on single atom and Rydberg blockaded Rabi oscillations. For the case of untrapped atoms, we provided upper bounds on experimentally achievable single atom and blockaded π-pulse fidelities in terms of the experimentally measured noise power spectral densities (PSDs) and atomic temperature. We derived analytic 'window' functions which select specific components of the laser intensity and frequency noise spectra, helping us understand the dependence of the Rabi oscillation fidelity on Rabi frequency. We find good agreement of our perturbative result with numerics and recent experimental work from the group. We also studied Rabi oscillations of trapped atoms in the non-magic trapping condition. We found that when the Rabi frequency is much larger than the harmonic trapping frequency, the single atom and blockaded π-pulse fidelity can still be quite high. Finally, we turned towards the question of near-term scalability of the experimental system. We built and tested a method for generating a 'ladder' configuration of optical tweezers utilizing two independent lasers in a way that allows us to fully tune the geometry of the ladder. We tested the mechanical stability of our setup and found its performance satisfactory. This pseudo-2D configuration would enable us to reach larger system sizes in the near future, whilst also allowing us to access beyond 1D physics.

7.1 Outlook

Our perturbative analysis of Rabi oscillations can be written in terms of a diagrammatic expansion as shown in Appendix B. This diagrammatic bookkeeping can facilitate the generalization of this method to the case of quantum operations with multiple pulses. For example, a Ramsey measurement involves 2 laser pulses separated by a duration of free-evolution. While the number of diagrams contributing at second-order in perturbation theory grows rapidly with the number of pulses, we can apply certain finite-correlation time approximations for the noise sources to reduce the number of tedious calculations required. Such a generalized method would be a powerful tool for studying

the effects of noise on quantum operations.

In this thesis, we used a metastable clock state $|g\rangle$ as the ground state and a Rydberg state $|r\rangle$ as the excited state of our qubit. Instead, to fully leverage the properties of the atoms we would like to use two long-lived states (such as $|a\rangle$ and $|g\rangle$) as our qubits. These states have very long coherence times are non-interacting. We can turn on interactions between these qubits by driving to Rydberg states as proposed in [36] and demonstrated in [24], or as proposed and demonstrated in [16]. We can analyze the fidelities of such entangling gates by considering working with 3 states per atom ($|a\rangle, |g\rangle, |r\rangle$) and using the generalized diagrammatic approach for multiple pulses. Preliminary numerics of these gates indicate a functional dependence of fidelity on Rabi frequency similar to that for single atom Rabi oscillations.

Regarding the ladder array prototype, we would like to integrate this design with the main experiment to reach larger system sizes. Additionally, we would like to exploit the pseudo-2D nature of the ladder configuration to explore the physics of spin-ladders[56], Haldane physics [60] and resonating valence bond (RVB) [57, 58] physics.

Appendix A

CALCULATIONS FOR NOISY RABI OSCILLATIONS

A.1 Doppler effect calculations

From Eq. (4.30), the excited state population for a given initial momentum p is given by:

$$\rho_{rr}(t;p) \approx \frac{1-\xi^2}{2} - \frac{1-\xi^2}{2}\cos\left(\Omega t(1+\frac{\xi^2}{2})\right) \tag{A.1}$$

Picking up from Eq. (4.33) and using the probability distribution of ξ is $P(\xi) = \mathcal{N}(0,\xi_0^2)$, we have:

$$\begin{aligned}
\overline{\rho_{rr}(t)} &= \int d\xi P(\xi)\rho_{rr}(t) \\
&\approx \int d\xi P(\xi)\frac{1-\xi^2}{2} - \int d\xi P(\xi)\frac{1-\xi^2}{2}\cos\left(\Omega t(1+\frac{\xi^2}{2})\right) \\
&= \frac{1-\xi_0^2}{2} - \int \frac{d\xi}{\sqrt{2\pi}\xi_0} e^{-\frac{\xi^2}{2\xi_0^2}} \frac{1-\xi^2}{2} \frac{e^{i\Omega t + i\Omega t\frac{\xi^2}{2}} + \text{c.c.}}{2} \\
&= \frac{1-\xi_0^2}{2} - \left[\frac{e^{i\Omega t}\sigma(t)}{4\xi_0}\int \frac{d\xi}{\sqrt{2\pi}\sigma(t)}(1-\xi^2)e^{\frac{-\xi^2}{2\sigma(t)^2}} + \text{c.c.}\right] \\
&= \frac{1-\xi_0^2}{2} - \left[\frac{e^{i\Omega t}\sigma(t)}{4\xi_0}(1-\sigma(t)^2) + \text{c.c.}\right]
\end{aligned}$$

where $\sigma^2(t) = \frac{\xi_0^2}{1-i\Omega t\xi_0^2}$. We can re-write this more suggestively as:

$$\overline{\rho_{rr}(t)} \approx \frac{1-\xi_0^2}{2} - \frac{|\sigma(t)(1-\sigma(t)^2)|}{\xi_0}\frac{\cos\left(\Omega t + \phi(t)\right)}{2} \tag{A.2}$$

where $\phi(t) = \arg(\sigma(t)(1-\sigma(t)^2)$ is the doppler-induced time-dependent phase shift and the decay envelope is given by:

$$\frac{|\sigma(t)(1-\sigma(t)^2)|}{\xi_0} \approx \frac{1}{(1+\Omega^2t^2\xi_0^4)^{1/4}}\left(1 - \frac{\xi_0^2}{1+\Omega^2t^2\xi_0^4}\right) \tag{A.3}$$

This envelope has a decay time scale of $\tau = \frac{1}{\Omega\xi_0^2} = \frac{\Omega}{\sigma_\delta^2}$. Since $\phi(t) \ll \pi$ for short times, we can estimate the π-pulse fidelity by ignoring $\phi(t)$ and plugging in $t = \pi/\Omega$. This gives us $\mathcal{F}_\pi \leq 1 - \xi_0^2$

A.2 Single Atom Frequency Noise Calculations

We start in known initial state $\rho(0) = |g\rangle\langle g|$ and we are interested in the population of the excited state as a function of time $\overline{\rho_{rr}(t)}$. Thus we focus

on the matrix element $\langle r|\, U(t)\, |g\rangle$. Explicitly writing this out to 2nd order in perturbation, we have:

$$\langle r|\, U(t)\, |g\rangle = -i \sin\frac{\Omega t}{2} - \frac{1}{2}\int_0^t dt_1 \nu(t_1)\left(\sin\frac{\Omega t}{2}\cos\Omega t_1 - \cos\frac{\Omega t}{2}\sin\Omega t_1\right)$$
$$+ \frac{i}{4}\int_0^t dt_1 \int_0^{t_1} dt_2 \nu(t_1)\nu(t_2)\left(\sin\frac{\Omega t}{2}\cos\Omega(t_1-t_2) - \cos\frac{\Omega t}{2}\sin\Omega(t_1-t_2)\right)$$
$$+ O(\nu^4 t^4) \quad \text{(A.4)}$$

We compute $|\,\langle r|\, U(t)\, |g\rangle\,|^2$ keeping only terms up to second order and then average over the ensemble. In doing so, we use $\overline{\nu(t')\nu(t'')} = K_\nu(t''-t')$.

$$\overline{|\,\langle r|\, U(t)\, |g\rangle\,|^2} = \sin^2\frac{\Omega t}{2} - \frac{1}{4}\int_0^t dt_1 \int_0^{t_1} dt_2 K_\nu(t_2-t_1)\big[\cos\Omega(t_2-t_1) -$$
$$\cos\Omega t\cos\Omega(t_2-t_1) + \sin\Omega t\sin\Omega(t_2-t_1)\big]$$
$$+ \frac{1}{8}\int_0^t dt_1 \int_0^t dt_2 K_\nu(t_2-t_1)\big[\cos\Omega(t_2-t_1) - \cos\Omega t\cos\Omega(t_2+t_1)$$
$$+ \sin\Omega t\sin\Omega(t_2+t_1)\big] \quad \text{(A.5)}$$

Further, we decouple the two integrals over time by writing the two-point correlation function in terms of its fourier transform i.e. the power spectral density, i.e., $K_\nu(t_2-t_1) = \int \frac{d\omega}{2\pi} S_\nu(\omega)\cos\omega(t_2-t_1)$:

$$\overline{|\,\langle r|\, U(t)\, |g\rangle\,|^2} = \frac{1}{2} - \frac{1}{8}\int \frac{d\omega}{2\pi} S_\nu(\omega)\int_0^t dt_1\Big[2\int_0^{t_1} dt_2 \cos\omega(t_2-t_1)\cos\Omega(t_2-t_1)$$
$$- \int_0^t dt_2 \cos\omega(t_2-t_1)\cos\Omega(t_2-t_1)\Big]$$
$$+ \cos\Omega t\Big(-\frac{1}{2} + \frac{1}{8}\int \frac{d\omega}{2\pi} S_\nu(\omega)\int_0^t dt_1\Big[2\int_0^{t_1} dt_2 \cos\omega(t_2-t_1)\cos\Omega(t_2-t_1)$$
$$- \int_0^t dt_2 \cos\omega(t_2-t_1)\cos\Omega(t_2+t_1)\Big]\Big)$$
$$+ \sin\Omega t\Big(\frac{1}{8}\int \frac{d\omega}{2\pi} S_\nu(\omega)\int_0^t dt_1\Big[2\int_0^{t_1} dt_2 \cos\omega(t_2-t_1)\sin\Omega(t_2-t_1)$$
$$- \int_0^t dt_2 \cos\omega(t_2-t_1)\sin\Omega(t_2+t_1)\Big]\Big) \quad \text{(A.6)}$$

The first integral vanishes. The second one gives us W_1 and the third one gives use W_2. That is, we define W_1 and W_2 as below:

$$\begin{aligned} W_1(\omega,\Omega,t) &= \frac{1}{t^2}\int_0^t dt_1\Big[2\int_0^{t_1} dt_2 \cos\omega(t_2-t_1)\sin\Omega(t_2-t_1) \\ &\quad - \int_0^t dt_2 \cos\omega(t_2-t_1)\sin\Omega(t_2+t_1)\Big] \\ &= \Big(3\Omega^2+\omega^2+(\Omega^2-\omega^2)\cos 2\Omega t - 4\Omega^2\cos\Omega t\cos\omega t \\ &\quad - 4\Omega\omega\sin\Omega t\sin\omega t\Big)/\Big((\Omega^2-\omega^2)^2t^2\Big) \end{aligned} \tag{A.7}$$

$$\begin{aligned} W_2(\omega,\Omega,t) &= \frac{1}{t^2}\int_0^t dt_1\Big[2\int_0^{t_1} dt_2 \cos\omega(t_2-t_1)\cos\Omega(t_2-t_1) \\ &\quad - \int_0^t dt_2 \cos\omega(t_2-t_1)\cos\Omega(t_2+t_1)\Big] \\ &= \Big(4\Omega\omega\cos\Omega t\sin\omega t + (\Omega^2-\omega^2)(2\Omega t+\sin 2\Omega t) \\ &\quad - 4\Omega^2\sin\Omega t\cos\omega t\Big)/\Big((\Omega^2-\omega^2)^2t^2\Big) \end{aligned} \tag{A.8}$$

This gives us equation (4.21).

A.3 Blockade Hamiltonian

The two atom (noisy) drive and interaction Hamiltonian is given by:

$$\begin{aligned} H &= \frac{\hbar\Omega(t)}{2}\left(e^{-ik_Lx_1}\sigma_1^+ + e^{-ik_Lx_2}\sigma_2^+ + \text{h.c.}\right) \\ &\quad + \frac{\hbar\nu(t)}{2}\left(\sigma_1^z+\sigma_2^z\right) + V(x_1,x_2)\,|r_1r_2\rangle\langle r_1r_2| \end{aligned} \tag{A.9}$$

where $\sigma_1^\mu = \sigma^\mu\otimes\mathbb{1}$ and $\sigma_2^\mu = \mathbb{1}\otimes\sigma^\mu$. We can explicitly write this Hamiltonian in the $|g\rangle$, $|w\rangle$, $|d\rangle$ and $|r\rangle$ basis (where $|r\rangle \equiv |r_1r_2\rangle$) as $H = \sum_{i,j}|i\rangle\langle i|\,H\,|j\rangle\langle j|$ with $i,j\in(g,w,d,r)$.

$$\begin{aligned} H &= \frac{\hbar\Omega(t)\sqrt{2}}{2}\left(|w\rangle\langle g| + e^{-ik_L(x_1+x_2)}|r\rangle\langle w| + \text{h.c.}\right) \\ &\quad + \frac{\hbar\nu(t)*2}{2}\left(|g\rangle\langle g| - |r\rangle\langle r|\right) + V(x_1,x_2)\,|r\rangle\langle r| \end{aligned}$$

Ignoring the $|r\rangle$ state because of the Rydberg blockade effect, and adding a constant offset, we get:

$$H = \frac{\hbar\Omega_2}{2}X_{gw} + \left(\frac{\hbar\Omega_2\epsilon(t)}{2}X_{gw} + \frac{\hbar\nu(t)}{2}(Z_{gw} - |d\rangle\langle d|)\right) \tag{A.10}$$

where $X_{gw} = |g\rangle\langle w| + |w\rangle\langle g|$ and $Z_{gw} = |g\rangle\langle g| - |w\rangle\langle w|$.

Blockade Motional Effects

The drive Hamiltonian (in the rotating wave approximation) is given by:

$$H = \frac{p_1^2}{2m} + \frac{p_2^2}{2m} + \frac{\hbar\Omega}{2}\left(e^{-ik_L x_1}\sigma_1^+ + e^{-ik_L x_2}\sigma_2^+ + \text{h.c.}\right) \tag{A.11}$$

Let us first start in the basis $|(p_1, s_1), (p_2, s_2)\rangle$ where $s_i \in (g_i, r_i)$ and p_i represent the atomic momenta. The Rabi drive terms couple the state $|(p_1, g_1), (p_2, s_2)\rangle$ to $|(p_1 - \hbar k_L, r_1), (p_2, s_2)\rangle$, and the state $|(p_1, s_1), (p_2, g_2)\rangle$ to $|(p_1, r_1), (p_2 - \hbar k_L, r_2)\rangle$. We eliminate the doubly-excited states (because of the Rydberg blockade) and changing basis to the more convenient form $|p_1, p_2, s\rangle$ where $s \in (g, w, d)$:

$$\begin{aligned}
|p_1, p_2, g\rangle &= |(p_1, g_1), (p_2, g_2)\rangle \\
|p_1, p_2, w\rangle &= \frac{|(p_1 - \hbar k_L, r_1), (p_2, g_2)\rangle + |(p_1, g_1), (p_2 - \hbar k_L, g_2)\rangle}{\sqrt{2}} \\
|p_1, p_2, d\rangle &= \frac{|(p_1 - \hbar k_L, r_1), (p_2, g_2)\rangle - |(p_1, g_1), (p_2 - \hbar k_L, g_2)\rangle}{\sqrt{2}}
\end{aligned}$$

Assembling these together into a pseudo-spinor $\Gamma(p_1, p_2)$,

$$\Gamma(p_1, p_2) = \begin{pmatrix} |p_1, p_2, g\rangle \\ |p_1, p_2, w\rangle \\ |p_1, p_2, d\rangle \end{pmatrix} \tag{A.12}$$

we can see easily that $\Gamma^\dagger(p_1', p_2')\ H\ \Gamma(p_1, p_2)$ is non-zero only when $p_1 = p_1'$ and $p_2 = p_2'$. Thus, we can write the Hamiltonian as:

$$\begin{aligned}
H = &\int dp_1 dp_2\ \Gamma(p_1, p_2) \\
&\times \begin{bmatrix} \frac{p_1^2+p_2^2}{2m} & \frac{\hbar\Omega_2}{2} & 0 \\ \frac{\hbar\Omega_2}{2} & \frac{p_1^2+p_2^2+\hbar^2k_L^2}{2m} - \frac{\hbar k_L(p_1+p_2)}{2m} & \frac{\hbar k_L(p_2-p_1)}{2m} \\ 0 & \frac{\hbar k_L(p_2-p_1)}{2m} & \frac{p_1^2+p_2^2+\hbar^2k_L^2}{2m} - \frac{\hbar k_L(p_1+p_2)}{2m} \end{bmatrix} \Gamma^\dagger(p_1, p_2)
\end{aligned} \tag{A.13}$$

which is the same as Eq. (4.50) up to a constant energy shift (and absorbing the $\hbar^2 k_L^2/2m$ term into the transition energy). We solve the resultant dynamics perturbatively assuming the Doppler shifts are much smaller than the Rabi frequency. Suppressing the momentum degrees of freedom once again, we write the bare Hamiltonian as:

$$H_0 = \frac{\hbar\Omega_2}{2} X_{gw} \tag{A.14}$$

and the perturbation Hamiltonian as:

$$H_1 = \frac{\hbar\delta_1}{2}(|g\rangle\langle g| - X_{wd}) + \frac{\hbar\delta_2}{2}(|g\rangle\langle g| + X_{wd}) \tag{A.15}$$

where $\delta_j = k_L p_j/m$. We calculate the perturbed time-evolution operator up to second order using Eq. (4.19) by straight forward integration, giving us:

$$\langle w|\, U(t)\, |g\rangle = -i \sin\frac{\Omega_2 t}{2} - \frac{(\delta_1+\delta_2)t}{4}\sin\frac{\Omega_2 t}{2} + i(\delta_1^2+\delta_2^2)\left((\frac{t^2}{32}+\frac{5}{16\Omega_2^2})\sin\frac{\Omega_2 t}{2} + \frac{5t}{16\Omega_2}\cos\frac{\Omega_2 t}{2}\right) + O(\delta_i^4 t^4) \quad \text{(A.16)}$$

Averaging over the ensemble, we assume that the momentum distributions p_j and hence the doppler detuning distributions δ_j are Gaussian (see Eq. (4.32)). We assume homogenous temperature and trap depth, i.e., $\overline{\delta_1^2} = \overline{\delta_2^2} = \overline{\delta^2}$. To second order in the perturbation, the bright state population is given by:

$$\overline{\rho_{ww}(t)} = \left(\frac{1}{2} - \frac{5\overline{\delta^2}}{4\Omega_2^2}\right)(1-\cos\Omega_2 t) + \frac{\overline{\delta^2} t}{8\Omega_2}\sin\Omega_2 t + O(\delta^4 t^4) \quad \text{(A.17)}$$

We can also look at the dark state population using:

$$\langle d|\, U(t)\, |g\rangle = \frac{(\delta_1-\delta_2)}{\Omega_2}\left(1-\cos\frac{\Omega_2 t}{2}\right) - i(\delta_1^2-\delta_2^2)\left(\frac{1}{2\Omega_2^2}\sin\frac{\Omega_2 t}{2} - \frac{t}{4\Omega_2}\cos\frac{\Omega_2 t}{2}\right) + O(\delta_i^4 t^4) \quad \text{(A.18)}$$

Averaging over the ensemble, we find:

$$\overline{\rho_{dd}(t)} = \frac{\overline{\delta^2}}{\Omega_2^2}\left(3-\cos\Omega_2 t - 4\cos\frac{\Omega_2 t}{2}\right) + O(\delta^4 t^4) \quad \text{(A.19)}$$

A.4 White Noise: Markovian Process

The limit of white frequency noise has been well studied in literature [45, 46]. We present the results here for completeness. Assuming the noise correlation function is $\overline{\nu(t)\nu(t')} = \alpha\delta(t-t')$ (Gaussian white noise) we get the following Optical Bloch Equations (OBE):

$$\frac{d}{dt}\begin{pmatrix}\overline{\rho_{gg}(t)}\\ \overline{\rho_{rg}(t)}\\ \overline{\rho_{gr}(t)}\\ \overline{\rho_{rr}(t)}\end{pmatrix} = -\frac{i}{2}\begin{bmatrix}0 & -\Omega & \Omega & 0\\ -\Omega & -i\alpha & 0 & \Omega\\ \Omega & 0 & -i\alpha & -\Omega\\ 0 & \Omega & -\Omega & 0\end{bmatrix}\begin{pmatrix}\overline{\rho_{gg}(t)}\\ \overline{\rho_{rg}(t)}\\ \overline{\rho_{gr}(t)}\\ \overline{\rho_{rr}(t)}\end{pmatrix} \quad \text{(A.20)}$$

Starting in a pure initial state $\rho(0) = |g\rangle\langle g|$, we have:

$$\overline{\rho_{rr}(t)} = \frac{1}{2} - e^{-\alpha t/4}\left(\frac{\cos\Omega' t}{2} + \frac{\alpha\sin\Omega' t}{4\Omega'}\right) \quad \text{(A.21)}$$

where $\Omega' = \sqrt{\Omega^2 - \alpha^2/16}$ and $\mathcal{F}_\pi \lesssim (1+e^{-\frac{\alpha\pi}{4\Omega}})/2$.

A p p e n d i x B

DIAGRAMMATIC APPROACH IN THE EIGENBASIS

B.1 Abstract

Instead of calculating the effect of laser noise on Rabi oscillations starting iwith a fixed initial state (i.e. $|g\rangle\langle g|$), we calculate the effect of laser noise on the quantum channel that maps the initial density matrix to the final density matrix. The fidelity of this operation is then given my the maximal distance between the effect of pure channel on a density matrix and the effect of the noisy channel on the same density matrix.

B.2 Set up

The drive hamiltonian is given by:

$$H_0 = \frac{\hbar\Omega}{2}(|r\rangle\langle g| + |g\rangle\langle r|) \tag{B.1}$$

The eignenstates of this Hamiltonian are:

$$\begin{aligned} |\pm\rangle &= \frac{1}{\sqrt{2}}(|g\rangle \pm |r\rangle) \\ E_\pm &= \pm\frac{\hbar\Omega}{2} \end{aligned} \tag{B.2}$$

Let us define $|0\rangle \equiv |+\rangle$ and $|1\rangle \equiv |-\rangle$. Writing all matrices in this basis, we get:

$$\begin{aligned} H_0 &= \frac{\hbar\Omega}{2}\sigma^z \\ H_1(t) &= \frac{\hbar\nu(t)}{2}\sigma^x \end{aligned} \tag{B.3}$$

The time-evolution operator is given by

$$\begin{aligned} U_0(t) &= e^{-\frac{iH_0t}{\hbar}} = e^{-\frac{i\Omega t}{2}\sigma^z} \\ [U_0(t)]_{\alpha\beta} &= \langle\alpha|\, U_0(t)\, |\beta\rangle = e^{-\frac{i\Omega t}{2}(-1)^\alpha}\delta_{\alpha\beta} \end{aligned} \tag{B.4}$$

The density matrix evolves under the action of H_0 as:

$$\begin{aligned} \rho(t) &= U(t)\rho(0)U(t)^\dagger \\ [\rho(t)]_{\alpha\beta} &= \sum_{\mu,\nu}[U(t)]_{\alpha\mu}[\rho(0)]_{\mu\nu}[U(t)^\dagger]_{\nu\beta} \end{aligned} \tag{B.5}$$

This quantum channel can be pictured as below. $U_0(t)$ takes $|\mu\rangle$ forward in time and $U_0(t)^\dagger$ takes $\langle\nu|$ backwards in time.

$$|\alpha\rangle \xleftarrow{U_0(t)} |\mu\rangle$$

$$\langle\beta| \xrightarrow[U_0(t)^\dagger]{} \langle\nu|$$

B.3 Perturbations

In the presence of noise, we can try to use perturbation theory to calculate the effect on the quantum channel.

The first order effect on time-evolution operator is:

$$|\alpha\rangle \xleftarrow[H_1(t_1)]{U_0(t-t_1) \qquad U_0(t_1)} |\mu\rangle$$

$$\begin{aligned}
[U_1(t)]_{\alpha\mu} &= \frac{-i}{\hbar}\int_0^t dt_1 [U_0(t-t_1)H_1(t_1)U_0(t_1)]_{\alpha\mu} \\
&= \frac{-i}{2}\int_0^t dt_1 e^{-\frac{i\Omega(t-t_1)}{2}(-1)^\alpha}\nu(t_1)[\sigma^x]_{\alpha\mu}e^{-\frac{i\Omega t_1}{2}(-1)^\mu} \\
&= \frac{-i}{2}\delta_{\mu,\alpha+1}e^{-\frac{i\Omega t}{2}(-1)^\alpha}\int_0^t dt_1 e^{i\Omega t_1(-1)^\alpha}\nu(t_1)
\end{aligned} \tag{B.6}$$

Second-order effect is given by:

$$|\alpha\rangle \xleftarrow[H_1(t_1)]{U_0(t-t_1)} \xleftarrow[H_1(t_2)]{U_0(t_1-t_2)} \xleftarrow{U_0(t_2)} |\mu\rangle$$

$$\begin{aligned}
[U_2(t)]_{\alpha\mu} &= \frac{-1}{\hbar^2}\int_0^t dt_1 \int_0^{t_1} dt_2 [U_0(t-t_1)H_1(t_1)U_0(t_1-t_2)H_1(t_2)U_0(t_2)]_{\alpha\mu} \\
&= \frac{-1}{4}\delta_{\alpha,\mu}e^{-\frac{i\Omega t}{2}(-1)^\alpha}\int_0^t dt_1 \int_0^{t_1} dt_2 e^{i\Omega(t_1-t_2)(-1)^\alpha}\nu(t_1)\nu(t_2)
\end{aligned} \tag{B.7}$$

B.4 Averaging over the noise

As per our noise model, we have the following two properties:

$$\overline{\nu(t)} = 0 \tag{B.8}$$

$$\overline{\nu(t_1)\nu(t_2)} = K(|t_1 - t_2|) \tag{B.9}$$

In order to average over the noise, lets define a new tensor quantity $\Gamma(t)$.

$$\begin{aligned}
[\rho(t)]_{\alpha\beta} &= \sum_{\mu,\nu} [U(t)]_{\alpha\mu}[\rho(0)]_{\mu\nu}[U(t)^\dagger]_{\nu\beta} \\
[\rho(t)]_{\alpha\beta} &= \sum_{\mu,\nu} [U(t)]_{\alpha\mu}[U(t)^*]_{\beta\nu}[\rho(0)]_{\mu\nu} \\
\overline{[\rho(t)]_{\alpha\beta}} &= \sum_{\mu,\nu} \overline{\Gamma_{\alpha\beta,\mu\nu}(t)}[\rho(0)]_{\mu\nu}
\end{aligned} \tag{B.10}$$

where $\Gamma_{\alpha\beta,\mu\nu}(t) = [U(t)]_{\alpha\mu}[U(t)^*]_{\beta\nu}$. We can expand $\overline{\Gamma_{\alpha\beta,\mu\nu}(t)}$ in a perturbative series up to second order as shown in Fig. B.1.

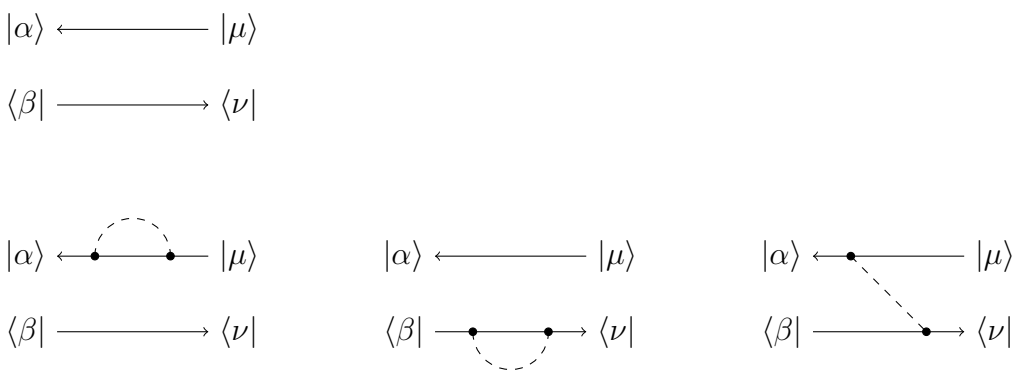

Figure B.1: The tensor quantity $\overline{\Gamma_{\alpha\beta,\mu\nu}(t)}$ is written out as a (perturbative) diagrammatic series. The arrows to the left correspond to the free evolution $U_0(t)$ and the arrows to the right correspond to $U_0(t)^\dagger$. The vertices correspond to the perturbing term and have a vertex factor $-\frac{i}{2}\sigma^x$. The dashed lines correspond to the noise correlation function giving a factor of $K(|t_1 - t_2|)$ where t_1 and t_2 are the end-points of the dashed line. These end-points need to be integrated over. The first row of the diagram gives the bare tensor. The second row shows the second-order corrections to the tensor caused by the noise.

$$\begin{aligned}
\overline{\Gamma_{\alpha\beta,\mu\nu}(t)} = {} & \delta_{\alpha\mu}\delta_{\beta\nu}e^{-\frac{i\Omega t}{2}[(-1)^\alpha-(-1)^\beta]} \\
& - \frac{1}{4}\delta_{\alpha\mu}\delta_{\beta\nu}e^{-\frac{i\Omega t}{2}[(-1)^\alpha-(-1)^\beta]}\int_0^t dt_1\int_0^{t_1} dt_2 e^{i\Omega(t_1-t_2)(-1)^\alpha}K(|t_1-t_2|) \\
& - \frac{1}{4}\delta_{\alpha\mu}\delta_{\beta\nu}e^{-\frac{i\Omega t}{2}[(-1)^\alpha-(-1)^\beta]}\int_0^t dt_1\int_0^{t_1} dt_2 e^{-i\Omega(t_1-t_2)(-1)^\beta}K(|t_1-t_2|) \\
& + \frac{1}{4}\delta_{\mu,\alpha+1}\delta_{\nu,\beta+1}e^{-\frac{i\Omega t}{2}[(-1)^\alpha-(-1)^\beta]}\int_0^t dt_1\int_0^{t} dt_2 e^{-\Omega[t_1(-1)^\alpha-t_2(-1)^\beta]}K(|t_1-t_2|)
\end{aligned} \tag{B.11}$$

We can Fourier transform the noise correlation function to obtain the noise power spectral density. This allows us to perform the integrals over time, leaving behind a window function that depends on Fourier frequency.

$$\begin{aligned}\overline{\Gamma_{\alpha\beta,\mu\nu}(t)} &= \delta_{\alpha\mu}\delta_{\beta\nu}e^{-\frac{i\Omega t}{2}[(-1)^\alpha-(-1)^\beta]} \\ &\quad - \frac{1}{4}\delta_{\alpha\mu}\delta_{\beta\nu}e^{-\frac{i\Omega t}{2}[(-1)^\alpha-(-1)^\beta]}\int\frac{d\omega}{2\pi}S(\omega)[\chi_2(\omega,\Omega,t,\alpha)+\chi_2(\omega,\Omega,t,\beta+1)] \\ &\quad + \frac{1}{4}\delta_{\mu,\alpha+1}\delta_{\nu,\beta+1}e^{-\frac{i\Omega t}{2}[(-1)^\alpha-(-1)^\beta]}\int\frac{d\omega}{2\pi}S(\omega)\chi_1(\omega,\Omega,t,\alpha,\beta)\end{aligned} \tag{B.12}$$

where we have defined two window functions χ_1 and χ_2.

$$\begin{aligned}\chi_2(\omega,\Omega,t,\alpha) &= \big(\Omega^2+\omega^2+i(-1)^\alpha\Omega t(\Omega^2-\omega^2) \\ &\quad - e^{i\Omega t(-1)^\alpha}((\Omega^2+\omega^2)\cos\omega t - 2i(-1)^\alpha\Omega\omega t\sin\omega t)\big)/(\Omega^2-\omega^2)^2\end{aligned} \tag{B.13}$$

$$\chi_1(\omega,\Omega,t,\alpha,\beta) = \begin{cases}\frac{2\left((\Omega^2+\omega^2)(1-\cos\Omega t\cos\omega t)-2\Omega\omega\sin\Omega t\sin\omega t\right)}{(\Omega^2-\omega^2)^2} & \beta=\alpha \\ \frac{2(\cos\omega t-\cos\Omega t)(\cos\Omega t+i(-1)^\alpha\sin\Omega t)}{\Omega^2-\omega^2} & \beta=\alpha+1\end{cases} \tag{B.14}$$

Appendix C

OPTICAL TWEEZER POTENTIAL IN 3D

In the experimental setup, the atoms are held in place using optical tweezers which are described by a Gaussian beam. The trapping potential experienced by the atoms is given by:

$$U(x,y,z) = -\frac{Z_0}{2}\alpha(\lambda) \times I(x,y,z) \tag{C.1}$$

where $Z_0 = \sqrt{\mu_0/\epsilon_0}$ is the vacuum wave impedance, α is the polarizability of the atom and $I(r,z)$ is the intensity of the trapping laser [37].

$$I(x,y,z) = I_0 \frac{1}{1+(\frac{z}{z_R})^2} \exp\left(\frac{-2(x^2+y^2)}{w_0^2(1+(\frac{z}{z_R})^2)}\right) \tag{C.2}$$

where $z_R = \pi w_0^2/\lambda_t = k_t w_0^2/2$ is the Rayleigh range [61]. In our current setup, $w_0 \approx \lambda_t = 813nm$. We can Taylor expand this expression to 4th order to obtain an algebraic expression for the trap potential. Let $\bar{x} = x/w_0$, $\bar{y} = y/w_0$ and $\bar{z} = z/z_R$.

$$\begin{aligned} I(x,y,z) \approx I_0\Big(&1 - 2\bar{x}^2 - 2\bar{y}^2 - \bar{z}^2 \\ &+ 2\bar{x}^4 + 2\bar{y}^4 + \bar{z}^4 \\ &+ 4\bar{x}^2\bar{y}^2 + \bar{x}^2\bar{z}^2 + \bar{y}^2\bar{z}^2 + \dots\Big) \end{aligned} \tag{C.3}$$

Thus to leading order, the Gaussian potential gives rise to an isotropic harmonic potential in the radial direction and a weaker harmonic potential in the axial direction. Using this expression we can write down the Hamiltonian for the atom in the trap. We can define $\omega_x = \omega_y = \omega_\rho \equiv \sqrt{\frac{2mZ_0\alpha I_0}{w_0^2}}$ and $\omega_z \equiv \sqrt{\frac{mZ_0\alpha I_0}{z_R^2}}$.

$$\begin{aligned} H_{trap} = \ &\frac{p_x^2}{2m} + \frac{1}{2}m\omega_x^2\Big(x^2 - \frac{x^4}{w_0^2} + \dots\Big) \\ &+ \frac{p_y^2}{2m} + \frac{1}{2}m\omega_y^2\Big(y^2 - \frac{y^4}{w_0^2} + \dots\Big) \\ &+ \frac{p_z^2}{2m} + \frac{1}{2}m\omega_z^2\Big(z^2 - \frac{z^4}{z_R^2} + \dots\Big) \\ &- m\omega_\rho^2\Big(\frac{x^2y^2}{w_0^2} + \frac{y^2z^2}{z_R^2} + \frac{x^2z^2}{z_R^2} + \dots\Big) \end{aligned} \tag{C.4}$$

We can see that to leading order the three axes x, y, and z have independent harmonic oscillators. The harmonic oscillator states only mix together at fourth order. Thus at low temperatures we can (1) assume the three axes are independent and (2) ignore the y and z directions entirely and treat the system as one dimensional (assuming drive laser is along x-direction).

BIBLIOGRAPHY

[1] Richard Feynman. "Simulating Physics with Computers". In: *Intl. Journal of Theoretical Physics* 21 (1982), pp. 467–488.

[2] Salonik Resch and Ulya R. Karpuzcu. *Quantum Computing: An Overview Across the System Stack*. 2019. arXiv: 1905.07240 [quant-ph].

[3] Ashley Montanaro. "Quantum algorithms: an overview". In: *npj Quantum Information* 2.1 (Jan. 2016), p. 15023. ISSN: 2056-6387. DOI: 10.1038/npjqi.2015.23. URL: https://doi.org/10.1038/npjqi.2015.23.

[4] Adam Smith, M. S. Kim, Frank Pollmann, and Johannes Knolle. "Simulating quantum many-body dynamics on a current digital quantum computer". In: *npj Quantum Information* 5.1 (Nov. 2019), p. 106. ISSN: 2056-6387. DOI: 10.1038/s41534-019-0217-0. URL: https://doi.org/10.1038/s41534-019-0217-0.

[5] M. C. Bañuls et al. *Simulating Lattice Gauge Theories within Quantum Technologies*. 2019. arXiv: 1911.00003 [quant-ph].

[6] B. P. Lanyon, J. D. Whitfield, G. G. Gillett, M. E. Goggin, M. P. Almeida, I. Kassal, J. D. Biamonte, M. Mohseni, B. J. Powell, M. Barbieri, A. Aspuru-Guzik, and A. G. White. "Towards quantum chemistry on a quantum computer". In: *Nature Chemistry* 2.2 (Feb. 2010), pp. 106–111. ISSN: 1755-4349. DOI: 10.1038/nchem.483. URL: https://doi.org/10.1038/nchem.483.

[7] Morten Kjaergaard, Mollie E. Schwartz, Jochen Braumüller, Philip Krantz, Joel I.-J. Wang, Simon Gustavsson, and William D. Oliver. "Superconducting Qubits: Current State of Play". In: *Annual Review of Condensed Matter Physics* 11.1 (2020), pp. 369–395. DOI: 10.1146/annurev-conmatphys-031119-050605. eprint: https://doi.org/10.1146/annurev-conmatphys-031119-050605. URL: https://doi.org/10.1146/annurev-conmatphys-031119-050605.

[8] Colin D. Bruzewicz, John Chiaverini, Robert McConnell, and Jeremy M. Sage. "Trapped-ion quantum computing: Progress and challenges". In: *Applied Physics Reviews* 6.2 (2019), p. 021314. DOI: 10.1063/1.5088164. eprint: https://doi.org/10.1063/1.5088164. URL: https://doi.org/10.1063/1.5088164.

[9] Debasis Bera, Lei Qian, Teng-Kuan Tseng, and Paul H. Holloway. "Quantum Dots and Their Multimodal Applications: A Review". eng. In: *Materials* 3.4 (Mar. 2010). PMC5445848[pmcid], pp. 2260–2345. ISSN: 1996-1944. DOI: 10.3390/ma3042260. URL: https://doi.org/10.3390/ma3042260.

[10] Mark Saffman. "Quantum computing with neutral atoms". In: *National Science Review* 6.1 (Sept. 2018), pp. 24–25. ISSN: 2095-5138. DOI: 10.1093/nsr/nwy088. eprint: https://academic.oup.com/nsr/article-pdf/6/1/24/30336094/nwy088.pdf. URL: https://doi.org/10.1093/nsr/nwy088.

[11] Michael A. Nielsen and Isaac L. Chuang. *Quantum Computation and Quantum Information: 10th Anniversary Edition*. 10th. USA: Cambridge University Press, 2011. ISBN: 1107002176.

[12] Antoine Browaeys, Daniel Barredo, and Thierry Lahaye. "Experimental investigations of dipole–dipole interactions between a few Rydberg atoms". In: *Journal of Physics B: Atomic, Molecular and Optical Physics* 49.15 (June 2016), p. 152001. DOI: 10.1088/0953-4075/49/15/152001. URL: https://doi.org/10.1088%2F0953-4075%2F49%2F15%2F152001.

[13] Y.-Y. Jau, A. M. Hankin, T. Keating, I. H. Deutsch, and G. W. Biedermann. "Entangling atomic spins with a Rydberg-dressed spin-flip blockade". In: *Nature Physics* 12.1 (2016), pp. 71–74. ISSN: 1745-2481. DOI: 10.1038/nphys3487. URL: https://doi.org/10.1038/nphys3487.

[14] Harry Levine, Alexander Keesling, Ahmed Omran, Hannes Bernien, Sylvain Schwartz, Alexander S. Zibrov, Manuel Endres, Markus Greiner, Vladan Vuleti ć, and Mikhail D. Lukin. "High-Fidelity Control and Entanglement of Rydberg-Atom Qubits". In: *Phys. Rev. Lett.* 121 (12 Sept. 2018), p. 123603. DOI: 10.1103/PhysRevLett.121.123603. URL: https://link.aps.org/doi/10.1103/PhysRevLett.121.123603.

[15] T. M. Graham, M. Kwon, B. Grinkemeyer, Z. Marra, X. Jiang, M. T. Lichtman, Y. Sun, M. Ebert, and M. Saffman. "Rydberg-Mediated Entanglement in a Two-Dimensional Neutral Atom Qubit Array". In: *Phys. Rev. Lett.* 123 (23 Dec. 2019), p. 230501. DOI: 10.1103/PhysRevLett.123.230501. URL: https://link.aps.org/doi/10.1103/PhysRevLett.123.230501.

[16] Harry Levine, Alexander Keesling, Giulia Semeghini, Ahmed Omran, Tout T. Wang, Sepehr Ebadi, Hannes Bernien, Markus Greiner, Vladan Vuleti ć, Hannes Pichler, and Mikhail D. Lukin. "Parallel Implementation of High-Fidelity Multiqubit Gates with Neutral Atoms". In: *Phys. Rev. Lett.* 123 (17 Oct. 2019), p. 170503. DOI: 10.1103/PhysRevLett.123.170503. URL: https://link.aps.org/doi/10.1103/PhysRevLett.123.170503.

[17] Ivaylo S. Madjarov, Jacob P. Covey, Adam L. Shaw, Joonhee Choi, Anant Kale, Alexandre Cooper, Hannes Pichler, Vladimir Schkolnik, Jason R. Williams, and Manuel Endres. "High-fidelity entanglement and detection of alkaline-earth Rydberg atoms". In: *Nature Physics* (May 2020). ISSN: 1745-2481. DOI: 10.1038/s41567-020-0903-z. URL: https://doi.org/10.1038/s41567-020-0903-z.

[18] M Saffman. "Quantum computing with atomic qubits and Rydberg interactions: progress and challenges". In: *Journal of Physics B: Atomic, Molecular and Optical Physics* 49.20 (Oct. 2016), p. 202001. DOI: 10.1088/0953-4075/49/20/202001. URL: https://doi.org/10.1088%2F0953-4075%2F49%2F20%2F202001.

[19] P. Schauß, J. Zeiher, T. Fukuhara, S. Hild, M. Cheneau, T. Macrı, T. Pohl, I. Bloch, and C. Gross. "Crystallization in Ising quantum magnets". In: *Science* 347.6229 (2015), pp. 1455–1458. ISSN: 0036-8075. DOI: 10.1126/science.1258351. URL: https://science.sciencemag.org/content/347/6229/1455.

[20] Henning Labuhn, Daniel Barredo, Sylvain Ravets, Sylvain de Léséleuc, Tommaso Macrì, Thierry Lahaye, and Antoine Browaeys. "Tunable two-dimensional arrays of single Rydberg atoms for realizing quantum Ising models". In: *Nature* 534.7609 (2016), pp. 667–670. ISSN: 1476-4687. DOI: 10.1038/nature18274. URL: https://doi.org/10.1038/nature18274.

[21] Hannes Bernien, Sylvain Schwartz, Alexander Keesling, Harry Levine, Ahmed Omran, Hannes Pichler, Soonwon Choi, Alexander S. Zibrov, Manuel Endres, Markus Greiner, Vladan Vuletic, and Mikhail D. Lukin. "Probing many-body dynamics on a 51-atom quantum simulator". In: *Nature* 551.7682 (2017), pp. 579–584. ISSN: 1476-4687. DOI: 10.1038/nature24622. URL: https://doi.org/10.1038/nature24622.

[22] Vincent Lienhard, Sylvain de Léséleuc, Daniel Barredo, Thierry Lahaye, Antoine Browaeys, Michael Schuler, Louis-Paul Henry, and Andreas M. Läuchli. "Observing the Space- and Time-Dependent Growth of Correlations in Dynamically Tuned Synthetic Ising Models with Antiferromagnetic Interactions". In: *Phys. Rev. X* 8 (2 June 2018), p. 021070. DOI: 10.1103/PhysRevX.8.021070. URL: https://link.aps.org/doi/10.1103/PhysRevX.8.021070.

[23] Elmer Guardado-Sanchez, Peter T. Brown, Debayan Mitra, Trithep Devakul, David A. Huse, Peter Schauß, and Waseem S. Bakr. "Probing the Quench Dynamics of Antiferromagnetic Correlations in a 2D Quantum Ising Spin System". In: *Phys. Rev. X* 8 (2 June 2018), p. 021069. DOI: 10.1103/PhysRevX.8.021069. URL: https://link.aps.org/doi/10.1103/PhysRevX.8.021069.

[24] T.M. Graham et al. "Rydberg mediated entanglement in a two-dimensional neutral atom qubit array". In: *arXiv* 1908.06103 (2019).

[25] Yang Wang, Aishwarya Kumar, Tsung-Yao Wu, and David S. Weiss. "Single-qubit gates based on targeted phase shifts in a 3D neutral atom array". In: *Science* 352.6293 (2016), pp. 1562–1565. ISSN: 0036-8075. DOI: 10.1126/science.aaf2581. eprint: https://science.sciencemag.org/content/352/6293/1562.full.pdf. URL: https://science.sciencemag.org/content/352/6293/1562.

[26] M. Saffman, T. G. Walker, and K. Mølmer. "Quantum information with Rydberg atoms". In: *Rev. Mod. Phys.* 82 (3 Aug. 2010), pp. 2313–2363. DOI: 10.1103/RevModPhys.82.2313. URL: https://link.aps.org/doi/10.1103/RevModPhys.82.2313.

[27] C. J. Ballance, T. P. Harty, N. M. Linke, M. A. Sepiol, and D. M. Lucas. "High-Fidelity Quantum Logic Gates Using Trapped-Ion Hyperfine Qubits". In: *Phys. Rev. Lett.* 117 (6 Aug. 2016), p. 060504. DOI: 10.1103/PhysRevLett.117.060504. URL: https://link.aps.org/doi/10.1103/PhysRevLett.117.060504.

[28] R. Barends et al. "Superconducting quantum circuits at the surface code threshold for fault tolerance". In: *Nature* 508.7497 (2014), pp. 500–503. ISSN: 1476-4687. DOI: 10.1038/nature13171. URL: https://doi.org/10.1038/nature13171.

[29] L. S. Theis, F. Motzoi, F. K. Wilhelm, and M. Saffman. "High-fidelity Rydberg-blockade entangling gate using shaped, analytic pulses". In: *Phys. Rev. A* 94 (3 Sept. 2016), p. 032306. DOI: 10.1103/PhysRevA.94.032306. URL: https://link.aps.org/doi/10.1103/PhysRevA.94.032306.

[30] T. Xia, X. L. Zhang, and M. Saffman. "Analysis of a controlled phase gate using circular Rydberg states". In: *Phys. Rev. A* 88 (6 Dec. 2013), p. 062337. DOI: 10.1103/PhysRevA.88.062337. URL: https://link.aps.org/doi/10.1103/PhysRevA.88.062337.

[31] David Petrosyan, Felix Motzoi, Mark Saffman, and Klaus Mølmer. "High-fidelity Rydberg quantum gate via a two-atom dark state". In: *Phys. Rev. A* 96 (4 Oct. 2017), p. 042306. DOI: 10.1103/PhysRevA.96.042306. URL: https://link.aps.org/doi/10.1103/PhysRevA.96.042306.

[32] Sylvain de Léséleuc, Daniel Barredo, Vincent Lienhard, Antoine Browaeys, and Thierry Lahaye. "Analysis of imperfections in the coherent optical excitation of single atoms to Rydberg states". In: *Phys. Rev. A* 97 (5 May 2018), p. 053803. DOI: 10.1103/PhysRevA.97.053803. URL: https://link.aps.org/doi/10.1103/PhysRevA.97.053803.

[33] Jacob P. Covey, Ivaylo S. Madjarov, Alexandre Cooper, and Manuel Endres. "2000-Times Repeated Imaging of Strontium Atoms in Clock-Magic Tweezer Arrays". In: *Phys. Rev. Lett.* 122 (17 May 2019), p. 173201. DOI: 10.1103/PhysRevLett.122.173201. URL: https://link.aps.org/doi/10.1103/PhysRevLett.122.173201.

[34] Alexandre Cooper, Jacob P. Covey, Ivaylo S. Madjarov, Sergey G. Porsev, Marianna S. Safronova, and Manuel Endres. "Alkaline-Earth Atoms in Optical Tweezers". In: *Phys. Rev. X* 8 (4 Dec. 2018), p. 041055. DOI: 10.1103/PhysRevX.8.041055. URL: https://link.aps.org/doi/10.1103/PhysRevX.8.041055.

[35] Ivaylo S. Madjarov, Alexandre Cooper, Adam L. Shaw, Jacob P. Covey, Vladimir Schkolnik, Tai Hyun Yoon, Jason R. Williams, and Manuel Endres. "An Atomic-Array Optical Clock with Single-Atom Readout". In: *Phys. Rev. X* 9 (4 Dec. 2019), p. 041052. DOI: 10.1103/PhysRevX.9.041052. URL: https://link.aps.org/doi/10.1103/PhysRevX.9.041052.

[36] D. Jaksch, J. I. Cirac, P. Zoller, S. L. Rolston, R. Côté, and M. D. Lukin. "Fast Quantum Gates for Neutral Atoms". In: *Phys. Rev. Lett.* 85 (10 Sept. 2000), pp. 2208–2211. DOI: 10.1103/PhysRevLett.85.2208. URL: https://link.aps.org/doi/10.1103/PhysRevLett.85.2208.

[37] Daniel Steck. "Quantum and Atom Optics". In: *http://steck.us/teaching* (2007), p. 38.

[38] R. W. P. Drever, J. L. Hall, F. V. Kowalski, J. Hough, G. M. Ford, A. J. Munley, and H. Ward. "Laser phase and frequency stabilization using an optical resonator". In: *Applied Physics B* 31.2 (June 1983), pp. 97–105. ISSN: 1432-0649. DOI: 10.1007/BF00702605. URL: https://doi.org/10.1007/BF00702605.

[39] Pierre Cladé. "Oscillations de Bloch d'atomes ultrafroids et mesure de la constante de structure fine (Ph.D. thesis)". In: *Physique Atomique [physics.atom-ph] Université Pierre et Marie Curie* (2005).

[40] Marco Tarallo. "Development of a Strontium optical lattice clock (Ph.D. thesis)". In: *Galileo Galilei School of Graduate Studies* (2009), pp. 1–18.

[41] Warren G. Nagourney. *Quantum electronics for atomic physics*. Includes bibliographical references and index. Oxford : Oxford University Press, [2010] ©2010, [2010]. URL: https://search.library.wisc.edu/catalog/9910089880202121.

[42] Dana Z. Anderson, Josef C. Frisch, and Carl S. Masser. "Mirror reflectometer based on optical cavity decay time". In: *Appl. Opt.* 23.8 (Apr. 1984), pp. 1238–1245. DOI: 10.1364/AO.23.001238. URL: http://ao.osa.org/abstract.cfm?URI=ao-23-8-1238.

[43] G. S. Agarwal. "Exact Solution for the Influence of Laser Temporal Fluctuations on Resonance Fluorescence". In: *Phys. Rev. Lett.* 37 (21 Nov. 1976), pp. 1383–1386. DOI: 10.1103/PhysRevLett.37.1383. URL: https://link.aps.org/doi/10.1103/PhysRevLett.37.1383.

[44] G. S. Agarwal. "Quantum statistical theory of optical-resonance phenomena in fluctuating laser fields". In: *Phys. Rev. A* 18 (4 Oct. 1978), pp. 1490–1506. DOI: 10.1103/PhysRevA.18.1490. URL: https://link.aps.org/doi/10.1103/PhysRevA.18.1490.

[45] N.G. Van Kampen. "A cumulant expansion for stochastic linear differential equations. I". In: *Physica* 74.2 (1974), pp. 215–238. ISSN: 0031-8914. DOI: https://doi.org/10.1016/0031-8914(74)90121-9. URL: http://www.sciencedirect.com/science/article/pii/0031891474901219.

[46] N.G. Van Kampen. "A cumulant expansion for stochastic linear differential equations. II". In: *Physica* 74.2 (1974), pp. 239–247. ISSN: 0031-8914. DOI: https://doi.org/10.1016/0031-8914(74)90122-0. URL: http://www.sciencedirect.com/science/article/pii/0031891474901220.

[47] W. M. Witzel and S. Das Sarma. "Quantum theory for electron spin decoherence induced by nuclear spin dynamics in semiconductor quantum computer architectures: Spectral diffusion of localized electron spins in the nuclear solid-state environment". In: *Phys. Rev. B* 74 (3 July 2006), p. 035322. DOI: 10.1103/PhysRevB.74.035322. URL: https://link.aps.org/doi/10.1103/PhysRevB.74.035322.

[48] G. Kucsko, S. Choi, J. Choi, P. C. Maurer, H. Zhou, R. Landig, H. Sumiya, S. Onoda, J. Isoya, F. Jelezko, E. Demler, N. Y. Yao, and M. D. Lukin. "Critical Thermalization of a Disordered Dipolar Spin System in Diamond". In: *Phys. Rev. Lett.* 121 (2 July 2018), p. 023601. DOI: 10.1103/PhysRevLett.121.023601. URL: https://link.aps.org/doi/10.1103/PhysRevLett.121.023601.

[49] J. Preskill. *Notes on noise*. URL: http://www.theory.caltech.edu/people/preskill/papers/decoherence_notes.pdf.

[50] Sylvain de Léséleuc. "Quantum simulation of spin models with assembled arrays of Rydberg atoms (Ph.D. thesis)". In: *Institut d'Optique* (2018), pp. 103–108.

[51] Jun Ye, H. J. Kimble, and Hidetoshi Katori. "Quantum State Engineering and Precision Metrology Using State-Insensitive Light Traps". In: *Science* 320.5884 (2008), pp. 1734–1738. ISSN: 0036-8075. DOI: 10.1126/science.1148259. URL: https://science.sciencemag.org/content/320/5884/1734.

[52] Jack Wilson, Samuel Saskin, Yijian Meng, Shuo Ma, Rohit Dilip, Alex Burgers, and Jeff Thompson. *Trapped arrays of alkaline earth Rydberg atoms in optical tweezers*. 2019. arXiv: 1912.08754 [quant-ph].

[53] D. J. Wineland and Wayne M. Itano. "Laser cooling of atoms". In: *Phys. Rev. A* 20 (4 Oct. 1979), pp. 1521–1540. DOI: 10.1103/PhysRevA.20.1521. URL: https://link.aps.org/doi/10.1103/PhysRevA.20.1521.

[54] T. Wilk, A. Gaëtan, C. Evellin, J. Wolters, Y. Miroshnychenko, P. Grangier, and A. Browaeys. "Entanglement of Two Individual Neutral Atoms Using Rydberg Blockade". In: *Phys. Rev. Lett.* 104 (1 Jan. 2010), p. 010502.

DOI: 10.1103/PhysRevLett.104.010502. URL: https://link.aps.org/doi/10.1103/PhysRevLett.104.010502.

[55] C L Vaillant, M P A Jones, and R M Potvliege. "Long-range Rydberg–Rydberg interactions in calcium, strontium and ytterbium". In: *Journal of Physics B: Atomic, Molecular and Optical Physics* 45.13 (July 2012), p. 135004. ISSN: 0953-4075. DOI: 10.1088/0953-4075/45/13/135004. URL: https://iopscience.iop.org/article/10.1088/0953-4075/45/13/135004.

[56] Steven R. White. "Equivalence of the antiferromagnetic Heisenberg ladder to a single S=1 chain". In: *Phys. Rev. B* 53 (1 Jan. 1996), pp. 52–55. DOI: 10.1103/PhysRevB.53.52. URL: https://link.aps.org/doi/10.1103/PhysRevB.53.52.

[57] S. R. White, R. M. Noack, and D. J. Scalapino. "Resonating Valence Bond Theory of Coupled Heisenberg Chains". In: *Phys. Rev. Lett.* 73 (6 Aug. 1994), pp. 886–889. DOI: 10.1103/PhysRevLett.73.886. URL: https://link.aps.org/doi/10.1103/PhysRevLett.73.886.

[58] E. Dagotto, J. Riera, and D. Scalapino. "Superconductivity in ladders and coupled planes". In: *Phys. Rev. B* 45 (10 Mar. 1992), pp. 5744–5747. DOI: 10.1103/PhysRevB.45.5744. URL: https://link.aps.org/doi/10.1103/PhysRevB.45.5744.

[59] A. Celi, B. Vermersch, O. Viyuela, H. Pichler, M. D. Lukin, and P. Zoller. *Emerging 2D Gauge theories in Rydberg configurable arrays*. 2019. arXiv: 1907.03311 [quant-ph].

[60] Sylvain de Léséleuc, Vincent Lienhard, Pascal Scholl, Daniel Barredo, Sebastian Weber, Nicolai Lang, Hans Peter Büchler, Thierry Lahaye, and Antoine Browaeys. "Observation of a symmetry-protected topological phase of interacting bosons with Rydberg atoms". In: *Science* (2019). ISSN: 0036-8075. DOI: 10.1126/science.aav9105. eprint: https://science.sciencemag.org/content/early/2019/07/31/science.aav9105.full.pdf. URL: https://science.sciencemag.org/content/early/2019/07/31/science.aav9105.

[61] Orazio Svelto. "Principles of Lasers 5th ed." In: *Springer Science+Business Media, LLC* (2010), pp. 150–154.